

FILE COPY

12

ADA189260



LASER IGNITION OF NITRAMINE COMPOSITE PROPELLANTS
AND CRACK PROPAGATION AND BRANCHING IN
BURNING SOLID PROPELLANTS

FINAL REPORT

Sponsored By
Office of Naval Research
Power Program
Arlington, Virginia
Contract No. N00014-79-C-0762

Prepared By
K. K. Kuo, J. U. Kim, J. Nimis, J. Smedley, J. M. Char,
B. Fetherolf, T. Snyder, and C. Zanotti

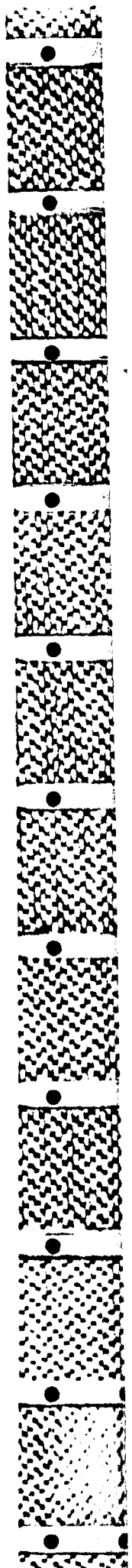
October 1987

DTIC
ELECTE
DEC 04 1987
S D

DISTRIBUTION STATEMENT A
Approved for public release
Distribution Unlimited

THE PENNSYLVANIA STATE UNIVERSITY
College of Engineering
Department of Mechanical Engineering
University Park, Pennsylvania

87 11 30 115



REPORT DOCUMENTATION PAGE		READ INSTRUCTIONS BEFORE COMPLETING FORM
1. REPORT NUMBER	2. GOVT ACCESSION NO.	3. RECIPIENT'S CATALOG NUMBER
4. TITLE (and Subtitle) "Laser Ignition of Nitramine Composite Propellants and Crack Propagation and Branching in Burning Solid Propellants"		5. TYPE OF REPORT & PERIOD COVERED Final - 1/1/86-8/31/87
		6. PERFORMING ORG. REPORT NUMBER
7. AUTHOR(s) K. K. Kuo, J. U. Kim, J. Nimis, J. Smedley J.-M. Char, B. Fetherolf, T. Snyder, and C. Zanotti		8. CONTRACT OR GRANT NUMBER(s) N00014-79-0762
9. PERFORMING ORGANIZATION NAME AND ADDRESS Department of Mechanical Engineering The Pennsylvania State University University Park, PA 16802		10. PROGRAM ELEMENT, PROJECT, TASK AREA & WORK UNIT NUMBERS
11. CONTROLLING OFFICE NAME AND ADDRESS Office of Naval Research Power Program Arlington, VA 22217		12. REPORT DATE October 15, 1987
		13. NUMBER OF PAGES
14. MONITORING AGENCY NAME & ADDRESS (if different from Controlling Office)		15. SECURITY CLASS. (of this report) Unclassified
		15a. DECLASSIFICATION/DOWNGRADING SCHEDULE
16. DISTRIBUTION STATEMENT (of this Report) Approved for public release; distribution unlimited.		
17. DISTRIBUTION STATEMENT (of the abstract entered in Block 20, if different from Report)		
18. SUPPLEMENTARY NOTES <i>carbon dioxide</i>		
19. KEY WORDS (Continue on reverse side if necessary and identify by block number) Ignition, CO_2 Laser, Nitramine, Composite Propellants, Thermal Decomposition, Reaction Mechanisms, Ignition Delay, Radiation Ignition, Crack Propagation, Crack Branching, Interrupted Burning, Depressurization, Extinguishment		
20. ABSTRACT (Continue on reverse side if necessary and identify by block number) (See reverse.)		



ABSTRACT

Two major tasks performed during the report period of investigation were: (i) laser ignition of nitramine-based composite propellants using a high-powered CO_2 laser and (ii) crack propagation and branching in burning solid propellants.

The laser ignition of a series of RDX-based composite propellants was studied theoretically and experimentally. A comprehensive model for the radiative ignition of the nitramine composite propellants was formulated. The theoretical model was solved numerically. A radiative ignition test setup employing a high-powered CO_2 laser was designed and constructed to study ignition characteristics of a series of RDX-based nitramine composite propellants. Interactions between the infrared laser beam and nitramine composite propellants revealed a number of interesting processes. The laser ignition of composite propellants involves many complex thermophysicochemical processes including gasification, initiation of a luminous flame, propagation of the flame, and chemical reactions near the sample surface as well as heat conduction in solid phases. In general, the delay time based upon the onset of light emission decreases monotonically with the increase of incident laser energy flux. The slope was found to be affected by the oxygen concentration in the ambient gas. This effect is prominent when the sample contains volatile energetic plasticizers. The effect of oxygen concentration is more pronounced in the gas-phase ignition of nitramine propellants than in conventional AP-based composite propellants. The flame structures of nitramine propellants depend strongly upon the ambient gas conditions. As ambient oxygen concentration is increased, the flame moves closer to the sample surface; this implies that the gas-phase reaction with ambient oxygen plays an important role in the initial phase of laser ignition of nitramine propellants.

The importance of crack propagation in solid rocket motors is widely recognized. However, the processes of crack propagation and branching in burning solid propellants are not as yet well understood. These processes could be instrumental in creating large specific areas for burning, and in extreme cases causing rocket motor failure. Numerous samples have been recovered from interrupted-burning experiments. Depending on the pressurization rate and sample geometry, different modes of crack propagation and/or branching were observed. This problem was analyzed through the use of basic physical principles, current theories on crack propagation in viscoelastic media, and experimental results. A set of governing dimensionless parameters which control and characterize the degree of damage was obtained. Key factors influencing the crack combustion, propagation and branching process considered in the dimensional analysis include chamber pressurization rate, initial crack length, initial temperature, sample geometry, and mechanical and thermal properties of the solid propellant. Based on experimental results, a multiple regression analysis was performed to obtain a set of correlations between the dimensionless parameters. The procedures developed in this work demonstrate a methodology for obtaining similar correlations which could be used as guidelines for safe operating conditions of rocket motors.

→ *Keywords:*

**LASER IGNITION
OF NITRAMINE COMPOSITE PROPELLANTS
AND
CRACK PROPAGATION AND BRANCHING
IN BURNING SOLID PROPELLANTS**

FINAL REPORT

Sponsored by

Office of Naval Research
Power Program
Arlington, Virginia

Contract No. N00014-79-C-0762

Prepared by

Kenneth K. Kuo
Jong U. Kim
Jeffrey Nimis
Jesse Smedly
Jir-Ming Char
Barry Fetherolf
Timothy Snyder
Claudio Zanotti

Department of Mechanical Engineering
The Pennsylvania State University
University Park, PA 16902

Reproduction in whole or in part is permitted
for any purpose of the United States Government

Approved for public release; distribution unlimited

Accession For	
NTIS CRA&I	<input checked="" type="checkbox"/>
DTIC TAB	<input type="checkbox"/>
Unannounced	<input type="checkbox"/>
Justification	
By	
Distribution /	
Availability Codes	
Dist	Avail and/or Special
A-1	



TABLE OF CONTENTS

	<u>Page</u>
ABSTRACT	iii
TABLE OF CONTENT	v
LIST OF FIGURES	viii
LIST OF TABLES	xi
NOMENCLATURE	xii
ACKNOWLEDGEMENT	xv
I. INTRODUCTION	1
II. LASER IGNITION OF NITRAMINE COMPOSITE PROPELLANTS	3
2.1 INTRODUCTION	3
2.1.1 General Statement of the Problem	3
2.1.2 Previous Related Studies	5
2.1.2.1 Radiative Ignition - Experimental	10
2.1.2.2 Radiative Ignition - Theoretical	12
2.1.2.3 Combustion of Nitramine Propellants	16
2.1.3 Scope of Present Work	16
2.1.3.1 Theoretical Approach	16
2.1.3.2 Experimental Approach	16
2.2 THEORETICAL APPROACH	18
2.2.1 Description of Physical Model	18
2.2.2 Assumptions	21
2.2.3 Mathematical Model	22
2.2.3.1 Governing Equations and Boundary Conditions	22
2.2.3.2 Physicochemical Consideration for Pyrolysis and Ignition of Nitramine Composite Propellants	26
2.2.3.3 Modeling of Source Terms	31
2.2.3.4 Transformation of Governing Equations	32
2.2.4 Numerical Method	33
2.3 EXPERIMENTAL APPROACH	34
2.3.1 Introduction	34
2.3.2 Experimental Apparatus and Operation	34

2.3.3	Data Acquisition and Analysis Systems	40
2.3.4	Propellant Samples	41
2.3.5	Beam Intensity Distribution	41
2.3.6	Temperature Measurement	45
2.3.7	Gas Species Measurement	49
2.3.8	Surface Structure Observation	49
2.3.9	Schlieren Technique	50
2.4	RESULTS AND DISCUSSION	52
2.4.1	Experimental Results	52
2.4.1.1	Ignition Delay Time	52
2.4.1.2	Flame Observation	58
2.4.1.3	Thermal Wave Structure	75
2.4.1.4	Gas Analysis	81
2.4.1.5	Sample Surface Structure	84
2.5	SUMMARY AND CONCLUSIONS	87
III.	CRACK PROPAGATION AND BRANCHING IN BURNING SOLID PROPELLANTS	89
3.1	INTRODUCTION	89
3.1.1	Motivation and Objectives	89
3.1.2	Brief Survey of Related Work	90
3.2	EXPERIMENTAL SETUP	93
3.2.1	Selection of Sample Propellant Type	93
3.2.2	Sample Configuration	94
3.2.3	Test Setup	94
3.2.3.1	Test Chamber	94
3.2.3.2	Data Acquisition System	99
3.2.4	Test Procedure	102
3.3	THEORETICAL ANALYSIS	103
3.3.1	Crack Sample Geometry	103
3.3.2	Determination of Mechanical Properties	103
3.3.2.1	Relaxation Modulus	105
3.3.2.2	Crack Propagation Velocity	105
3.3.2.3	Fracture Energy and Related Parameters	110
3.3.3	Energy Balance Applied to the Control Volume	111
3.3.4	Dimensional Analysis	114

3.3.4.1 Arrangement into Meaningful Dimensionless Groups	114
3.3.4.2 Functional Relationships Between Dimensionless Parameters	115
3.4 RESULTS	117
3.4.1 Determination of Dimensionless Parameters	117
3.4.1.1 Pressure Loading in the Damaged Zone	117
3.4.1.2 Interpretation of Film Data	121
3.4.1.3 Determining Other Key Parameters	121
3.4.2 Relationships Between Dimensionless Parameters	127
3.4.3 Discussion of Results	129
3.5 SUMMARY AND CONCLUSIONS	135
REFERENCES	137
APPENDICES:	
A. MEASUREMENT OF CO ₂ LASER ENERGY FLUXES	144
B. DIFFERENT TECHNIQUES USED FOR ACHIEVING BEAM UNIFORMITY	149
C. ABSORPTION OF CO ₂ LASER BEAM ENERGY BY CO ₂ GAS	154
D. OPERATION PROCEDURE AND SAFETY FEATURES OF THE CO ₂ LASER SYSTEM	158
E. SPECIFICATION OF THE EQUIPMENT USED IN THE IGNITION STUDY	163
F. TEST PROCEDURES AND CHECKLIST FOR CRACK PROPAGATION	167
G. ERROR ANALYSIS	172

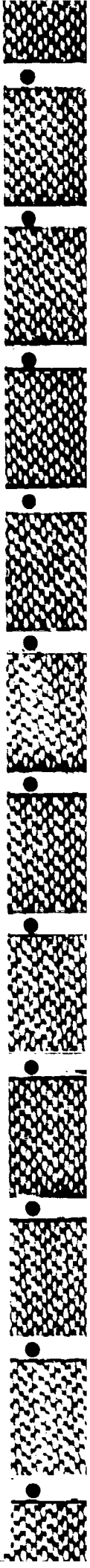
LIST OF FIGURES

<u>Figure</u>	<u>Page</u>
1. Physical and Chemical Processes in Composite Solid Propellant Ignition under Radiative Heating	19
2. Heterogeneous Structure of Nitramine Composite Propellants	20
3. Statistically Averaged Element and Finite Difference Grid Pattern	20
4. Physical and Chemical Processes in the Ignition and Combustion of Nitramine Composite Propellants	27
5. A Schematic Diagram of CO_2 Laser Ignition Test Setup	35
6. Low Pressure Chamber	37
7. A Schematic Diagram of Gas Control System	38
8. The CO_2 Laser	39
9. Configuration of Fine Wire Thermocouple Mounting	46
10. The Junction of Thermocouple (Pt-Pt13%Rh, $25\mu m$)	47
11. Schematic Diagram of Temperature Measurement	48
12. Schlieren Optical System	51
13. Delay Time for Onset of Light Emission (BLX4)	54
14. Delay Time for Onset of Light Emission (BLX8)	55
15. Delay Time for Onset of Light Emission (BLX9)	56
16. Delay Time for Onset of Light Emission (AP/HTPB)	57
17. Ignition Characteristics of BLX8($5\%O_2, 1a^*m$)	58
18. Flame Development of BLX8 ($\dot{q}'' = 700W/cm^2, 5\%O_2$)	61
19. Flame Development of BLX4 ($\dot{q}'' = 700W/cm^2, 1\%O_2$)	62
20. Flame Development of BLX4 ($\dot{q}'' = 700W/cm^2, 21\%O_2$)	63
21. Flame Structure Recorded by Conventional Video Camera	65
22. Schlieren Pictures and Direct Pictures	66-74
23. Surface Temperature vs. Time ($\dot{q}'' = 1000W/cm^2, He$)	76
24. Gas Temperature vs. Time ($\dot{q}'' = 600W/cm^2, He$)	77

25.	Surface and Gas Temperature vs. Time ($\dot{q}'' = 1000W/cm^2$)	78
26.	Surface and Gas Temperature vs. Time ($\dot{q}'' = 800W/cm^2$)	79
27.	Gas Temperature vs. Time ($\dot{q}'' = 800W/cm^2$)	80
28.	A Typical Output of Gas Chromatograph for Porapak Q and R Column	82
29.	A Typical Output of Gas Chromatograph for MS 5A Column	83
30.	Scanning Electron Micrographs of BLX4	86
31.	Crack Propagation Velocity versus Pressurization Rate	91
32.	Propellant Sample Configuration Before Loading	95
33.	Test Chamber	96
34.	Driving Motor	98
35.	Data Acquisition System	100
36.	Geometry of the Damaged Propellant Sample	104
37.	Relaxation Modulus Time Shift Factor versus Temperature	106
38.	Master Relaxation Curve	107
39.	Test Configuration for Crack Velocity Characterization	108
40.	Crack Propagation Velocity versus Stress Intensity Factor for ARC 4525	109
41.	Control Volume Used in Energy Analysis	112
42.	Pressure-Time Trace for DNICP 27	118
43.	Recovered Sample from DNICP 27	119
44.	Pressure-Time Trace for DNICP 40	120
45.	Film Record from DNICP 40	122
46.	Instantaneous Bright Film Contour From DNICP 40	124
47.	Crack Tip Location versus Time for DNICP 40	125
48.	Instantaneous Bright Film Contour From DNICP 31	124
49.	Data Correlation for the Extended Crack Length Π_A	130
50.	Data Correlation for the Rate of Increase in Specific Surface Area Π_B	131

51. Data Correlation for the Number of Macrocracks Π_C 132

52. Data Correlation for the Crack Propagation Velocity Π_D 133



LIST OF TABLES

<u>Table</u>		<u>Page</u>
I.	Composition of Test Propellants	42
II.	Thermophysical Properties of the Ingredients	43
III.	Molecular Structure of Major Ingredients	44
IV.	Film Interpretation of Crack Propagation Processes	123
V.	Steady-State Burning Rate Constants	127
VI.	Experimental Value of Dimensionless Parameters	128
VII.	Estimation of measurement Errors	173

NOMENCLATURE

<u>Symbol</u>	<u>Description</u>
A_b	Burning surface area in the affected region
A_{bt}	Total burning surface area
A_s	Specific burning surface area
a	Total crack length
a_o	Initial crack length
a_T	Time shift factor
b	Propellant sample thickness
c, c_p	specific heat
D	binary mass diffusion coefficient
E	activation energy, relaxation modulus or total energy
g	acceleration of gravity
h_p	Enthalpy of the propellant
h_t	Stagnation enthalpy of product gases
I	radiation flux
k	thermal conductivity
k_i	rate constants for reaction i
K_I	Stress Intensity Factor
K_{I_c}	Critical stress intensity factor
L	thickness of cylindrical pellet
L_D	Length of extended macrocrack
\overline{MW}	mean molecular weight of gas mixture
\dot{m}	Mass flow rate
\dot{m}_R	mass burning rate of RDX filler
\dot{m}_B	mass burning rate of binder
n	Number of macrocracks
P	pressure

\dot{q}''	heat flux (energy per unit time per unit area)
\dot{q}'''	heat generation rate (energy per unit time per unit volume)
$Q_{py,o}$	heat of pyrolysis per unit mass
\dot{Q}	Heat loss
r	radial distance from center of pellet
r_b	burning rate
R	gas constant
R_u	universal gas constant
R_1, R_2	radii of outer surfaces of filler and binder, respectively
R^2	Sample multiple coefficient of determination
T	temperature
t	time
v_z	gas phase velocity in z direction
V	Voltage
V_a	Affected volume
V_c	Chamber free volume
V_p	Crack propagation velocity
Y_j	mass fraction of species j
z	distance from gas-solid interface; positive in gas
Z	pre-exponential factor

Greek Letters

α	absorptivity or thermal diffusivity
β	in-depth radiation absorption coefficient
γ	Specific heat ratio
Γ	Fracture energy
ϵ	emissivity or strain
ν	Poisson's ratio
ξ	Shifted time

ρ	density
σ	Stress
σ_{fm}	Maximum stress in the failure zone
τ	transmissivity of solid phase
ψ_i	Crack cavity angle
ψ_o	Outside taper angle
$\dot{\omega}''$	mass production rate per unit area
$\dot{\omega}_i'''$	mass production rate per unit volume

Subscripts

1, 2, 3, 4, 5	various reactions of species
B	binder
g	gas phase
i	initial value or species
$pyro$	pyrolysis
R	RDX filler
rad	radiation
s	solid phase
$s - g$	solid-gas interface

ACKNOWLEDGEMENT

This research has been sponsored by the Office of Naval Research, Arlington, Virginia, under Contract No. N00014-79-C-0762. Dr. Richard S. Miller served as the technical monitor and program manager for this contract. His support of this research investigation is greatly appreciated. We would also like to acknowledge the encouragement of Mr. Tom Boggs of NWC for investigating nitramine propellant ignition. Appreciation is extended to Drs. E. C. Martin and Rena Y. Yee of the Naval Weapons Center for providing various types of nitramine propellants for this ignition study. Thanks are also due to Professor R. A. Schapery of Texas A. & M. University for useful exchange of ideas in crack propagation studies. The authors would also like to thank Mr. T. Torikai of Ashahi Chemical Ind. Co. of Japan for his assistance on this study.

I. INTRODUCTION

This is the final report summarizing the research investigation conducted during January 1, 1986 to August 31, 1987, under the project entitled "Ignition of Solid Propellants and Propagation of Burning Propellants Cracks" (Contract No. N00014-79-C-0762).

The major objectives of this investigation are: 1) to develop a comprehensive theory for the radiative ignition of nitramine composite propellants and to evaluate the theory by comparison with experimental results obtained in this investigation and 2) to examine propagation and branching processes in burning solid propellant crack samples. Specific objectives of this study are:

- 1) to determine the dependence of delay time for onset of light emission (t_{LE}) as a function of incident energy flux (\dot{q}''), ambient gas compositions, and ambient pressure;
- 2) to observe the site of initial light emission and flame development processes;
- 3) to measure gas-phase temperatures in the vicinity of the burning surface;
- 4) to study the surface structures of test samples recovered before and after onset of light emission;
- 5) to compare the ignition characteristics of a series of nitramine solid propellants with those of a conventional AP/HTPB propellant;
- 6) to develop a theoretical model and to obtain numerical solutions for ignition of nitramine composite propellants under CO_2 laser heating;
- 7) to validate the theoretical model with experimental data;
- 8) to study important parameters governing the laser ignition of nitramine composite propellants;

- 9) to define a group of meaningful dimensionless parameters for characterizing the operating conditions and resulting damage of a solid sample;
- 10) to obtain test data necessary for developing correlations between the dimensionless parameters; and,
- 11) to establish correlations, demonstrating a methodology for generating useful safety criteria.

II. LASER IGNITION OF NITRAMINE COMPOSITE PROPELLANTS

2.1 INTRODUCTION

2.1.1 General Statement of the Problem

Recently, solid propellant researchers have focused a good deal of attention on the study of nitramine composite propellants. Nitramine composite propellants offer several advantages: (1) high energy, (2) low combustion temperature, (3) low infrared emissions in the plume region, and (4) low vulnerability. However, most studies [1-11] have been focussed on steady-state combustion. Little effort has been directed to the study of ignition of nitramine composite propellants[12,13].

Radiative ignition techniques have been used widely for research and for testing the ignition characteristics of newly formulated propellants[14]. The radiative energy sources are usually produced from an arc image furnace or a CO₂ laser. The arc image furnace was a popular device for laboratory radiative ignition studies prior to development of the CO₂ laser. In recent years, the CO₂ laser has been more widely used in propellant ignition studies[15-18,28,29] due to several major advantages it offers over the arc image furnace[9]. The advantages of employing a CO₂ laser system for the study of pyrolysis and ignition are: (1) the energy flux to the propellant sample can be controlled with a high degree of reproducibility; (2) the environmental parameters, such as chamber pressure, initial temperature, and chemical composition of surrounding gases in a CO₂ laser ignition device, can be varied independently; and (3) the improved CO₂ laser beam intensity can reach a sufficiently high level to simulate the broad range of energy fluxes in propulsive devices.

The low vulnerability characteristics of composite propellants used in an ammunition system are important factors in screening newly formulated propellants. Low susceptibility to external thermal energy stimulation is a desirable feature of a Low Vulnerability Ammunition (LOVA) propellant. LOVA propellants should also possess proper ignitibility for propulsive purposes. Recently, Roller et al.[13] found that LOVA propellants can be ignited more effectively using oxidizer-rich ignition materials. This further substantiates the importance of the effect of ambient oxidizer concentration in the ignition processes of LOVA propellants. These ignition characteristics can be determined readily and accurately by using a high-powered CO₂ laser with well-controlled ambient gas composition.

Although radiative ignition of solid propellants drew extensive attention for more than three decades, it has its own inherent drawbacks. Ohlemiller and Summerfield [14] critically reviewed the radiative ignition of solid fuels. They found the most prominent drawback to be the lack of hot gas adjacent to the heated surface; this results in loss of the energy absorbed by the solid surface through conductive heat transfer to the adjacent cool ambient gas. Another major problem is that the radiative energy absorbed by the solid propellants is strongly dependent on the optical properties of propellants. Despite these disadvantages, radiative ignition is attractive.

The present study emphasizes achieving a better understanding of thermal pyrolysis, flame initiation, and flame development in the ignition of nitramine composite propellants.

2.1.2 Previous Related Studies

An extensive review of experimental and theoretical studies related to the radiative ignition of nitramine composite propellants is given in this section. Price et al.[19] reviewed the state of the art in solid propellant ignition theories published up to 1966. They also discussed experimental works related to theoretical approaches. Kulkarni et al.[20] also reviewed theoretical and experimental works on the ignition of solid propellants. Recently, Hermance[21] presented an excellent review covering work done after Price's 1966 review.

Experimental studies of radiative ignition will be reviewed first in the present study, followed by an examination of previous theoretical approaches to radiative ignition. Due to the importance of information from steady-state combustion of nitramine propellants to the ignition study of nitramine composite propellants, both experimental and theoretical studies on the combustion of nitramine propellants will be reviewed. Finally, since thermal decomposition of nitramines is an important process in the ignition of nitramine composite propellants, a brief review of thermal decomposition of nitramines and binders will be given in this section and will be discussed further in a later section.

2.1.2.1 Radiative Ignition - Experimental

Shannon[22] studied ignition characteristics of composite solid propellants using an arc-imaging furnace as a radiant energy source. He used AP-based composite propellants with different binders as test samples. A go/no-go test was used as an ignition criterion. The pressure range was 0.1 - 4 atm and the range of heat fluxes was 10 - 100 cal/cm² s. He defined the ignition process by considering two separate stages: (1) propellant inert heating, and (2) ignition of the volatile following

propellant heating. Thus, the ignition event can be divided into time intervals representing the two stages,

$$\tau_{ign} = t_T + t_c \quad (2-1)$$

where

τ_{ign} = total time to ignition

t_T = time of propellant heating by external energy source alone

t_c = time of heat addition by various chemical reactions plus time of transition to steady-state combustion.

The rate of volatile generation rises rapidly with temperature and will exceed any threshold value within a small temperature change. Therefore, ignition will usually occur when the solid reaches some fixed temperature, and the temperature will be substantially independent of heating rate and other parameters over a limited range. Shannon suggested that if a complete understanding of the ignition mechanism is to be attained, the kinetic processes affecting the chemical time, t_c , must be defined in greater detail. The purpose of his study was to explore the interrelationship among ignition characteristics and propellant compositional factors in order to determine chemical reaction sequences that may be important in determining t_c . He determined the minimum exposure times by using the go/no-go criterion. At low pressures, where ignition requires long exposure times, the exposure time was held constant and go/no-go limits of pressures were also determined.

Shannon[22] found that interfacial oxidation between oxidizer and binder was not important, and that gas-phase compositional and pyrolysis differences were more important than solid-phase or surface reactions. He concluded that gas-phase

reaction establishment is an important process in composite propellant ignition by radiant energy.

Summerfield and his associates[14-18] conducted a series of experiments to understand the behavior of composite propellants under radiative heating. They suggested an equation for prediction of ignition delay time in radiative ignition of composite propellants. They considered three dominant factors (conduction, in-depth radiation, and diffusion/reaction) in ignition delay, based on the value of radiant flux. At high energy flux, the delay time for chemical and diffusion processes in the gas phase is dominant. At low energy flux, condensed-phase heating dominates the ignition delay. In the upper range of the low energy flux, the in-depth absorption of radiation is more important than heat conduction. From the above reasoning, they proposed a simple equation for prediction of ignition delay time.

$$t_{ign} = t_{CD} + \alpha[\rho C \Delta T^* / (1 - r)F] + (\pi K/4)[\rho C \Delta T^* / (1 - r)F]^2 \quad (2 - 2)$$

where α is the sample absorption coefficient for the incident radiation, r the surface reflectance, K the thermal diffusivity, F the incident flux, and ΔT^* the temperature rise of the surface necessary to yield ignition. They did not elaborate on any method to obtain t_{CD} in Eq. (2-2). Thus, the equation is only qualitatively useful when processes subsequent to heating of the condensed phases dominate the ignition delay.

Ohiemiiler and Summerfield[15] examined the radiative ignition behavior of polymeric fuels with special reference to solid propellants. Polystyrene and an epoxy polymer in oxygen/nitrogen mixtures were studied. Ignition delay time was measured as a function of radiant flux, pressure, oxygen percentage, and fuel absorptivity. A continuous wave CO_2 laser was employed as an energy source to

eliminate some of complexities related to an arc image furnace. They found that as the oxygen partial pressure in the ambient gas increases, the ignition delay time decreases. At the upper limit of oxygen partial pressure, ignition delay becomes independent of this variable. As the oxygen partial pressure is decreased, the ignition delay time increases until it approaches a no-ignition limit. They also studied the effect of a surface opacifier(carbon black) on ignition delay. They found that the addition of the opacifier not only reduced ignition delay time, but made the slopes of ignition delay vs. incident energy graphs steeper.

Ohlemiller et al.[16] extended their radiative ignition studies to investigate the dynamic response of a solid propellant to rapidly varying radiative fluxes. They found that when a CO₂ laser is used as an energy source, a flame was sustained only during the external laser heating, and was extinguished when the incident laser beam is cut off. They also found that the tendency to extinction upon deradiation is reduced by increasing pressure or increasing the time interval for reducing the energy flux to zero. They proposed a mechanism to explain this phenomenon. A short deradiation interval produces a corresponding rapid decrease in surface gasification rate and a relatively fast decrease in heat feedback from the flame. However, the condensed phase acts as if it has inertia, and cannot respond instantaneously to a change in heat feedback from the flame. Accordingly, the high condensed-phase temperature gradient, previously established by the external radiation, persists and causes a relatively large fraction of heat to be conducted out of the gas phase. This diminishes the flame intensity. Thus, there is a competition between condensed-phase conduction processes that decrease the temperature gradients at the condensed-phase surface, and the weakened ability of the flame to be sustained as the condensed phase adjusts to the reduced heating rate. They also proposed a

theoretical model to simulate the extinction of the flame with removal of incident laser energy.

In their two-part study, DeLuca et al.[17-18] examined the ignition response of several propellants under radiative heating and the influence of the radiation source (arc image vs. laser) on observed ignition behavior. In the first part of the study[17], they emphasized the influence of propellant formulation on ignition behavior. They found that comparisons of the chemical factors in the formulation can only be made properly when the optical factors are minimized. They also found that the HMX composite was most difficult to ignite among the propellant samples tested, and followed by AP-based composite and double-base propellants. In the second part of the study[18], pre-ignition events and effects of the nature of the radiation source were emphasized. They found that fast deradiation extinction occurs only with the laser, not with the arc image furnace.

Kashiwagi[23-25] used a CO₂ laser in a series of experiments to study radiative ignition of polymethylmethacrylate (PMMA) and red oak. He found strong attenuation of incident laser radiation by the plume consisting of decomposition products in the gas phase. He postulated that PMMA ignites by absorption of incident radiation by decomposition products in the gas phase. He also found that the attenuation of radiation caused by decomposition products in the gas phase was significant enough to affect surface temperature.

Kashiwagi and Ohlemiller[26] studied oxygen effects on nonflaming transient gasification of PMMA and PE during thermal radiation. The presence of oxygen in the gas phase was found to increase the mass flux from PMMA and PE significantly. However, the effect of oxygen on mass flux was apparently reduced as the counterflow of decomposition gases grew. Kashiwagi and Ohlemiller[27] also used a

CO₂ laser to study the ignition mechanism of a liquid fuel under radiation heating.

Mutoh et al.[30] conducted an experimental study to explore the behavior of the radiative ignition of PMMA. A CO₂ laser was used as an energy source. They found a critical energy flux above which ignition occurred at the plume axis away from the PMMA surface, and below which it occurred at the edge of the plume near the sample surface. They suggested that determining *a priori* the ignition criterion is impossible, and that it is necessary to explore the heat and mass fluxes throughout the solid and gas phases in order to predict ignition. Beckel and Matthews[33] also used a CO₂ laser to study the radiative ignition of polyoxymethylene (POM). They found the effect of oxidizer supply in the ambient gas on ignition delay time of POM to be significant.

Recently, the application of high power lasers to gun systems as practical initiation devices has been attempted[31,32]. Laser ignition systems for large caliber guns were found to offer possibilities for improved performance and reliability. Ostrowski et al.[31-32] employed a laser to study ignition characteristics of gun propellants. They used a pulsed ruby laser to ignite the propellants. They found that proper adjustment of the laser energy deposition rates produced a certain degree of self-confinement of the flame which then allowed sustained combustion to occur.

2.1.2.2 Radiative Ignition - Theoretical

General ignition theories have been reviewed extensively by Price et al.[19] and Hermance[21]. In this section, some recent radiative ignition models are reviewed.

Kashiwagi[34] proposed a theoretical model describing radiative ignition of a solid fuel. He included the effects of gas-phase reaction and in-depth absorption of the incident radiation by the solid fuel. From the results of his theoretical inves-

tigation, he established a range of pyrolysis activation energies for ignition as well as the importance of gas-phase reaction and in-depth radiation. He also found that the effects of ambient inert gas on the ignition delay time are significant. His model demonstrates some important aspects of radiative ignition; however, the application is limited to pure fuel ignition.

Kumar and Hermance[35] presented a radiative ignition model of a homogeneous propellant. The decomposed gas from the solid phase is a homogeneous mixture of fuel and oxidiser. They found that the gas-phase reactions are important in establishing a gas-phase flame, but their influence in evaluating the ignition behavior of the propellant is negligible. They suggested that only at very low pressures and extremely high heating rates do the gas-phase processes become important. Although this model can handle the ignition of a homogeneous propellant, the applicability to a composite propellant is questionable.

Kumar[36] further extended the radiative ignition model[35] to include the two-dimensional nature of composite propellants. In this model, the diffusion of species and energy was considered two-dimensional. The propellant was considered to be opaque. Thus, no in-depth radiative heating was considered. Although the prediction of this model agreed with some of the experimental observations in other cases, predictions regarding the pressure dependence of ignition delay in inert atmospheres did not agree.

Phuoc and Durbetaki[37] formulated a set of boundary layer equations which included the absorption of external radiation by the gas phase. They used the empirical equations derived from Kashiwagi's experiments[24]. They could predict the discontinuity in ignition time observed in Mutoh's experiments[30].

Kindelan and Williams[38] employed an asymptotic method for ignition of a

solid fuel. They included in their analysis the endothermic gasification of the solid fuel and exothermic reactions in the gas phase. In-depth absorption of the external radiant energy flux was also considered. The advantage of using an asymptotic method is the availability of parametric studies. However, the applicability of the asymptotic technique is limited, especially when the properties of the materials are dependent on the other variables.

2.1.2.3 Combustion of Nitramine Propellants

McCarty et al.[1] conducted a study to determine the combustion behavior of nitramine propellants. They studied the effects of solid loading and particle size on the burning rate of HMX composite propellants. They found a slope break on the burn-rate curve near 136 atm. They also found that with coarse particles, the HMX protruded from the quenched surface, while fine particles produced a smooth surface. This was attributed to ignition delay of coarse particles. With coarse particles, the heat transfer between particles is reduced due to the relatively longer distance between particles.

Kubota et al.[2] studied the combustion characteristics of nitramine and AP composite propellants. They found that the replacement of AP with nitramines decreased the burning rate. They also observed that the effect of the particle size of nitramines on burning rate was not significant. Kuwahara and Kubota[4] extended the study to low-pressure combustion in order to observe combustion wave structures.

Kubota[3] also investigated the combustion mechanisms of nitramine composite propellants to determine controlling parameters of the burning rate in the combustion wave. He found that the combustion wave structure was homogeneous due to

the melt layer formed by RDX and binder. He also observed a preparation zone, similar to a dark zone in the combustion of a homogeneous propellant, whose height strongly depended on the ambient pressure. From thermocouple measurements, he concluded that the effect on the burning rate of heat feedback from the luminous flame was negligible in comparison to heat released at the burning surface.

The effects of binders on burning rates and thermal wave structures of HMX composite propellants were investigated by Kubota[5]. The thermal structure of propellants with a high-oxygen content binder was homogeneous due to the formation of a molten layer of HMX/binder on the burning surface. The flame structure of HMX propellants was found to be a two-stage flame consisting of two reaction zones. The first-stage reaction zone, which appears just above the burning surface, is equivalent to the fizz zone of double-base propellants; the second stage, i.e., the preparation zone, is equivalent to the dark zone of double-base propellants. The luminous flame that appears some distance above the burning surface is produced by the second stage reaction. The luminous flame and the preparation zone were distinguished by measurement on microphotographs and microthermocouples. However, the thermocouple outputs were not synchronized with the high-speed microphotography.

The combustion of HMX-based propellants was also studied by Cohen-Nir[7]. From his cinemicrography study, he argued that previous speculations regarding the ejection of HMX particles from the burning surface were erroneous.

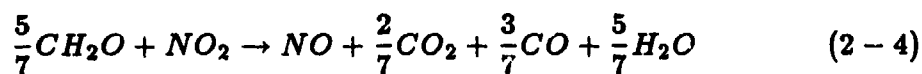
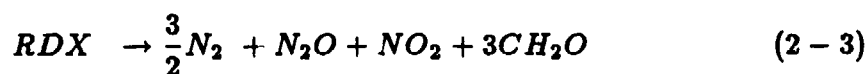
Baumann et. al[39] and Harris[40] measured the temperature distribution and transient species concentrations in the reaction zone of an RDX-based composite propellant using Coherent Anti-Stokes Raman Scattering (CARS) to provide information for the evaluating the reaction mechanism in the decomposition of nitramine

propellants. The species identified were N_2 , H_2 , CO , CO_2 , HCN , and NO . The propellant flame consisted of three zones: an inner dark zone, a bright yellow intermediate zone, and an outer blue zone. The inner dark zone, which is about 4mm thick in air at 1 atm, is the reaction zone near the solid-gas interface where the surface temperature is around 900 ± 100 K. In this zone, large percentages of CO and H_2 are formed. The final products were identified as N_2 , H_2 , CO , and CO_2 ; intermediate species such as N_2O and NO_2 were not observed. Baumann and his coworkers claimed that the intermediate NO_2 at atmospheric pressure was not observable with their CARS apparatus. Despite the fact that no NO_2 species were measured, they suggested that the initial step of the thermal decomposition of nitramines is the loss of NO_2 to form a dinitro-RDX radical, which further undergoes stepwise degradation to form n-nitroformimine ($H_2C = N - NO_2$) and HCN . At low temperatures (below 600 K), CH_2O and N_2O form, whereas at higher temperatures (above 700 K), HCN and N_2O form. Based upon the existence of moderate quantities of HCN , they believed the high-temperature pathway to be the major route for thermal decomposition of RDX near the surface of the propellant. This is consistent with the decomposition mechanism considered by Boggs[48] and Schroeder[43]. They concluded that the luminous flame due to conversion of NO to N_2 was too far away to provide to the burning surface the heat that determines the burning rate. They believed that the heat feedback from the gas-phase reactions of RDX and HCN controlled the burning rate.

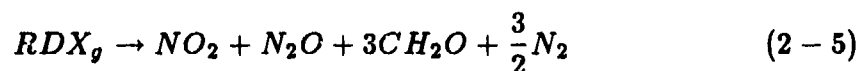
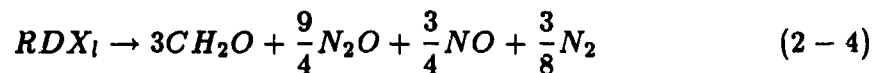
Parr and Hanson-Parr[41] investigated the chemistry and kinetics of the ignition and combustion of HMX using PLIF(Planar Laser Induced Fluorescence). They measured species and temperature profiles during CO_2 laser ignition and steady-state deflagration of HMX. They obtained time-resolved PLIF images for

NO_2 , NO , CN , NH , H_2CO , OH , and OH rotational temperatures during ignition and deflagration of HMX. CN and NH were found in a delayed gas-phase ignition kernel which rapidly reformed into a thin flame sheet. They concluded that NO and NO_2 were initial decomposition products which were consumed in a flame in which CN and NH were transient radical by-products.

A theoretical combustion model of nitramine propellants was proposed by Ben-Reuven et al.[8-10]. For the deflagration of RDX, they proposed two overall reaction steps:



The proposed mechanism included (1) the decomposition of RDX in the liquid phase, (2) the primary gas-phase reaction following vaporization and gas-phase decomposition, and (3) oxidation of CH_2O by NO_2 that is the secondary gas-phase reaction. In the early phase of their work[8], they assumed Eq.(2-2) to hold for both gas- and liquid-phase decomposition of RDX. The reaction scheme was modified later[10] to consider different reaction mechanisms for the liquid phase and gas phase:



They found that the near-field region with its dominant primary decomposition is fundamental in controlling heat feedback to the propellant surface.

2.1.3 Scope of the Present Work

The main objective of this investigation is to develop a comprehensive theory for the radiative ignition of nitramine composite propellants and to evaluate the theory by comparison with experimental results obtained in this investigation. The scope of the present work for theoretical and experimental approaches is presented below.

2.1.3.1 Theoretical Approach

The specific objectives of the theoretical study are:

- 1) to develop a theoretical model and to obtain numerical solutions for ignition of nitramine composite propellants under CO₂ laser heating;
- 2) to validate the theoretical model with experimental data;
- 3) to study important parameters governing the laser ignition of nitramine composite propellants.

2.1.3.2 Experimental Approach

The specific objectives of the experimental study are:

- 1) to determine the dependence of delay time for onset of light emission (t_{LE}) as a function of incident energy flux (\dot{q}''), ambient gas compositions, and ambient pressure;
- 2) to observe the site of initial light emission and flame development processes;
- 3) to measure gas-phase temperatures in the vicinity of the burning surface;
- 4) to study the surface structures of test samples recovered before and after onset of light emission; and

5) to compare the ignition characteristics of a series of nitramine solid propellants with those of a conventional AP/HTPB propellant.

2.2 THEORETICAL APPROACH

2.2.1 Description of Physical Model

Physical processes involved in radiative ignition of composite solid propellants are complex. Figure 1 shows a schematic diagram of various thermophysiochemical processes involved in the radiative ignition of composite solid propellants. In the initial inert heating period, incident radiative energy heats up the solid propellant material without involving any chemical reactions. Once the surface temperature of the propellant reaches a certain point, a significant amount of gas is generated from the pyrolysis of the condensed-phase propellant. A melt layer may be formed before massive pyrolysis occurs. As the pyrolyzed gas product is moving away from the propellant surface, a part of the incident external radiative energy is absorbed by the pyrolyzed gas. A portion of the radiative energy reaching the propellant surface is reflected away from the surface. The remainder of the radiative energy penetrates into the propellant and is absorbed by the condensed phase. Pyrolyzed gas of the RDX filler may undergo a primary monoflame. The gas product of the primary flame diffuses and reacts with the diffusing decomposed gas from the binder. Diffusion of external oxidizing gas may accelerate the gas-phase chemical reactions.

The heterogeneous structure of nitramine composite propellants is shown in Fig. 2. The physical model of the present study considers an RDX filler particle embedded in the binder matrix. The shape of the filler particles is approximated by a cylindrical pellet of radius R_1 and thickness L , enveloped by a binder of radius R_2 . Figure 3 shows the statistically averaged element and finite difference grid pattern.

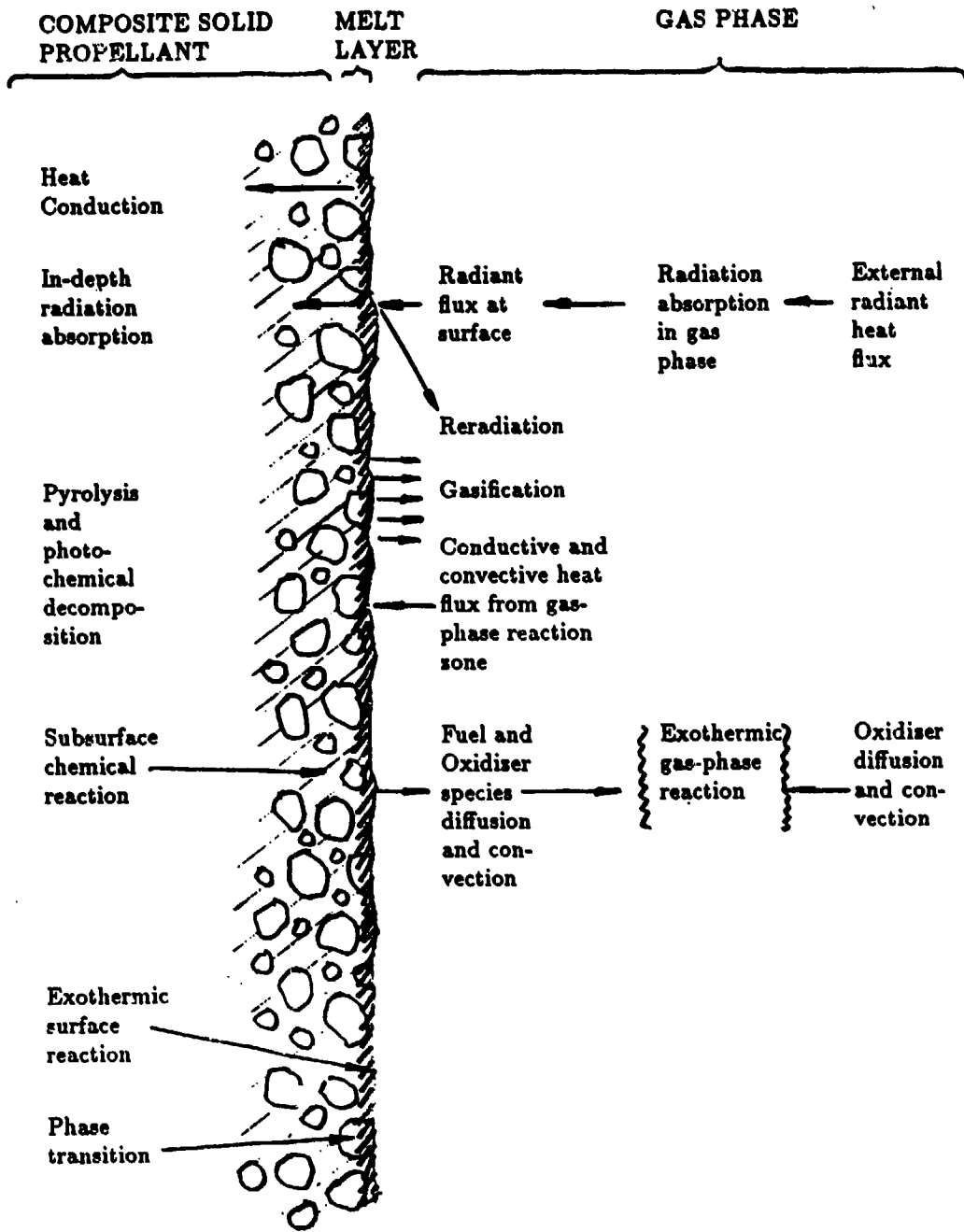


Fig. 1. Physical and Chemical Processes in Composite Solid Propellant Ignition under Radiative Heating

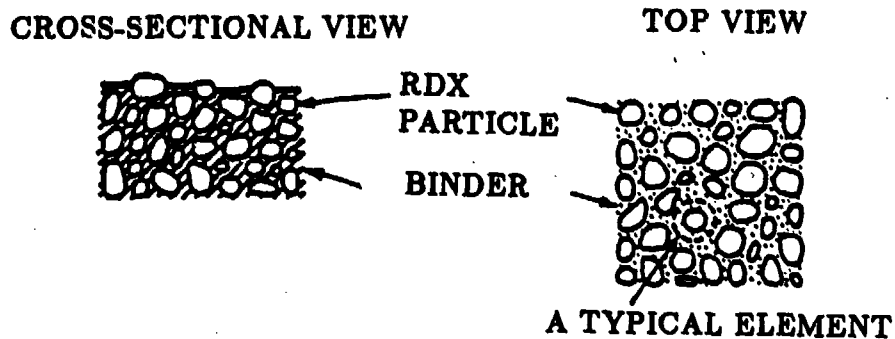


Fig. 2 Heterogeneous Structure of Nitramine Composite Proeplants

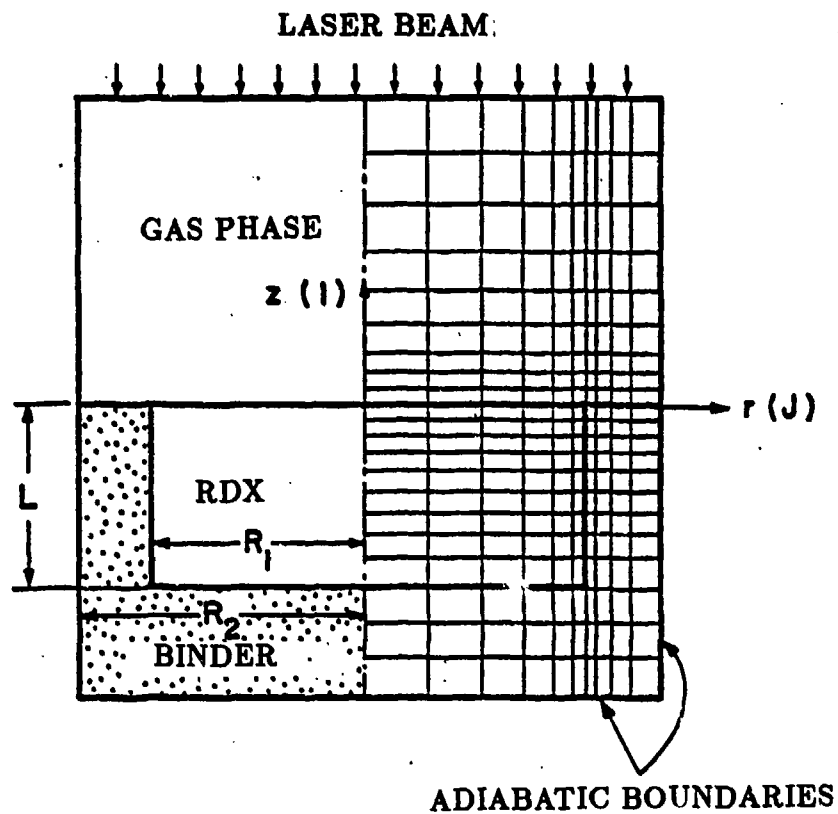


Fig. 3 Statistically Averaged Element and Finite Difference Grid Pattern

2.2.2 Assumptions

The following assumptions are employed in the mathematical model:

- 1) The solid propellant and gas phase are two-dimensional and axisymmetric.
- 2) The gas pressure is constant.
- 3) The gas-phase chemical reactions can be described by second-order Arrhenius kinetics.
- 4) The pyrolysis processes are expressed by single zero-order reactions of the Arrhenius Law.
- 5) The gas mixture obeys the perfect gas law.
- 6) The specific heat of all gaseous species is assumed to be the same and constant.
- 7) The binary diffusion coefficients of all gaseous species are equal.
- 8) The incident radiation is absorbed in-depth by the solid phase satisfying Beer's Law.
- 9) The radial bulk velocity is much smaller than the axial.
- 10) The thermal properties of the solid are independent of temperature.
- 11) The Lewis number is unity.

The assumption of a two-dimensional geometry closely represents a composite propellant, while being mathematically tractable. Since there is no external driving force for the ambient gas for radiative ignition, the pressure of the ambient gas is nearly constant. This assumption eliminates the momentum equations. The assumptions for the gas-phase chemical reactions are due to the lack of knowledge of the complex chemical reactions in the gas phase and the prohibitive computational time involved. Further discussion will be presented in subsequent sections, and as further information is gathered, the more refined reaction schemes will be incorporated. The pyrolysis mechanisms of RDX filler remain controversial even

after extensive studies of the mechanisms. This subject will be discussed further in a later section. Assumptions (5), (7), and (11) are standard in combustion studies. Assumptions (6) and (10) are made to simplify the problem. Assumption (9) holds true for radiative ignition.

2.2.3 Mathematical Model

2.2.3.1 Governing Equations and Boundary Conditions

The mathematical model consists of governing equations for the solid-phase and gas-phase regions. In the solid phase, two energy equations are considered; one for the RDX filler and the other for the binder. Source terms in these equations include contributions due to in-depth radiation absorption and pyrolysis. The energy equations are coupled to the gas-phase conservation equations through the heat-flux balance at the solid-gas interface. Gas-phase behavior is described by mass, energy, and species conservation equations. For the RDX-based composite propellants, five different species (CH_2O , NO_2 , RDX vapor, gaseous binder, and products) are considered to be present in the gas phase.

Solid Phase Energy Equations

RDX filler:

$$\rho_{R,s} c_{R,s} \left(\frac{\partial T}{\partial t} + \frac{\dot{m}_R}{\rho_{R,s}} \frac{\partial T}{\partial z} \right) = \frac{\partial}{\partial z} \left(k_{R,s} \frac{\partial T}{\partial z} \right) + \frac{1}{r} \frac{\partial}{\partial r} \left(k_{R,sr} r \frac{\partial T}{\partial r} \right) + \dot{q}_{R,rad}''' + \dot{q}_{R,pyro}''' \quad (2-6)$$

Binder:

$$\rho_{B,s} c_{B,s} \left(\frac{\partial T}{\partial t} + \frac{\dot{m}_B}{\rho_{B,s}} \frac{\partial T}{\partial z} \right) = \frac{\partial}{\partial z} \left(k_{B,s} \frac{\partial T}{\partial z} \right) + \frac{1}{r} \frac{\partial}{\partial r} \left(k_{B,sr} r \frac{\partial T}{\partial r} \right) + \dot{q}_{B,rad}''' + \dot{q}_{B,pyro}''' \quad (2-7)$$

where

$$\dot{q}_{j,rad}''' = -\frac{\partial I}{\partial z} = \beta_j I_o (1 - \rho_{r,j}) e^{\beta_j y},$$

$$\dot{q}_{j,\text{pyro}}''' = -Z_{j,\text{pyro}} Q_{j,\text{pyro}} \exp(-E_{j,\text{pyro}}/R_u T),$$

and

$$j = R(\text{RDX}) \text{ or } B(\text{binder}) \quad (2-8)$$

Gas-Phase Equations

The gas-phase conservation equations are

Continuity:

$$\frac{\partial \rho_g}{\partial t} + \frac{\partial}{\partial z} (\rho_g v_z) = 0 \quad (2-9)$$

Energy:

$$\rho_g C_p \frac{\partial T}{\partial t} + \rho_g C_p v_z \frac{\partial T}{\partial z} = \frac{\partial}{\partial z} \left(k_g \frac{\partial T}{\partial z} \right) + \frac{1}{r} \frac{\partial}{\partial r} \left(k_g r \frac{\partial T}{\partial r} \right) + \dot{q}_g''' \quad (2-10)$$

Species:

$$\rho \frac{\partial Y_j}{\partial t} + \rho_g v_z \frac{\partial Y_j}{\partial z} = \frac{\partial}{\partial z} \left(\rho_g D \frac{\partial Y_j}{\partial z} \right) + \frac{1}{r} \frac{\partial}{\partial r} \left(\rho_g D r \frac{\partial Y_j}{\partial r} \right) + \dot{\omega}_j''' \quad (2-11)$$

where $j = 1, 2, 3$ or 4 for the gaseous species CH_2O , N_2O , RDX vapor, and binder pyrolysis gas, respectively.

The source terms \dot{q}_g''' and $\dot{\omega}_j'''$ are obtained by using chemical kinetics information described in a later section. The equation of state for the gas phase is

$$\rho_g = \frac{PMW}{R_u T} \quad (2-12)$$

Initial and Boundary Conditions

The initial condition for the solid phase (both RDX and binder) is

$$\text{at } t = 0 : T(0, r, z) = T_i \quad (2-13)$$

Boundary conditions for the solid phase are as follows. The temperature far from the interface is the same as the propellant initial temperature, i.e.,

$$\text{at } z \rightarrow -\infty : T = T_i \quad (2-14)$$

Temperature continuity at various interface requires

$$T|_{r=R_1^+} = T|_{r=R_1^-} \quad (2-15)$$

and

$$T|_{z=-L^-} = T|_{z=-L^+} \quad (2-16)$$

On symmetric surfaces, adiabatic conditions are

$$\text{on } r = 0 : \frac{\partial T}{\partial r} = 0 \quad (2-17)$$

$$\text{on } r = R_2 : \frac{\partial T}{\partial r} = 0 \quad (2-18)$$

At solid-gas and RDX-binder interfaces, the heat flux balance gives

$$\text{at } z = z_{s-g} : k_s \frac{\partial T}{\partial z} \Big|_{z_{s-g}^-} = k_g \frac{\partial T}{\partial z} \Big|_{z_{s-g}^+} + \alpha_{s-g} I + r_{b,s} \rho_s T (c_{p,s} - c_{p,g}) + \dot{q}_{s-g}'' \quad (2-19)$$

where \dot{q}_{s-g}'' is the net heat generation at the interface.

$$\text{at } z = -L = k_{B,s} \frac{\partial T}{\partial z} \Big|_{-L^-} = k_{R,s} \frac{\partial T}{\partial z} \Big|_{-L^+} + \alpha_{R-B} \tau_R I_0 e^{-\beta_R L} \quad (2-20)$$

$$\text{at } r = R_1 \text{ and } -L < z < 0 : -k_{b,s} \frac{\partial T}{\partial r} \Big|_{R_1^+} = -k_{r,s} \frac{\partial T}{\partial r} \Big|_{R_1^-} \quad (2-21)$$

Initial conditions for the gas-phase equation (for $j = 1, 2, 3,$ and 4) are

$$\text{at } t = 0 : v_z(0, r, z) = 0; T(0, r, z) = T_{g,i}; \text{ and } Y(0, r, z) = Y_{j,i} \quad (2-22)$$

Boundary conditions for the gas phase are as follows. The symmetric conditions at the centerline and outer boundary give

$$\text{at } r = 0 : \frac{\partial T}{\partial r} = 0; \quad \frac{\partial Y_j}{\partial r} = 0 \quad (2-23)$$

and

$$\text{on } r = R_2 : \frac{\partial T}{\partial r} = 0; \quad \frac{\partial Y_j}{\partial r} = 0 \quad (2-24)$$

Far away from the surface,

$$z \rightarrow \infty : \frac{\partial T}{\partial z} = 0; \quad \frac{\partial Y_j}{\partial z} = 0 \quad (2-25)$$

The temperature continuity at the interface gives

$$\text{on } z = z_{s-g} : T \Big|_{z_{s-g}^+} = T \Big|_{z_{s-g}^-} \quad (2-26)$$

The overall and individual species mass-flux balance at the solid-gas interface is given as follows.

$$\text{on } z = z_{s-g} : \rho_g v_x = \rho_s r b_s \quad (2-27)$$

and

$$\rho_g v_x Y_j |_{z_{s-g}-} = \rho_g v_x Y_j |_{z_{s-g}+} - \rho_g D \frac{\partial Y_j}{\partial z} - \dot{\omega}_j'' \quad (2-28)$$

2.2.3.2 Physiochemical Consideration for Pyrolysis and Ignition

Description of Physical and Chemical Processes

Physical and chemical processes involved in the ignition and combustion of nitramine composite propellant are described below. Figure 4 shows a general diagram compiled from various studies of nitramine propellant decomposition, ignition, and combustion. It is evident that the ignition and combustion of nitramine composite propellants involves many complex physical and chemical processes. When heated by ambient gases, the solid-phase nitramine crystal and binder undergo inert heating in the subsurface region. Near the surface of the nitramine crystal, phase transitions may occur. Decomposed radicals could be trapped between molecules or within molecules. This produces the so-called "Cage Effect" proposed by Fifer[49]. Trapped radicals can recombine due to their close proximity and low mobility. This recombination process is generally believed to be the reason for the higher activation energy of solid-phase decomposition than that of liquid-phase or gas-phase decompositions. It was reported by Brill[50] that the phase transition has an activation energy similar to that of solid-phase decomposition. He postulated that the rate controlling step of solid-phase thermal decomposition is due to disruption of inter molecular forces.

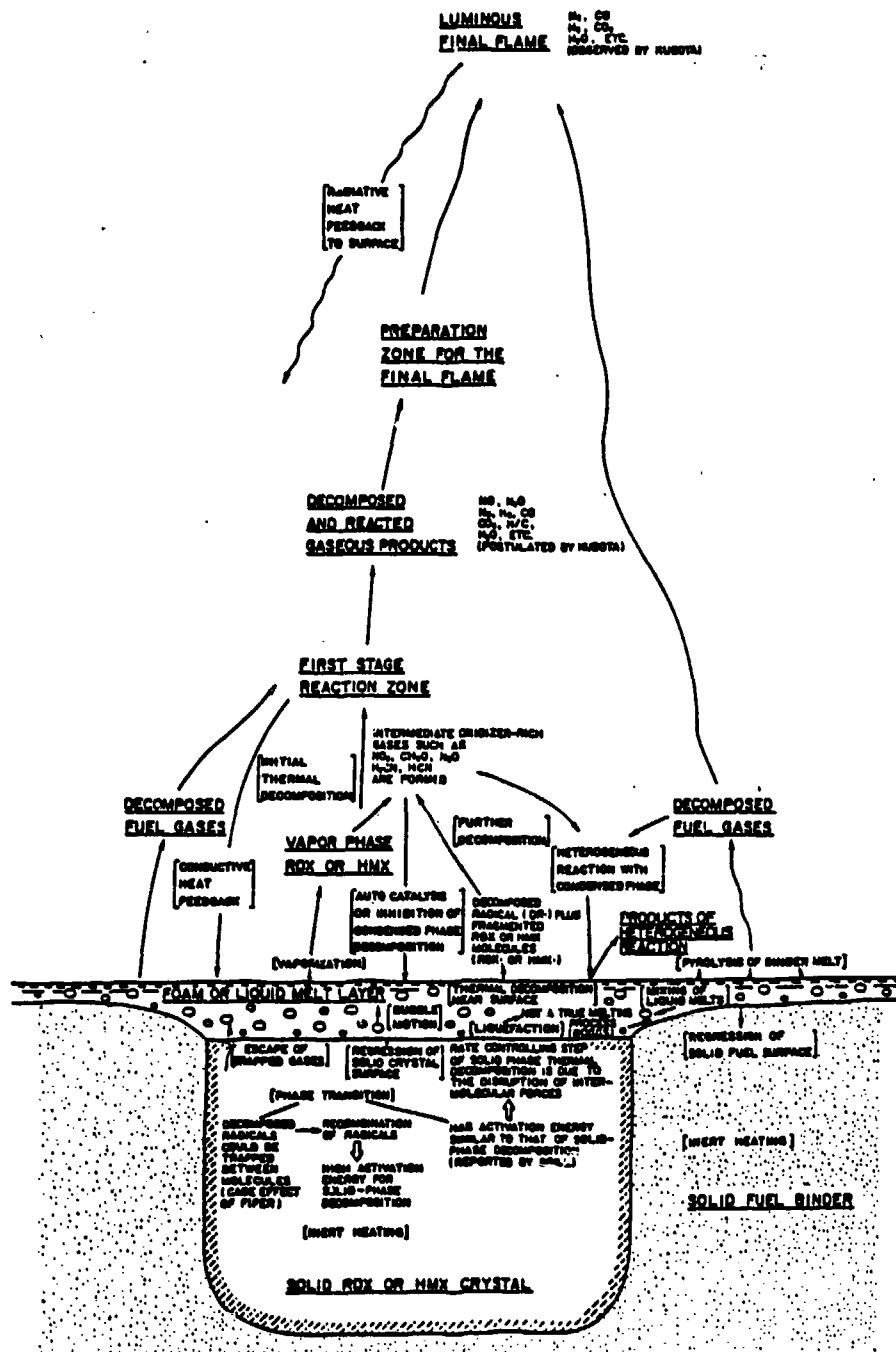


Fig. 4. Physical and Chemical Processes in the Ignition and Combustion of Nitramine Composite Propellants

At the interface between the gas phase and condensed phase, a foam or liquid melt layer could form above the solid-phase crystal and binder. The foam layer may contain various sizes of bubbles. The melt layer of the nitramine filler could form at a temperature lower than the melting point of pure nitramine. This phenomenon was called "liquefaction" by Boggs[48]. Boggs stressed that liquefaction is not a true melting process. A melt of nitramine filler and binder could be mixed to form an energetic melt layer. Vaporization of the liquid melt can occur on the surface of the melt layer. In the meantime, thermal decomposition of the nitramine filler in the liquid phase can yield decomposed radicals and fragmented nitramine molecules in the initial decomposition step. Further decomposition of the gaseous species formed at the initial step and vapor-phase decomposition will yield slightly oxidizer-rich gases. Some of the gaseous species from the oxidizer-rich gases could attack the surface of the melt layer. Chemical species of the oxidizer-rich gases will react with each other exothermically to form the first-stage reaction zone. Before reacting in the final flame, the gaseous products from the first-stage reaction zone may pass a preparation zone where reaction kinetics are retarded. The gaseous species from the preparation zone and the decomposed fuel gases will react eventually to form the final luminous flame.

Radiative heat could be transferred from the luminous flame to the first reaction zone and the foam or melt layer. Simultaneously, conductive heat feedback to the condensed-phase surface from the first reaction zone will occur. The mechanisms depicted in Fig. 4 are based upon observations and a physical understanding of the ignition and combustion processes.

Thermal Decomposition of Nitramine

Since it has been considered that the overall chemical processes in the deflagra-

tion of nitramine composite propellants are dominated by thermal decomposition of pure nitramine, extensive studies have been conducted on the subject. Schroeder[43-47], Boggs[48], Fifer[49], and Dubovitsii and Korsunskii[58] reviewed the literature on the kinetics and reaction mechanisms of the thermal decomposition of nitramines, especially RDX and HMX. Despite extensive studies on the thermal decomposition of RDX and HMX, the detailed mechanisms are generally unknown. Even the initial step(s) of the reaction is controversial.

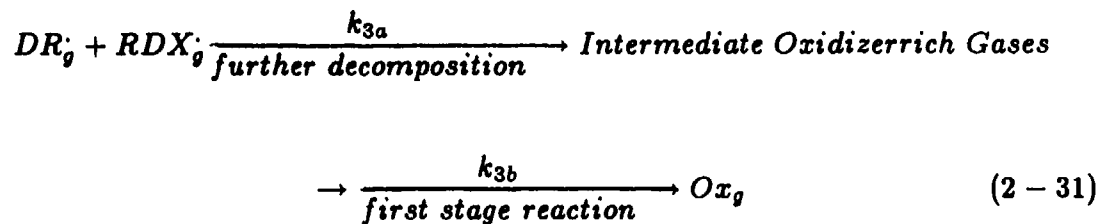
Various mechanisms proposed have been critically reviewed by Schroeder[43-47]. An excellent arrangement of the probable mechanisms has been prepared by Shaw and Walker[59]. The main question concerning the primary step (or steps) of thermal decomposition of RDX and HMX is whether it is $N - N$ bond fission or $C - N$ bond cleavage. Fission of $N - NO_2$ bond has generally been considered as an initial step of the decomposition mechanism of RDX and HMX. Growing evidence has shown that $C - N$ bond cleavage occurs first, identified mostly by mass spectroscopic [60,61] and labelling studies accompanying rapid pyrolysis[62]. The initial decomposition schemes are (1) elimination of CH_2NNO_2 , (2) $N - NO_2$ fission, (3) homolytic $C - N$ cleavage, (4) *HONO* elimination, (5) concerted depolymerization to 4 CH_2NNO_2 , and (6) transfer of an oxygen atom from an $-NO_2$ group to a neighboring group.

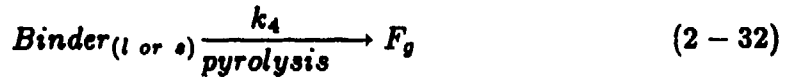
A mechanism proposed by Karpowicz, Gelfand, and Brill[50] is quite different from those of covalent bond cleavage. Based on observations of their phase transition experiments, it was proposed that disruption of intermolecular electrostatic forces (rather than covalent bond cleavage) controls the rate of thermal decomposition of HMX. As mentioned above, Fifer also postulated the "Cage Effect," which represents an induced recombination of radicals generated in the initial dissociation

step. He suggested that cage escape (the escape of decomposed gaseous species from the condensed region) might be rate-controlling for the condensed-phase decomposition. In general, both Fifer and Brill consider intermolecular actions to be dominant factors in condensed-phase decomposition.

Kinetic Model

Based on the information discussed above, a kinetic model was constructed. The reaction mechanisms used in the present model can be extended to include various initial decomposition mechanisms discussed previously. The initial step can be $N - NO_2$ fission, $C - N$ bond cleavage, $HONO$ elimination, or other mechanisms. The present investigation considers the following five representative chemical reactions: (1) vaporization of nitramine filler followed by thermal decomposition to form oxidizer-rich gases, (2) initial thermal decomposition of liquid phase nitramine to form decomposed radicals ($DR\cdot$) and fragmented RDX ($RDX\cdot$), (3) further decomposition of $RDX\cdot$ to form intermediate oxidizer-rich gases which then react in the first-stage reaction to form Ox_g , (4) binder pyrolysis to form fuel-rich gases, and (5) reaction of Ox_g and F_g to form final products in luminous flame:





Depending upon the options considered for radical initiation, $DR\cdot$ could represent NO_2 , CH_2NNO_2 , $HONO\cdot$ or any other reactive species. Some of the kinetic data required as input for the thermal decomposition of nitramine filler is available from various decomposition experiments. Other kinetic constants such as k_5 required for the above reaction model must be based upon the kinetic data of similar reactions.

2.2.3.3 Modeling of Source Terms

In order to solve the governing equations, source terms (\dot{q}'' , \dot{q}_g''' , $\dot{\omega}_i''$, and $\dot{\omega}_i'''$) must be expressed as functions of other variables and known parameters. In modeling the source terms, it is implicitly assumed that the rate-controlling reaction rate constants have Arrhenius dependence on local temperature and are given by

$$k = zT^m e^{-E/R_u T} \quad (2-34)$$

The gas-phase mass fractions, Y_1 , Y_2 , Y_3 , Y_4 , and Y_5 , represent the RDX vapor, NO_2 , CH_2O , binder decomposed gas, and products, respectively. The source terms can be expressed as follows:

$$\dot{\omega}_1''' = Z_3 \frac{W_1}{W_2 W_3} \rho_g^2 T \exp(-E_3/R_u T) - Z_5 \frac{1}{W_4} \rho_g^2 Y_1 Y_4 \exp(-E_5/R_u T) \quad (2-35)$$

$$\dot{\omega}_2''' = Z_3 \frac{1}{W_3} \rho_g^2 Y_2 Y_3 T \exp(-E_3/R_u T) \quad (2-36)$$

$$\dot{\omega}_3''' = \dot{\omega}_2''' \frac{W_3}{W_2} \quad (2-37)$$

$$\dot{\omega}_4''' = -Z_5 \frac{1}{W_1} \rho_0^2 Y_1 Y_4 \exp(-E_5/R_u T) \quad (2-38)$$

$$\dot{q}_g''' = (\dot{\omega}_2''' \Delta H_3 + \dot{\omega}_4''' \Delta H_5) \quad (2-39)$$

where ΔH_3 is the heat of reaction per unit mass of RDX for the reaction of Eq.(2-31), and ΔH_5 is the heat of reaction per unit mass of fuel for the reaction of Eq.(2-33).

2.2.3.4 Transformation of Governing Equations

In view of the large temperature and species concentration gradients near the propellant surface, a coordinate transformation is used to obtain an exponential finer grid size in the transformed coordinates. The following exponential transformation is used for the axial coordinate.

Solid phase:

$$s = \exp(A_s Z) - 1 \text{ or } Z = \frac{1}{A_s} \ln(1 + s), (-\infty \leq Z \leq 0) \quad (2-40)$$

Gas phase:

$$s = 1 - \exp(-A_g Z) \text{ or } Z = \frac{1}{A_g} \ln(1 - s), (0 \leq Z \leq \infty) \quad (2-41)$$

This transforms $Z = -\infty, 0, \infty$ to $s = -1, 0, 1$, respectively. The radial coordinates remain unchanged.

2.2.4 Numerical Method

An implicit finite difference scheme was used to solve the governing equations. A central difference scheme was used to approximate axial derivatives. A three-point, variable mesh, Allen's method was employed to represent radial derivatives, because the conventional central-difference scheme does not accurately represent radial derivatives when the radial coordinate is very small. Time derivatives were approximated by a generalized Crank-Nicolson scheme. A quasilinearization technique was used to linearize the inhomogeneous terms of governing equations. The resulting set of simultaneous finite-difference equations are being solved by a successive overrelaxation iterative scheme.

2.3 EXPERIMENTAL APPROACH

2.3.1 Introduction

An experimental investigation of the laser ignition of nitramine composite propellants was initiated to explore the physical and chemical processes involved in interactions between an incident laser beam and composite propellants. Observations and understandings gained from these experiments are useful in developing new igniter systems, and are very important for validating proposed ignition models. Thus, the experimental approach was carefully selected, based on the possibility of the comparison with theoretical results. Knowledge obtained from this radiative ignition can be extended to the ignition processes under other types of energy transfer modes, either convective, conductive, or combinations of the three different types of energy transfer modes.

In this chapter, the experimental apparatus and their operations will be discussed in the first section. Then, the data acquisition system will be discussed, followed by the description of the propellant samples used in the experiment. The laser-beam intensity distribution which is important in defining the energy flux to the sample surface is discussed next. The examination of beam-intensity distribution will be followed by description of the techniques used in measuring both temperature and gaseous species. Finally, the schlieren technique used for visualization of gasification and flame development will be discussed.

2.3.2 Experimental Apparatus and Operation

The schematic diagram of the CO₂ laser ignition test setup is shown in Fig. 5. A low-pressure ignition test chamber, 250 x 250 mm and 250 mm high, is mounted on an X-Y positioning bed to provide convenience in aligning the laser beam on

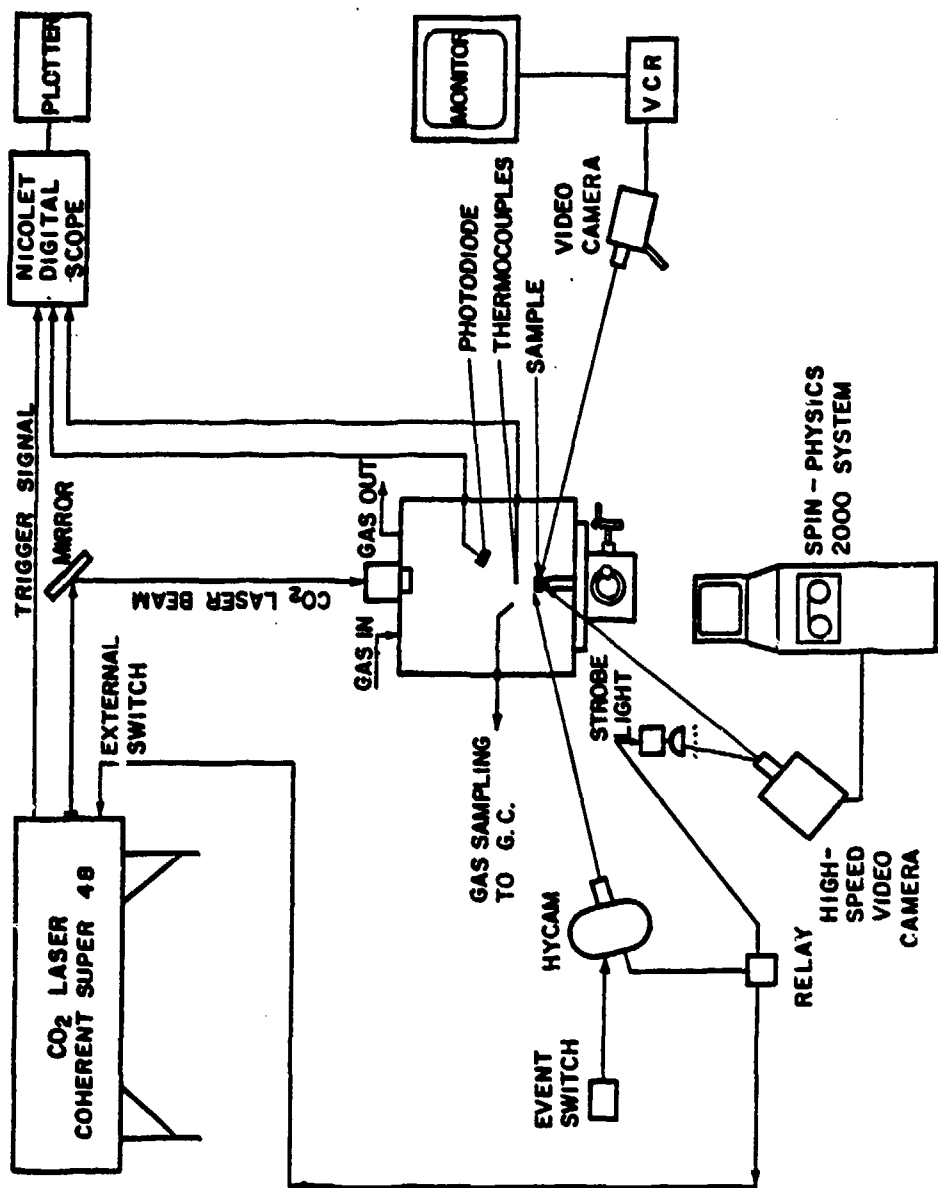


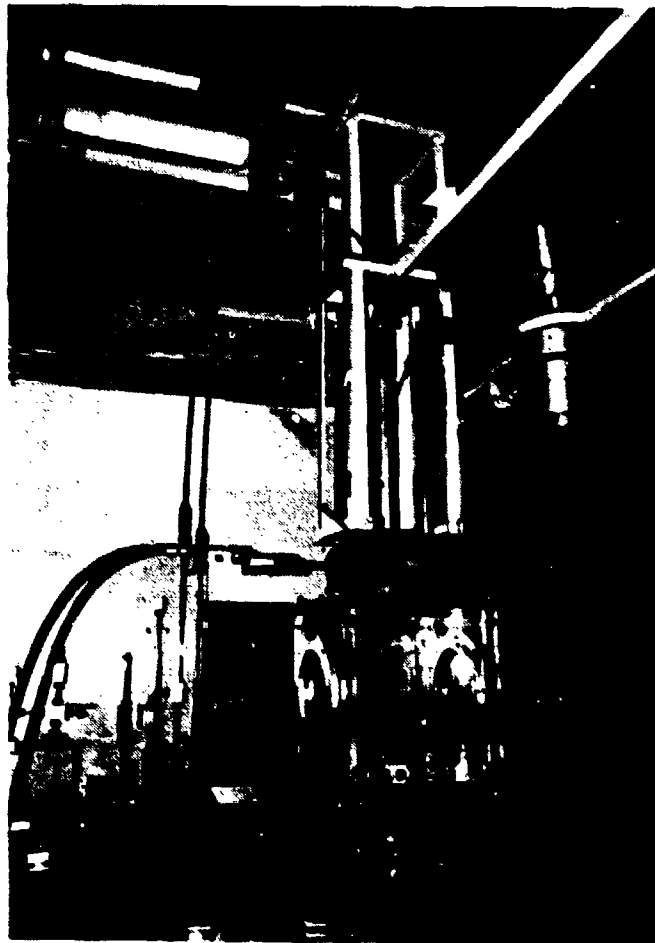
Fig. 5 A Schematic Diagram of CO₂ Laser Ignition Test Setup

the test sample. The propellant sample is mounted on a black-anodized aluminum sample holder located at the center of the test chamber. In order to minimize pressure change during the ignition test, the size of the test chamber was designed to be large enough so that the effect of the product gas generated from the sample on the chamber pressure during the test would be negligible. The gas supply line to provide different gases, and the purge line to remove the combustion gas products, are connected to the stainless steel top cover of the test chamber.

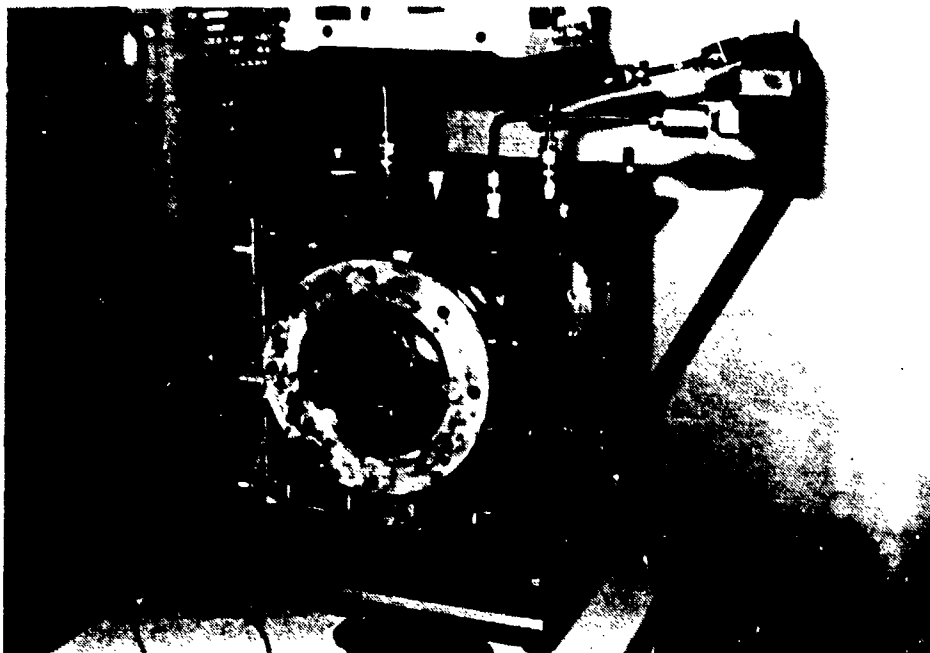
The four side walls of the low-pressure chamber, suitable for a pressure range of 10^{-3} to 2 atm, were fabricated with plexiglass (Fig. 6). The transparent side walls of the chamber provide full access to ignition events from all directions. The feedthroughs for the photodiode, thermocouples, and gas-sampling probes are mounted on the side walls of the chamber. For schlieren photography, a pair of schlieren quality windows were mounted on the two opposite side walls of the test chamber. The CO_2 laser beam reaches the propellant sample by passing through the KCl window mounted on top of the chamber. A gas control system (Fig. 7) was also designed and constructed to provide the desired initial gas composition and chamber pressure.

A high-powered Coherent Super 48 CO_2 laser (Fig. 8) is used as a radiant energy source for the ignition study of nitramine composite propellants. The maximum power of the CO_2 laser is 800 W in the CW mode, and 3500 W in the pulsed mode. The laser time can be controlled precisely by preselecting the time period of irradiation. The CO_2 laser generates a signal to trigger all the data acquisition systems.

The CO_2 laser beam generated from the laser system travels through a beam delivery system consisting of a series of silicon mirrors. The laser beam is confined



a) Overall View



b) Close-up View

Fig. 6. Low Pressure Chamber

CO₂ LASER IGNITION
A SCHEMATIC DIAGRAM OF GAS CONTROL SYSTEM

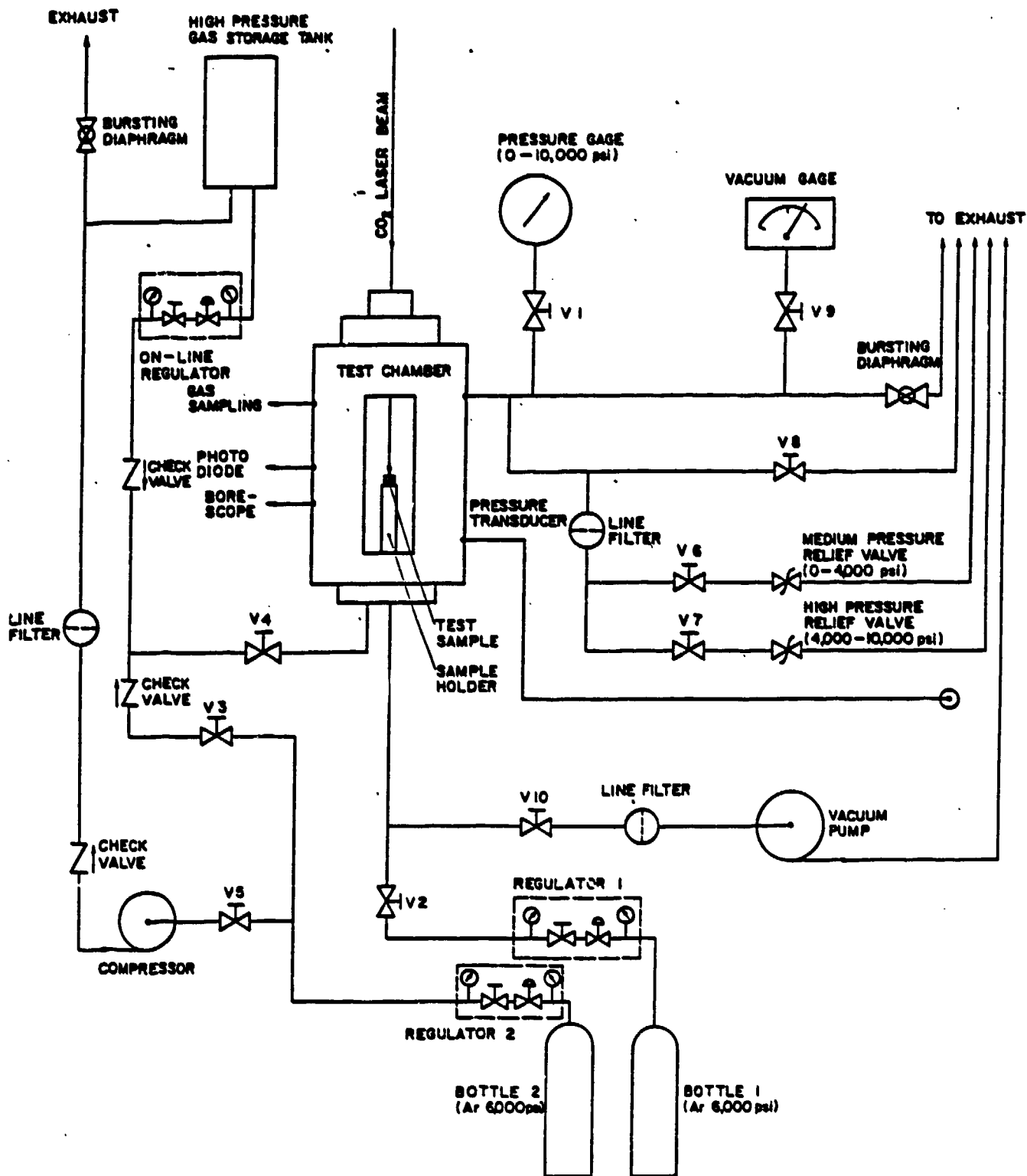
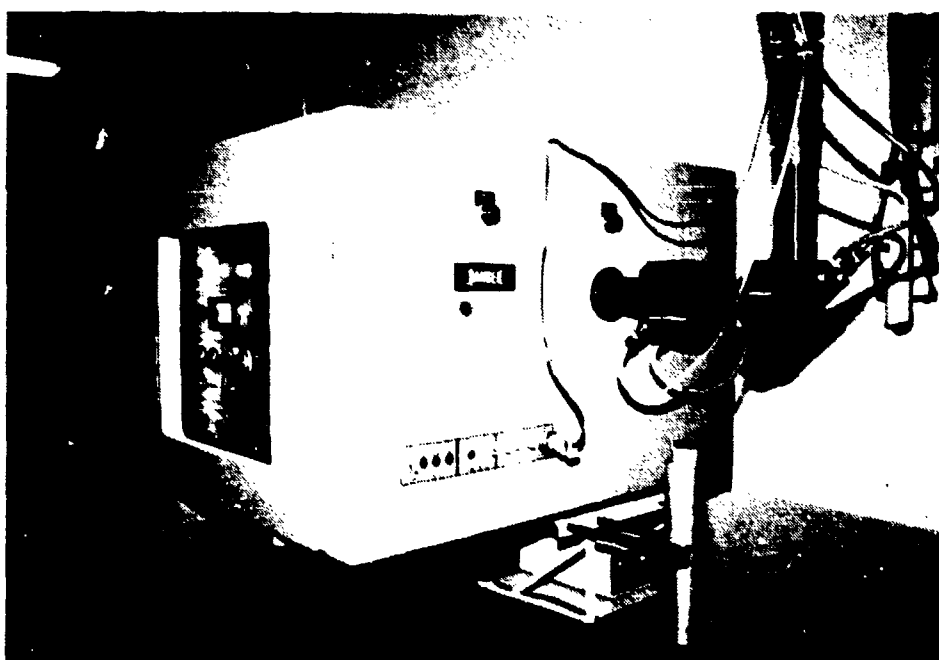


Fig. 7 A Schematic Diagram of Gas Control System



a) Side View



b) Front View

Fig. 8. The CO_2 Laser

within the anodized beam guiding tubings. Since the CO₂ laser beam is invisible (wave length = 10.6 μm), a beam combiner was designed and fabricated to combine the invisible CO₂ laser beam with an He-Ne laser beam so that the two beams travel together. One of the major advantages in combining an He-Ne laser with a CO₂ laser is to provide convenience in beam alignment.

2.3.3 Data Acquisition and Analysis Systems

Three different types of cameras (a high-speed video camera, a high-speed movie camera, and a conventional video camera) are used to observe flame initiation and development. A Spin-Physics 2000 high-speed video camera (12,000 pps max.) is used to film flame development. A quick review of the recorded ignition events is possible with this high-speed video system, and the recorded images can be analyzed on the monitor by moving reticle lines. Data can be transferred to an advanced Qauntex image analyzer for processing and storage. A high-speed movie camera (HYCAM 44,000 pps max.) is used to obtain a more detailed record of gas evolution and flame development during pyrolysis and ignition. A conventional video camera system, despite its low filming rate (ca. 25 pps), is also useful in observing the overall event in relatively good spatial resolution. In addition to the movie cameras, a silicon photodiode is used to detect the onset of first light emission.

Data from the thermocouples and the photodiode are recorded on a Nicolet digital oscilloscope. The data recorded by the Nicolet oscilloscope is stored on floppy diskettes, and then transferred to an IBM-AT microcomputer. The transferred data is processed and analyzed by the microcomputer and plotted on a laser-jet printer.

2.3.4 Propellant Samples

The composition and thermophysical properties of the ingredients of the propellant samples used in this study are given in Tables I and II. Three different types of RDX-based LOVA propellants (BLX4, BLX8, and BLX9) processed at the Naval Weapons Center(NWC) are tested. (BLX stands for baseline explosive.) Both BLX4 and BLX9 propellants contain RDX fillers and GAP binder, but with different energetic plasticizers (TMETN and BTTN, respectively). BLX8 propellant contains RDX filler and GAP binder, but no energetic plasticizers. The RDX particles in the BLX-series propellants are divided in two different classes: classes A and E. The average size of the particle in the class E is $4\mu\text{m}$, while class A contains a wide range of particle-size distribution. In order to compare the ignition behavior of BLX-series of nitramine propellants with conventional AP-based composite propellants, a propellant processed at Atlantic Research Corporation (ARC) with 73% AP (average particle size = $20\mu\text{m}$) and 27% HTPB was also used.

2.3.5 Beam Intensity Distribution

In order to define the incident energy flux to the sample surface, a uniform distribution of laser-beam intensity is desired. The intensity distribution of the CO_2 laser beam was examined by using a fine wire thermocouple and a pyroelectric detector. A fine wire thermocouple was mounted on a pole attached to an x-y positioning bed. The thermocouple travelled through the laser beam while measuring the intensities of the beam at different equally spaced locations. Since the exposure time of the thermocouple to the beam was sufficiently short, the slopes of the thermocouple signals were quite straight, indicating that the convective cooling effect of the thermocouple was negligible. The relative magnitude of the incident energy flux was determined based on the slopes of the signals. Since the heat-transfer

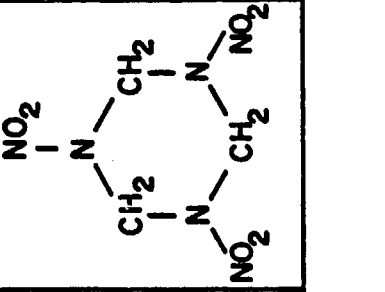
Table I. Composition of Test Propellants

Propellant Samples	BLX-4	BLX-6	BLX-8	BLX-9	NOS-A
Ingredients					
Filler	RDX (75%)	RDX (73%)	PDX (68%)	RDX (66%)	RDX (79%)
Main Binder Ingredients	TMETN GAP N-100	EHA VP DOM	GAP N-100	BTTN GAP N-100	CTPB

Table II. Thermophysical Properties of the Ingredients

Properties Ingredients	Molecular Weight (Kg/Kmol)	Density (Kg/m ³)	Heat of Formation (Kcal/Kg)	Heat of Combustion (Kcal/Kg)	Heat of Explosion (Kcal/Kg)	Melting Point (C)	Vapor Pressure (Pa)
RDX	222.	1820.	66.19 ~95.9	2.285	1439.	204.	-
GAP	2455.	1300.	13.85	-4.854	-	-	-
BTIN	241.	1520.	-371.2	2.168	1420.	-27.	.147
TMEIN	255.	1470.	-389.	2.542	1236.	-3.0~ -17.5	.017

Table III. Molecular Structure of Major Ingredients

INGREDIENTS	RDX	GAP	BTTN	TMETN
<p style="text-align: center;">MOLECULAR STRUCTURE</p> 	$\text{HO} \left[\text{CH}_2 \underset{\text{CH}_2\text{N}_3}{\text{CHO}} \right]_n \text{H}$	$\begin{array}{c} \text{H}_2\text{C}-\text{O}-\text{NO}_2 \\ \\ \text{H}_2\text{C} \\ \\ \text{HC}-\text{O}-\text{NO}_2 \\ \\ \text{H}_2\text{C}-\text{O}-\text{NO}_2 \end{array}$	$\begin{array}{c} \text{H}_2\text{C}-\text{O}-\text{NO}_2 \\ \\ \text{H}_3\text{C}-\text{C}-\text{CH}_2-\text{O}-\text{NO}_2 \\ \\ \text{H}_2\text{C}-\text{O}-\text{NO}_2 \end{array}$	

mechanism from the laser to the thermocouple is quite complicated, no attempt was made to determine the absolute amount of the energy flux. A pyroelectric detector (PZT 350), in conjunction with a chopper whose frequency was 100 Hz, was used to verify the intensity distribution measured by the fine-wire thermocouple. The profile of beam intensity distribution showed that a low intensity region exists near the center of the beam.

Two different approaches were taken to achieve uniformity of beam intensity distribution. The combination of a Kaleidoscope and a rotating mirror was one method used to average the original laser beam. The other technique was to modify the intensity distribution with a mask made of thin stainless steel. The latter method proved to be more convenient and effective.

The intensity level of the laser beam was also examined using the pyroelectric detector. An initial transient peak was observed. However, the delay time and the magnitude of the initial transient was not considered significant to the ignition test results.

2.3.6 Temperature Measurement

The surface temperature and thermal wave structure in the gas phase during the ignition of propellants are very important in understanding the mechanism of pyrolysis and ignition. A fine wire thermocouple technique was used to measure the temperatures of the propellant surface and the gas evolved from the sample surface during laser irradiation. Figure 9 shows the configuration of the thermocouples mounted with a propellant sample. The fine wire thermocouple (dia. 25 μm Pt-Pt/13%Rh) was supported by thicker extension wires. Since the gas products escaping from the sample surface can push the thermocouples upward, lead weights

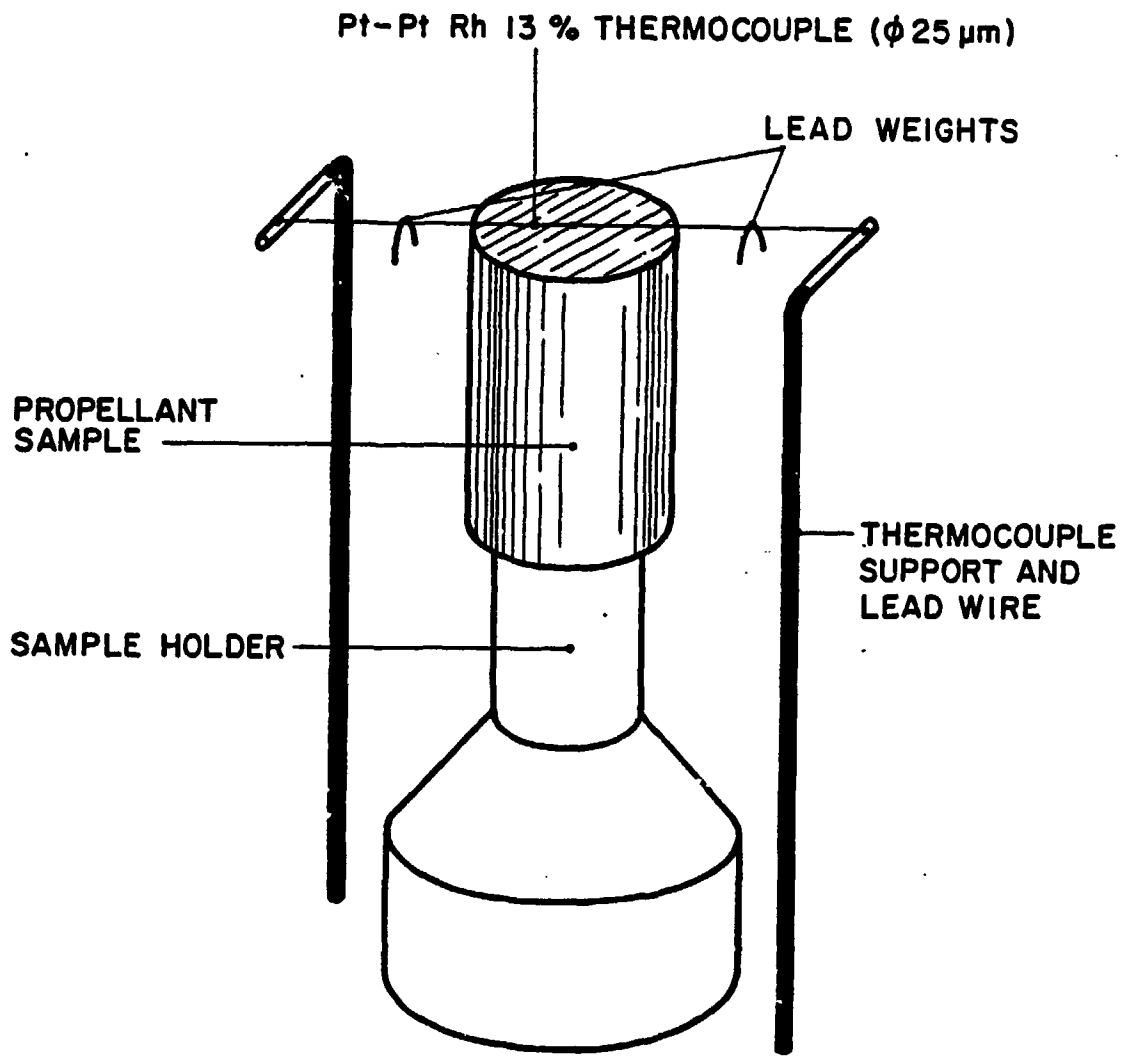


Fig. 9 Configuration of Fine Wire Thermocouple Mounting

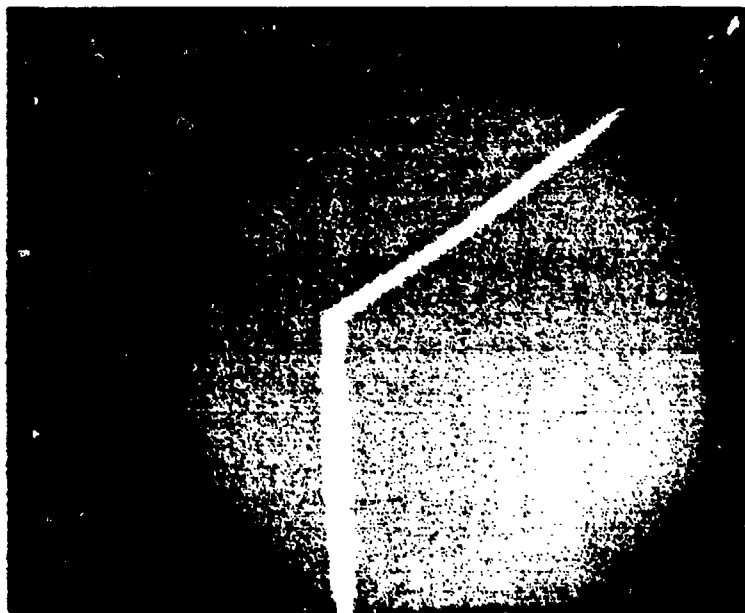


Fig. 10. The Junction of Thermocouple (Pt-Pt13%Rh, $25\mu m$)

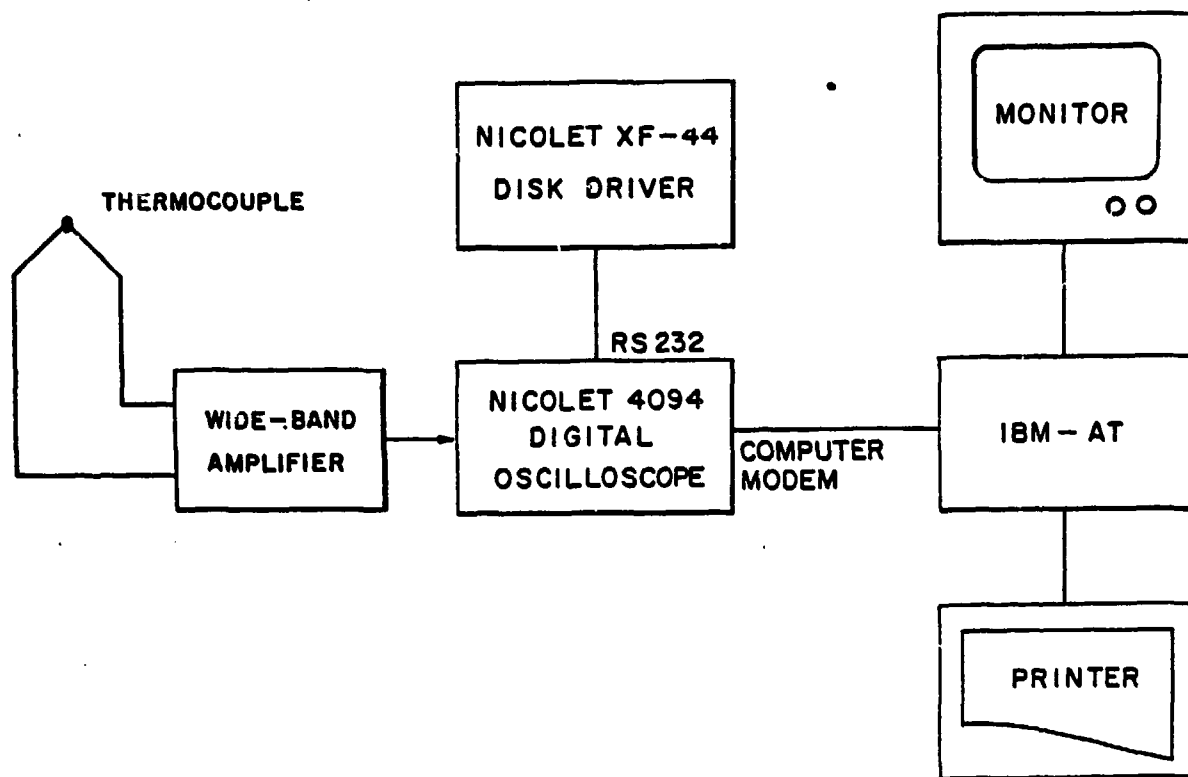


Fig. 11 Schematic Diagram of Temperature Measurement

were suspended on the thermocouple wires to maintain the location of the thermocouple junctions. Figure 10 shows the magnified view of the thermocouple junction. In order to minimize the size of thermocouple bead, a constant current technique was used to weld the thermocouple wires. Signals generated from the thermocouples were recorded on a Nicolet oscilloscope through an amplifier. Data recorded by the scope was processed and analyzed by an IBM-AT microcomputer. Figure 11 shows the schematic diagram of the temperature recording and processing system.

2.3.7 Gas Species Measurement

Analysis of the composition of the gas products from the pyrolysis and ignition of solid propellants is important to understanding the reaction mechanisms governing the processes. A Varian 3700 Gas Chromatograph was used to analyze the gaseous species generated from the sample during pyrolysis and ignition. Gas samples were taken through the gas sampling port. The stable species from the product gases were detected by using two different types of columns: a molecular sieve (MS 5A) and a series of Porapak Q and R. In order to minimize further reactions of the initial decomposed gases, low pressure conditions were chosen for the pyrolysis study. A GC/MS system was also used to confirm the peaks observed in the gas chromatography.

2.3.8 Surface Structure Observation

Scanning electron micrography was used to examine the surface structures of propellant samples before and after exposure to CO₂ laser radiation. The micrography provided important clues in determining the relative response of the RDX filler and the binder systems to the incident laser beam. It was also important in ascertaining the existence of an energetic melt layer during ignition processes.

2.3.9 Schlieren Technique

One of the common visualization techniques for the study of combustion phenomena is schlieren photography. Observations of the detailed gas evolution and mixing are possible using a schlieren optical system during pyrolysis and ignition of the propellant samples. Figure 12 shows the configuration of the schlieren system used in this study. The "Z" type schlieren optical system employs two parabolic first-surface mirrors, each with a diameter of 6 inches. The light source is a continuous tungsten-halogen lamp. When a Spin-Physics high-speed video camera is used to record the events, a monochromatic visualization technique is used. A color schlieren technique developed by Professor Gary S. Settles was used to take pictures with a high speed movie camera.

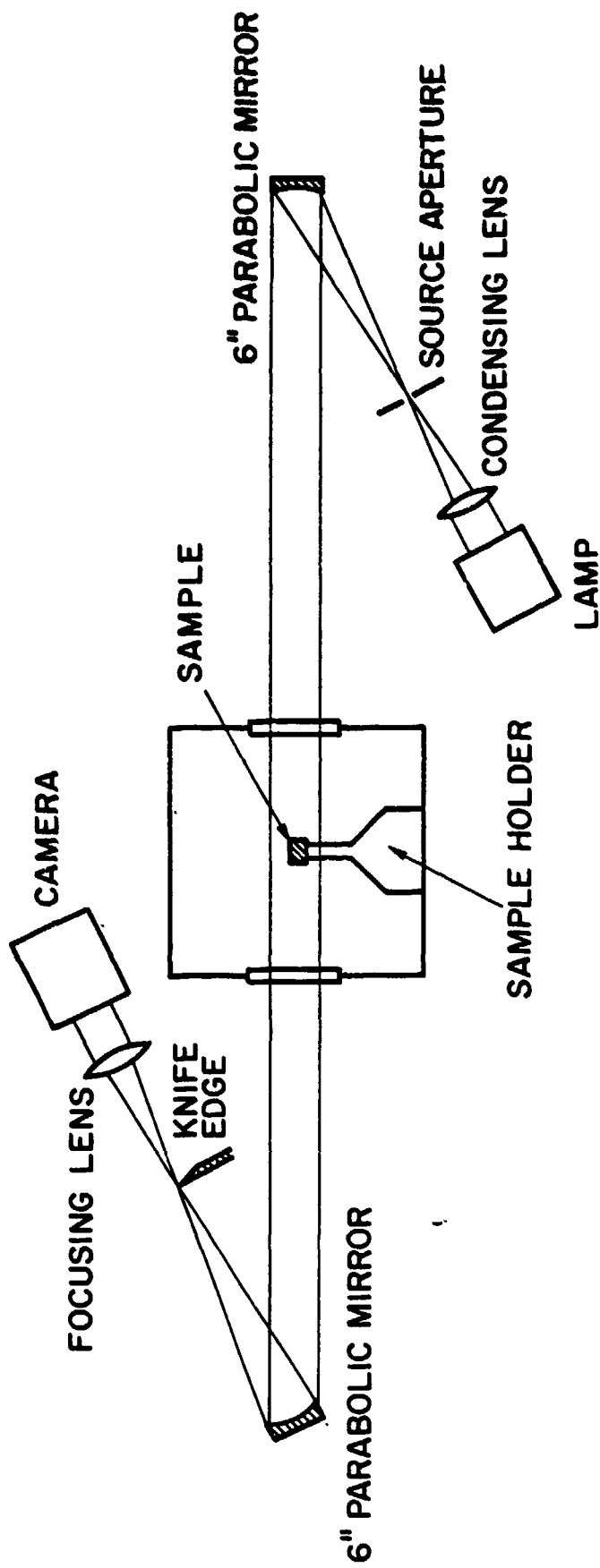


Fig. 12 Schlieren Optical System

2.4 RESULTS AND DISCUSSION

2.4.1 Experimental Results

In this section, the delay times for onset of light emission are presented and discussed. The effect of oxygen concentration in the ambient gas on delay times is also discussed. Gas evolution, flame initiation, and flame development are examined from direct and the schlieren pictures recorded by high-speed video camera, high-speed movie camera, and conventional video camera. Surface temperatures and the thermal wave structure of the gas phase are presented and discussed to explain the thermal processes that occur during pyrolysis and ignition of nitramine composite propellants. Analysis of product gases generated from the test propellants can reveal the mechanisms of chemical reactions involved in the pyrolysis and ignition. Results of the gas analysis by a gas chromatography are discussed. Examination of the optical and scanning electron microscope(SEM) pictures of the propellant surfaces before and after test illustrates the effects of incident energy fluxes.

2.4.1.1 Ignition Delay Time

Delay times for the onset of light emission in the gas phase were determined from photodiode signals. The data obtained by the photodiode were compared with the delay times estimated from analysis of the video pictures recorded by the Spin-Physics high-speed video camera.

Figure 13 shows the measured delay times of the BLX4 propellant as a function of incident laser energy fluxes for three different oxygen concentrations in the ambient gas. The data for 1%, 5%, and 21% O_2 show the same trends: the delay time decreases as the energy flux increases. For 21% O_2 , the delay times are shorter than those at lower oxygen concentrations. This indicates that the oxygen in the

ambient gas participates in the chemical reactions that produce a luminous flame. The slope of the curve for the 21% O_2 case is less steep than those for the 1% and 5% cases. As the incident energy increases, the effect of the oxygen concentration on delay time becomes less pronounced. For the lower oxygen concentration case (1% and 5% O_2), no luminous flame in the gas phase was observed below about 600 W/cm^2 .

The delay times for BLX8 are given in Fig. 14. For 5% O_2 , a luminous flame was observed in a narrow range of the energy flux. At the lower oxygen concentration (1% O_2), a luminous flame was barely visible. For 21% O_2 , a slope break was found at the incident energy flux of about 700 W/cm^2 . It is believed that the mechanisms dominating the gas-phase reactions are changing across that boundary. The effect of the absorption of the incident laser energy by the gaseous products may become significant at higher energy fluxes.

Figure 15 shows the delay times of the BLX9 propellant samples. The delay times of BLX9 are quite similar to those of BLX4. The slope of the delay times of BLX9 at 21% O_2 is slightly flatter than that of BLX4.

At 21% oxygen, the t_{LE} vs. q'' curves for BLX4 and BLX9 propellants with energetic plasticizers present different trends from those of BLX8. At the higher energy fluxes and the higher oxygen concentration, the delay times for BLX8 are significantly reduced. However, for 1% and 5% oxygen cases, the slopes are nearly the same for all BLX-series propellants. This implies that at a higher energy flux, the absorption of the incident radiative energy by decomposed gaseous products from the GAP binder may become significant enough to accelerate reactions between the product gases and the oxygen in the ambient gas.

DELAY TIME FOR ONSET OF LIGHT EMISSION

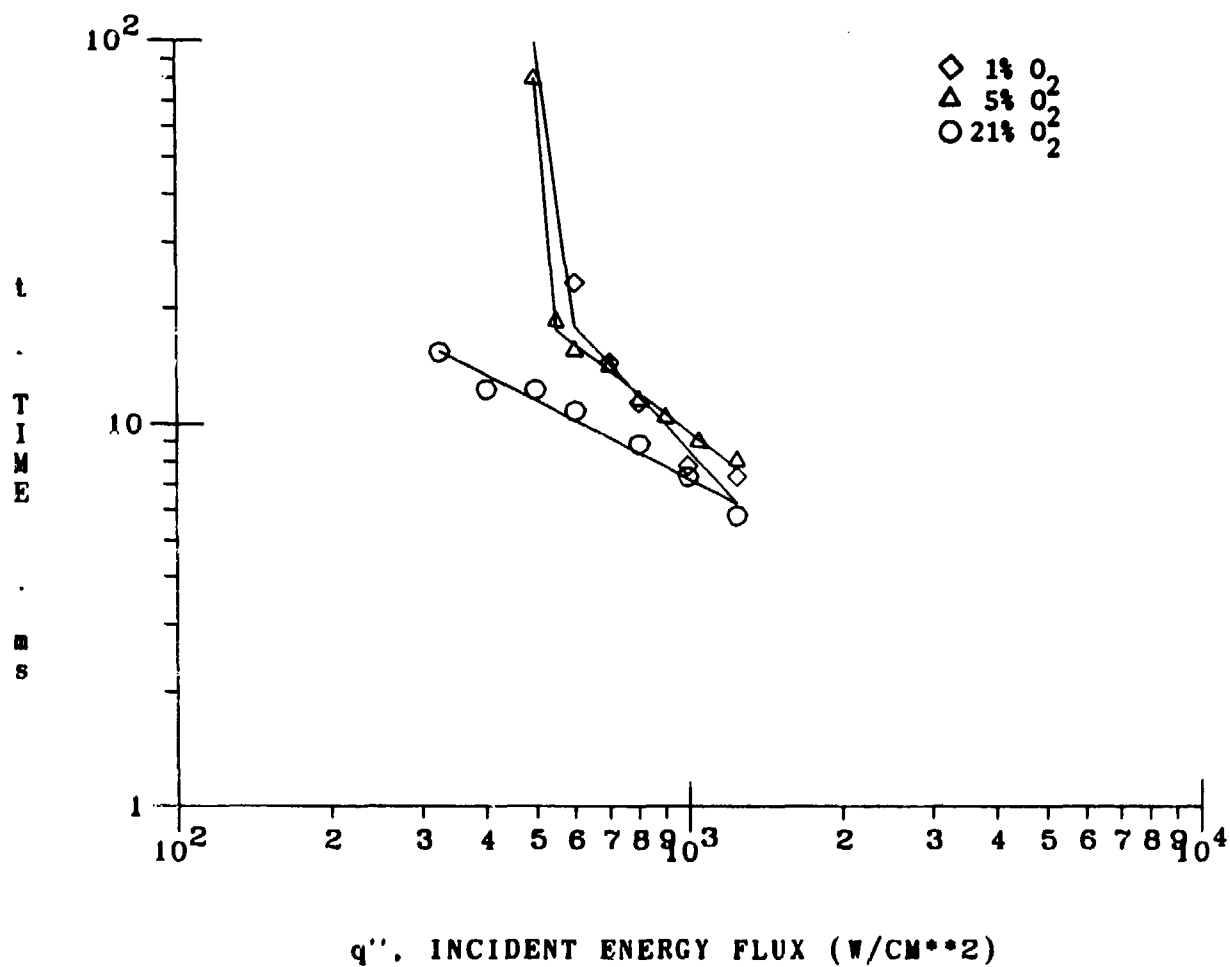


Fig. 13. Delay Time for Onset of Light Emission (BLX4)

DELAY TIME FOR ONSET OF LIGHT EMISSION (BLX8)

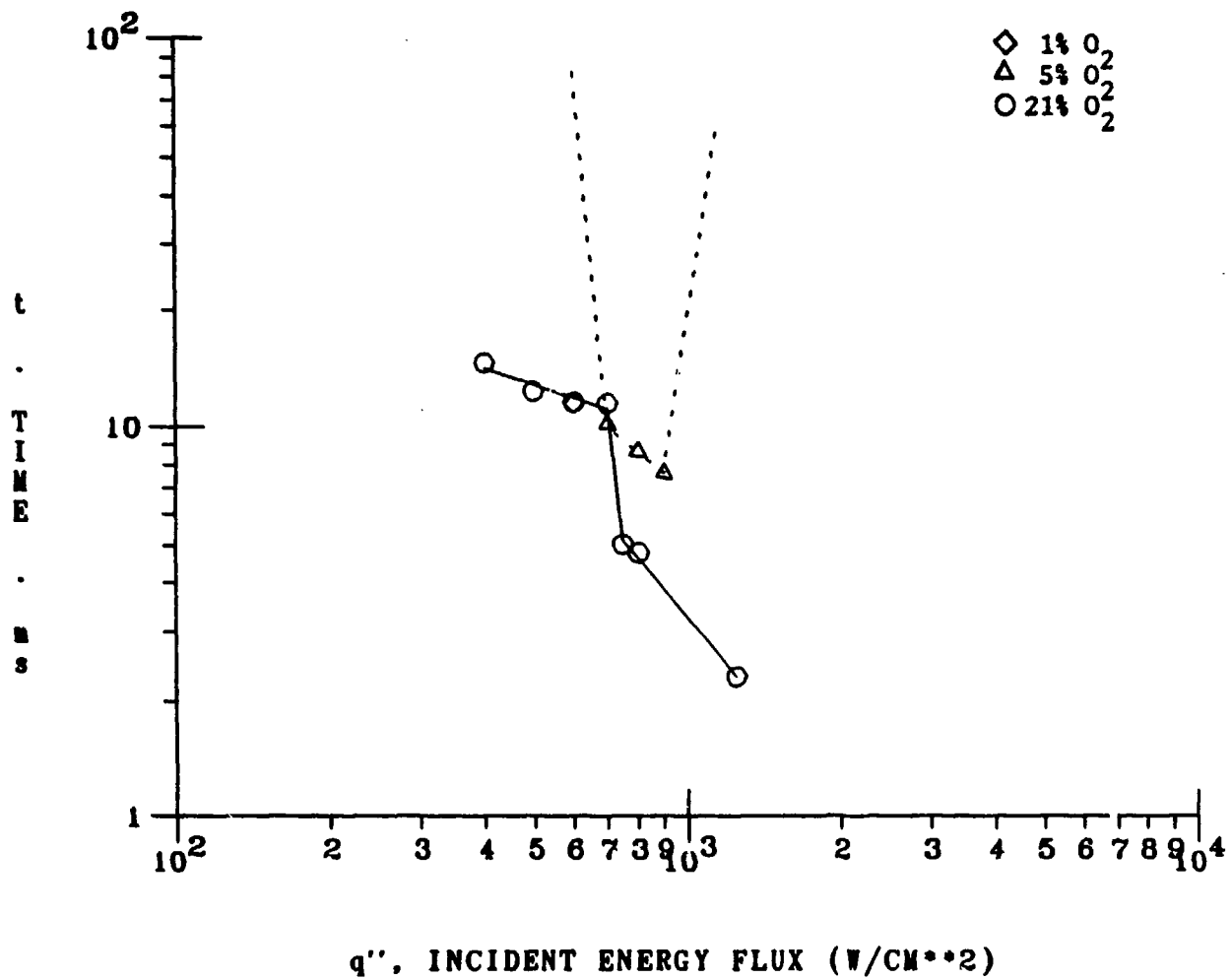


Fig. 14. Delay Time for Onset of Light Emission (BLX8)

DELAY TIME FOR ONSET OF LIGHT EMISSION

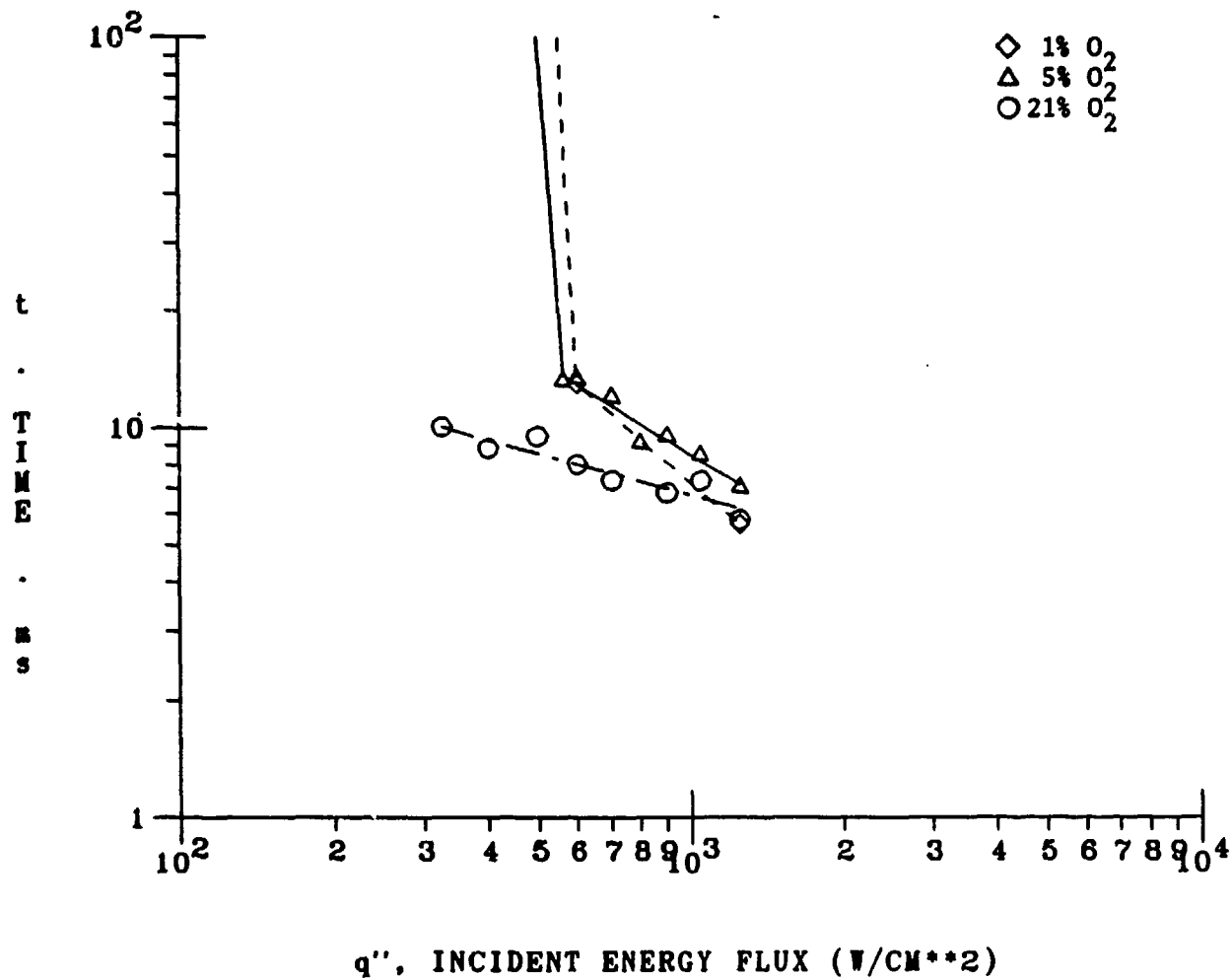


Fig. 15. Delay Time for Onset of Light Emission (BLX9)

DELAY TIME FOR ONSET OF LIGHT EMISSION (AP/HTPB)

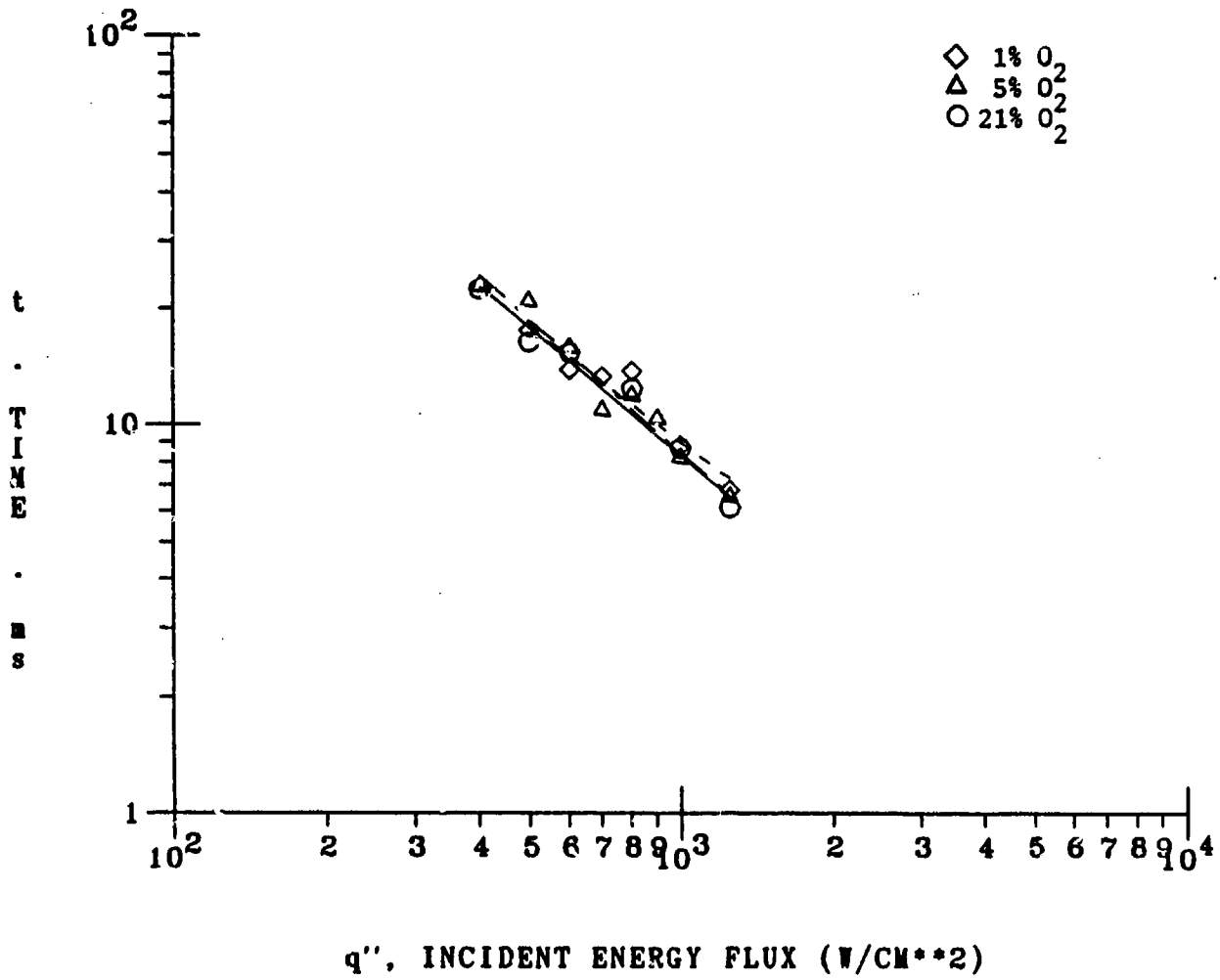


Fig. 16. Delay Time for Onset of Light Emission (AP/HTPB)

In contrast to those of the BLX-series propellants, the ignition characteristics of AP/HTPB composite propellant are nearly independent of the oxygen concentration in the ambient gas(Fig.16). This is due to the existence of sufficient oxidizer in the decomposed gaseous products.

Figure 17 presents a more detailed description of the ignition characteristics of BLX8 propellant at 5% O_2 . For energy fluxes ranging from 600 to 1000 W/cm^2 , two different luminous flames appear at different times. For example, at the incident heat flux of 800 W/cm^2 (after a period of inert heating), a luminous flame appears briefly, followed by a dark period before luminous flamelets appear on the sample surface. At lower energy fluxes (below 600 W/cm^2), no luminous flame distant from the sample surface was observed. After a relatively long exposure to the laser beam, luminous flamelets appear on the sample surface. Figure 18 presents a series of pictures recorded on the Spin-Physics video camera at an energy flux of 700 W/cm^2 . These photographs demonstrate the existence of the various zones depicted in Fig. 17. The sample location, after the appearance of luminous flamelets on the sample surface, is indicated by two reticle lines in the last picture of the series. The slope discontinuity of the curve in Fig. 17 at the critical energy flux (ca. 600 W/cm^2) is believed to be caused by the change of reaction mechanism from gas-phase to heterogeneous.

2.4.1.2 Flame Observation

Different sites and shapes of flames were observed, depending on incident energy flux, oxygen concentration in the ambient gas, and composition of the samples. Figure 19 shows the high-speed video pictures of luminous flame initiation and development for a BLX4 sample in a low oxygen concentration. A spherical flame which appears distant from the sample surface expands to become a peanut-shaped

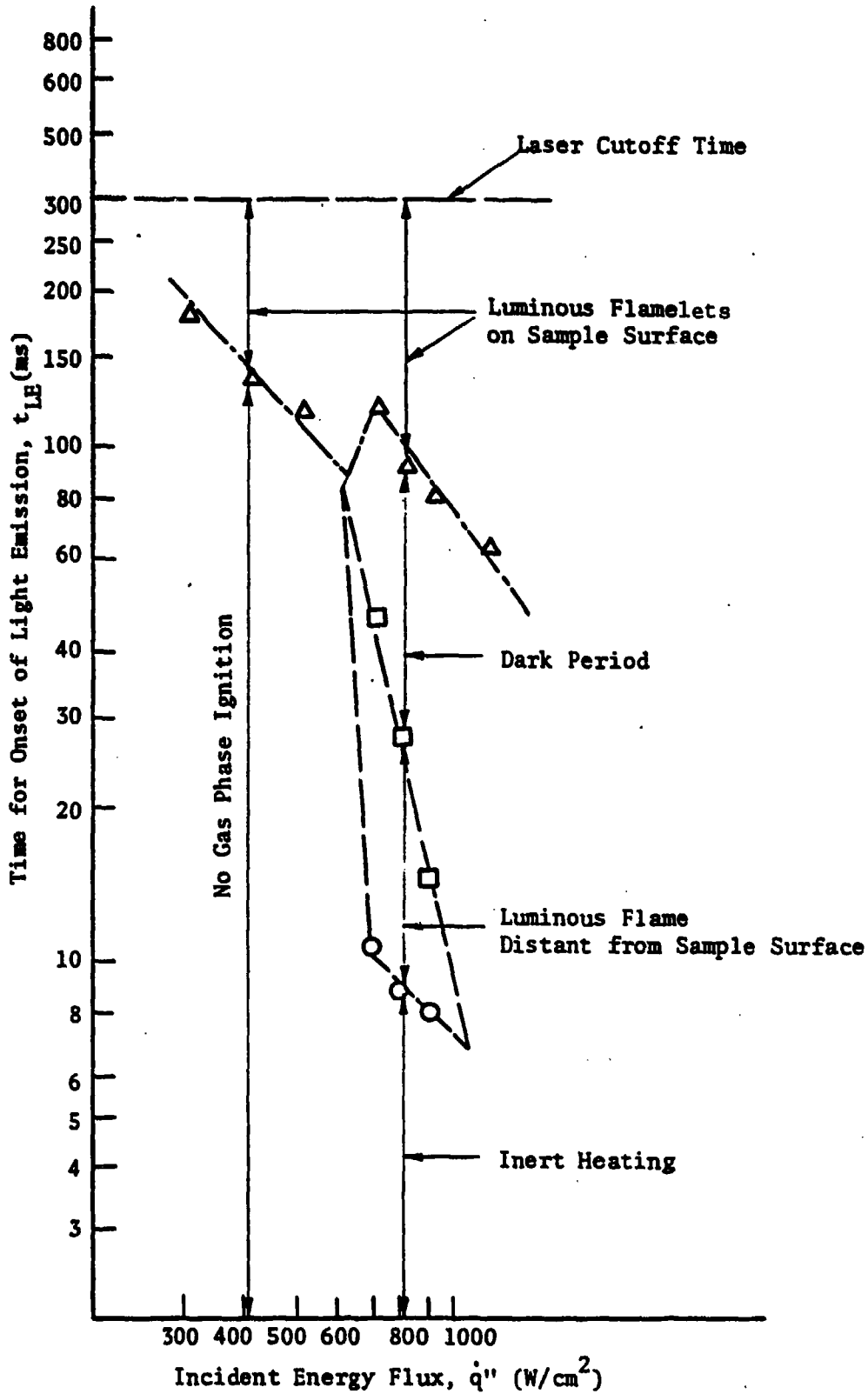


Fig. 17 Ignition Characteristics of BLX8(5% O_2 ,1atm)

flame before developing into a candle-light type flame. In contrast to this flame development, in a higher oxygen environment a dome-shaped luminous flame is established close to sample surface. Figure 20 shows the dome-shaped flame with two growing flames near the base of the dome, which may be due to the existence of the thermocouple wire. The thermocouple wire acts as a flame holder. After the thermocouple is blown away from the flame, a clear dome-shaped flame is seen (see picture in Fig. 20 at $t = 35$ ms).

During flame development, various shaped flames initiated from different sites were observed, depending on incident energy flux, oxygen concentration in the ambient gas, and composition of samples. The high-speed video pictures of ignition of the BLX4 propellant sample (see Fig. 19) show that at the onset of light emission, the luminous flame zone appears at a location distant from the sample surface. The flame expands into a larger flame, and the lower boundary of the gaseous flame moves slowly toward the sample surface. Shortly after the appearance of the gaseous flame, the luminosity of the sample surface increases with time; this indicates that heterogeneous reactions occur on the propellant sample surface while the products of this surface reaction further react in the gas phase. This is drastically different from the flame development process of BLX8 propellant. The most interesting observation to be made from these photographs is the presence of localized bright spots near the outer boundary of the gas-phase flame zone (see Fig. 19 at time = 43.5, 74.5, 75.0-80.0, 82.5 ms). These bright spots are believed to be due to the entrainment of small RDX particles by the pyrolyzed gaseous species from the energetic plasticizer. Since BLX4 propellant contains a high percentage of $4 \mu m$ RDX particles, these particles can be entrained easily by the pyrolyzed gases at the sample surface. The temperatures of the entrained particles in the dark zone are

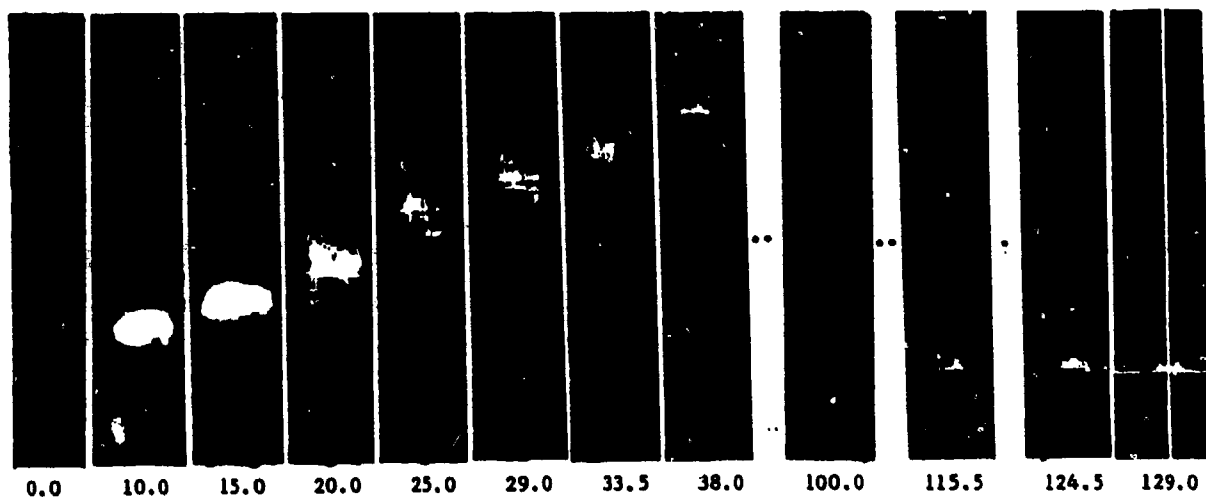


Fig. 18 Flame Development of BLX8 ($\dot{q}'' = 700W/cm^2, 5\%O_2$)

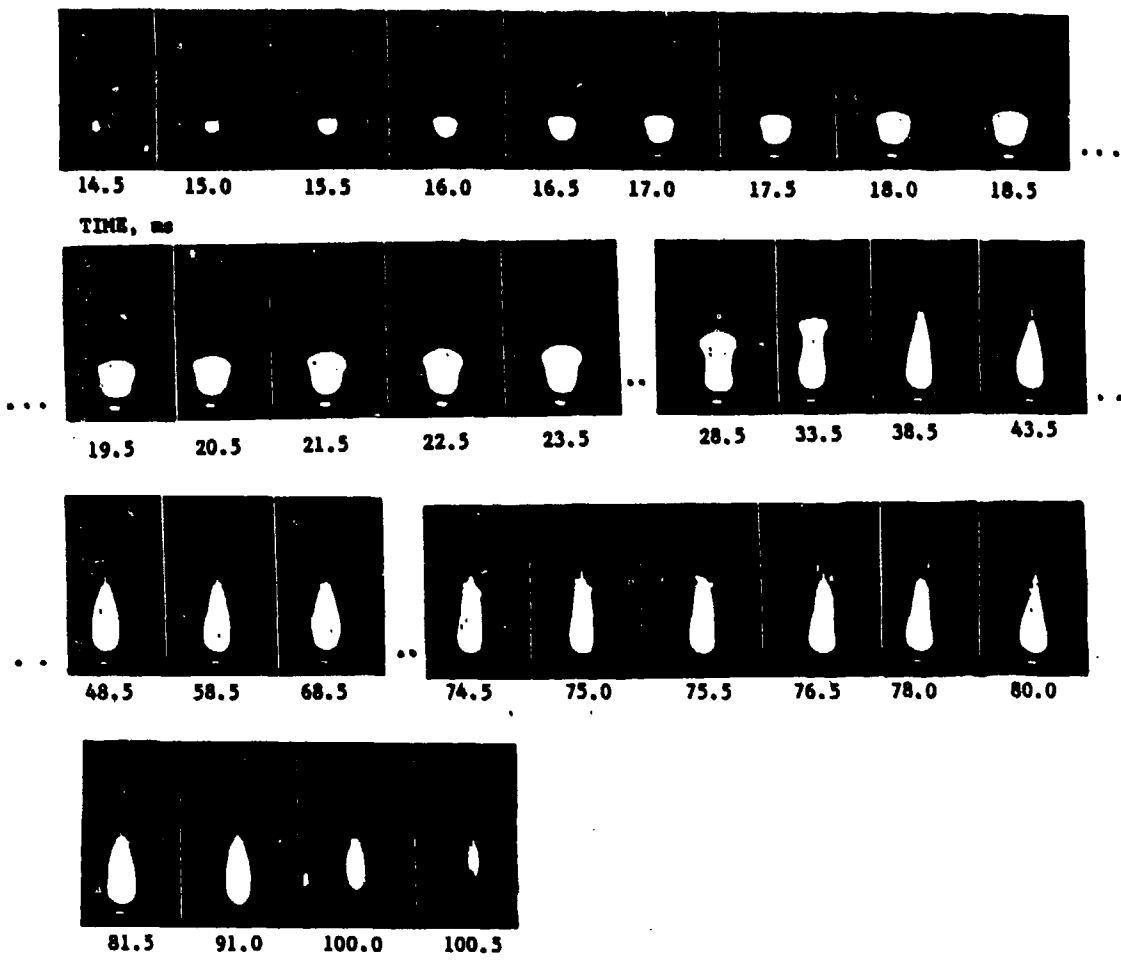


Fig. 19 Flame Development of BLX4 ($\dot{q}'' = 700W/cm^2, 1\%O_2$)

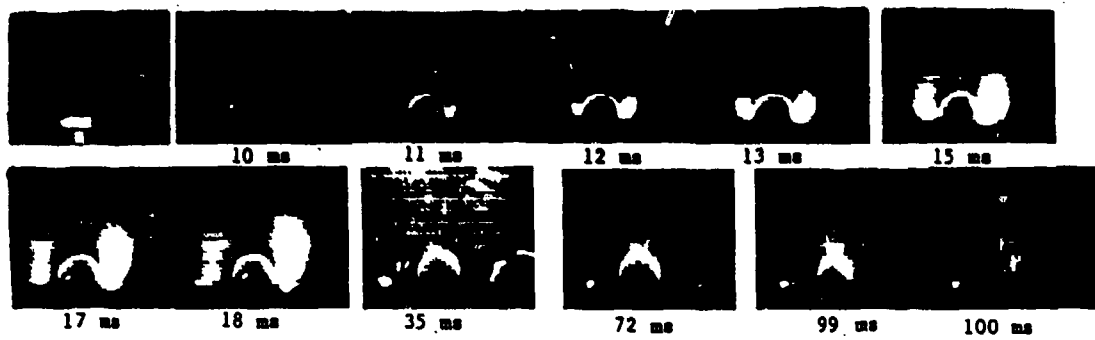
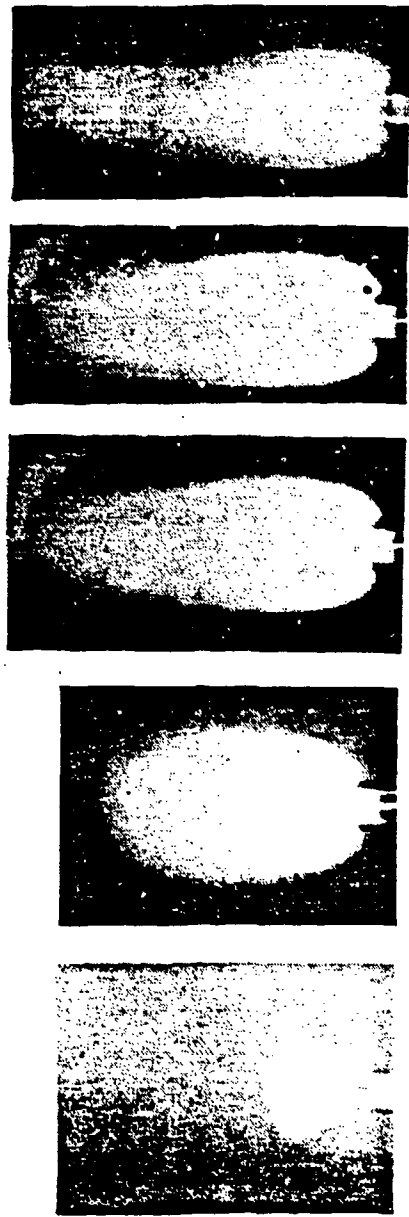


Fig. 20 Flame Development of BLX4 ($\dot{q}'' = 700W/cm^2, 21\%O_2$)

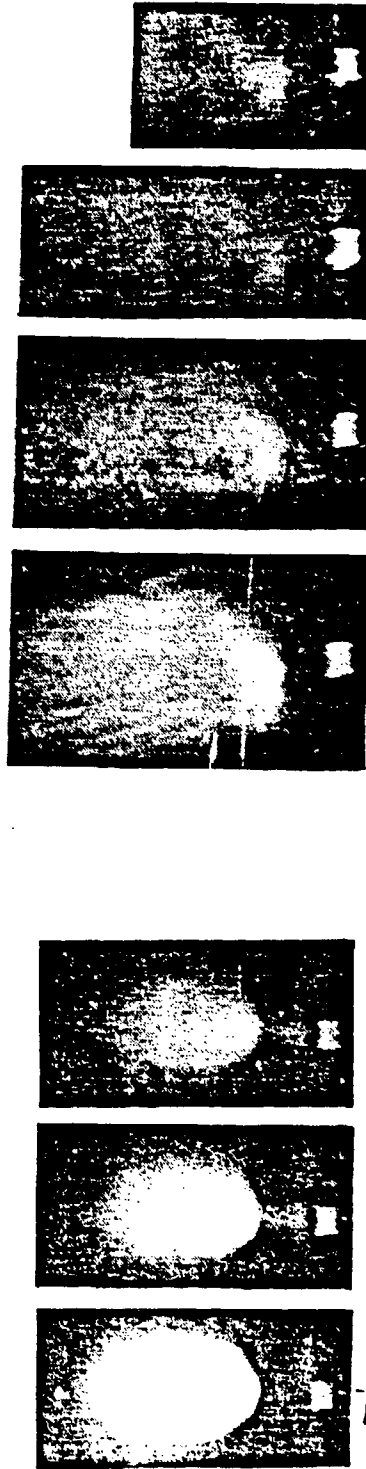
too low to produce visible bright traces. After the particles have traveled a sufficient distance in the gaseous flame, they are heated to an ignition condition and burn with a bright flame. This phenomenon is not observed with BLX8 propellant, because BLX8 contains no energetic plasticizer and because the GAP binder serves to bond the small RDX particles together. Since BLX9 has a formulation much like that of BLX4 (except for plasticizer type), the flame initiation and development of the two propellants are generally similar.

Figure 21 presents pictures of the flame development of BLX4, BLX9, and BLX8 propellant samples recorded on a conventional video camera. For all cases, the oxygen concentration in the ambient gas is 5%. Since the filming rate of the conventional video is about 25 pictures per second, detailed variations of flame development could not be captured. However, this recording does give a broader field of view of flame development in color. For the BLX4 propellant sample, the luminous flame is initiated distant from the sample surface and expands to reach very near the sample surface. This phenomenon differs from the 1% O_2 case given in Fig. 19. For the BLX9 propellant sample, the flame is distant from the sample surface until the laser is cut off; at this point the flame disappears. For the BLX8 propellant sample, a faint flame is established distant from the sample surface and the luminosity of the flame is reduced continuously. Figure 21c clearly shows that as the gas-phase flame weakens, small flamelets appear on the sample surface.

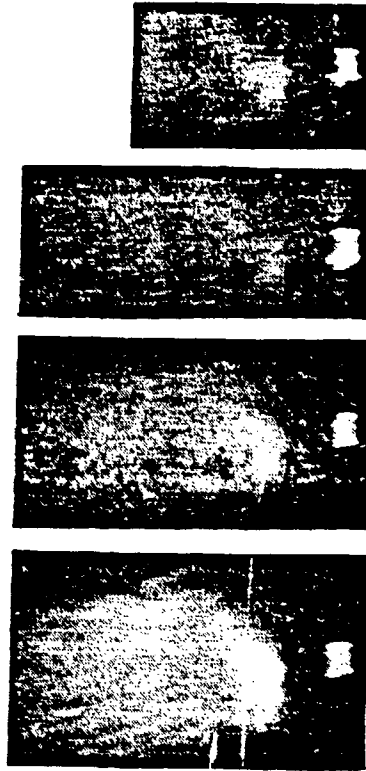
From the direct pictures recorded by the high-speed video camera, only the luminous flames were observed. However, observations of the initial gasification and movement of the decomposed gases are very important in understanding the ignition processes. Using a schlieren technique, the delay times for the gas evolution and the structures of the primary flame are determined. Figures 22 show the sequences



a) BLX4 ($\dot{q}'' = 600 \text{ W/cm}^2$, $t_{\text{EXP}} = 100 \text{ ms}$, 5% O_2)



b) BLX9 ($\dot{q}'' = 600 \text{ W/cm}^2$, $t_{\text{EXP}} = 150 \text{ ms}$, 5% O_2)



c) BLX8 ($\dot{q}'' = 700 \text{ W/cm}^2$, $t_{\text{EXP}} = 200 \text{ ms}$, 5% O_2)

Fig. 21 Flame Structure Recorded by Conventional Video Camera

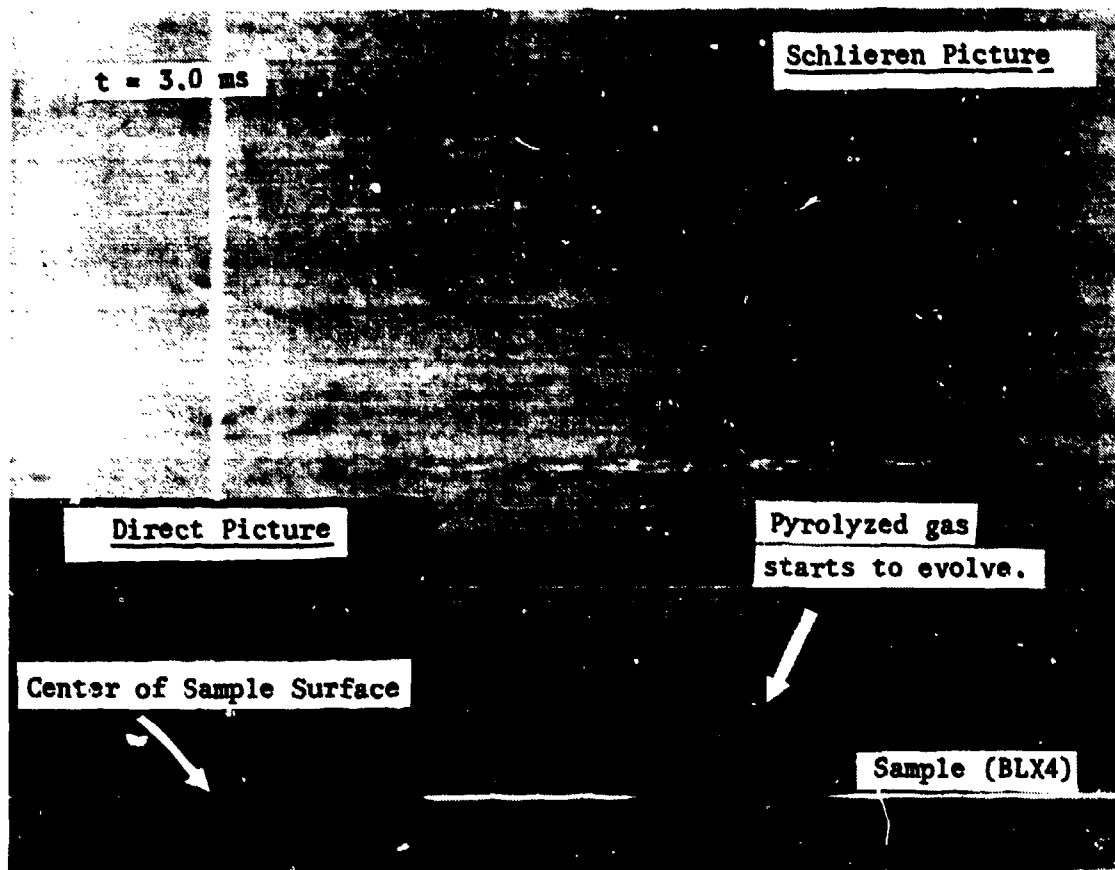


Fig. 22a Schlieren Pictures and Direct Pictures

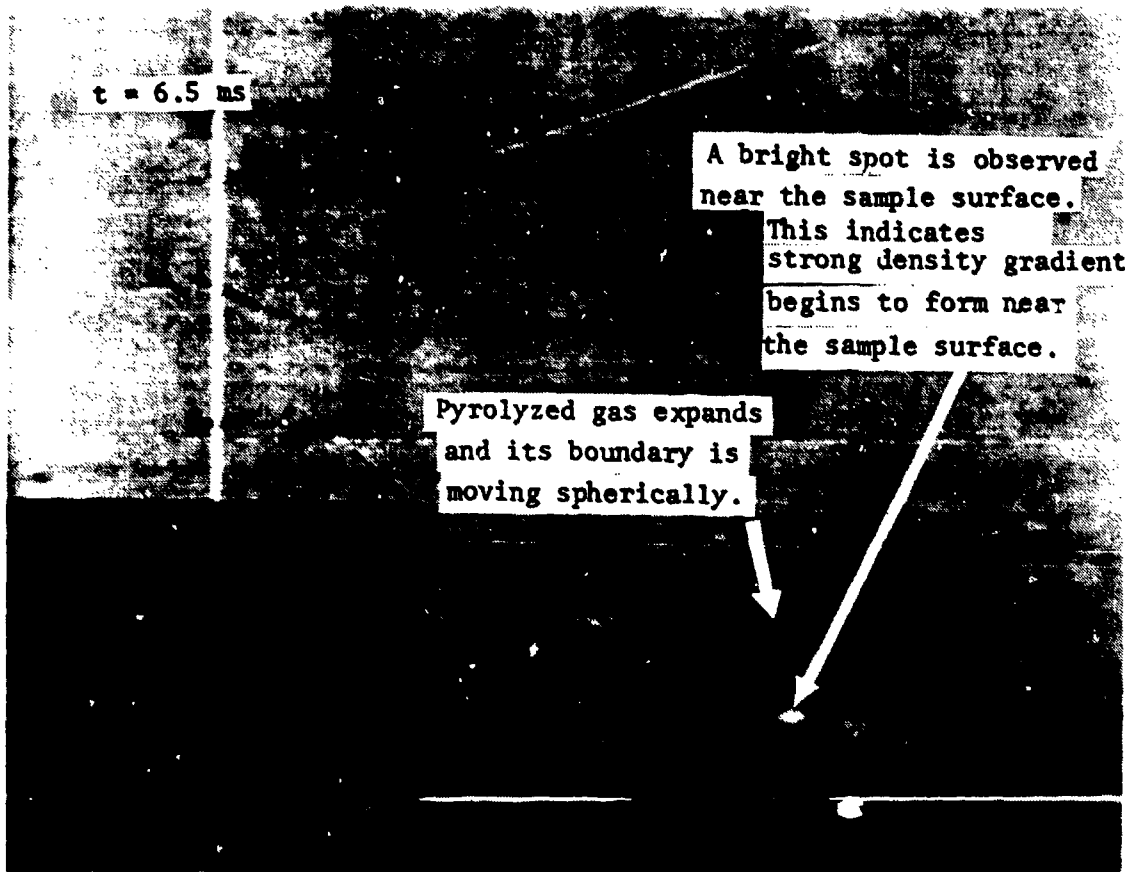


Fig. 22b Schlieren Pictures and Direct Pictures

$t = 10 \text{ ns}$

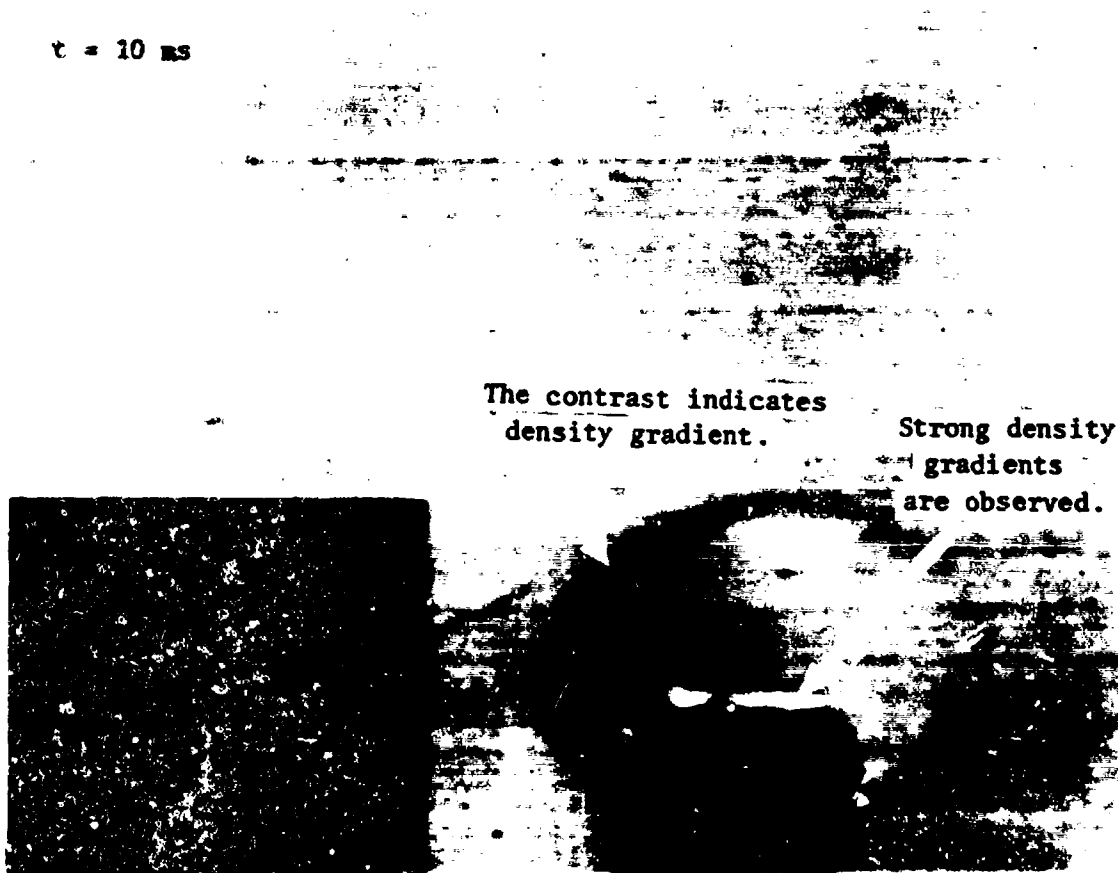
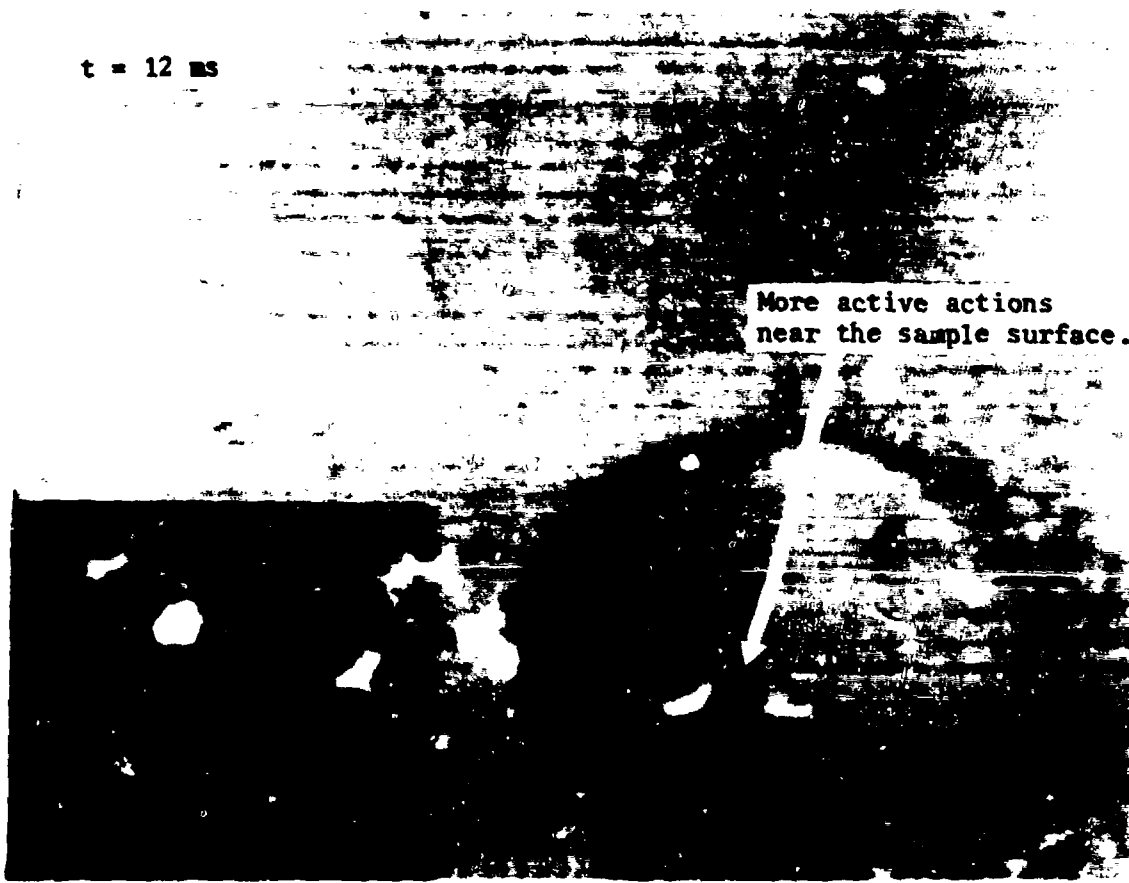


Fig. 22c Schlieren Pictures and Direct Pictures



t = 12 ms

More active actions
near the sample surface.

Fig. 22d Schlieren Pictures and Direct Pictures





Fig. 22e Schlieren Pictures and Direct Pictures

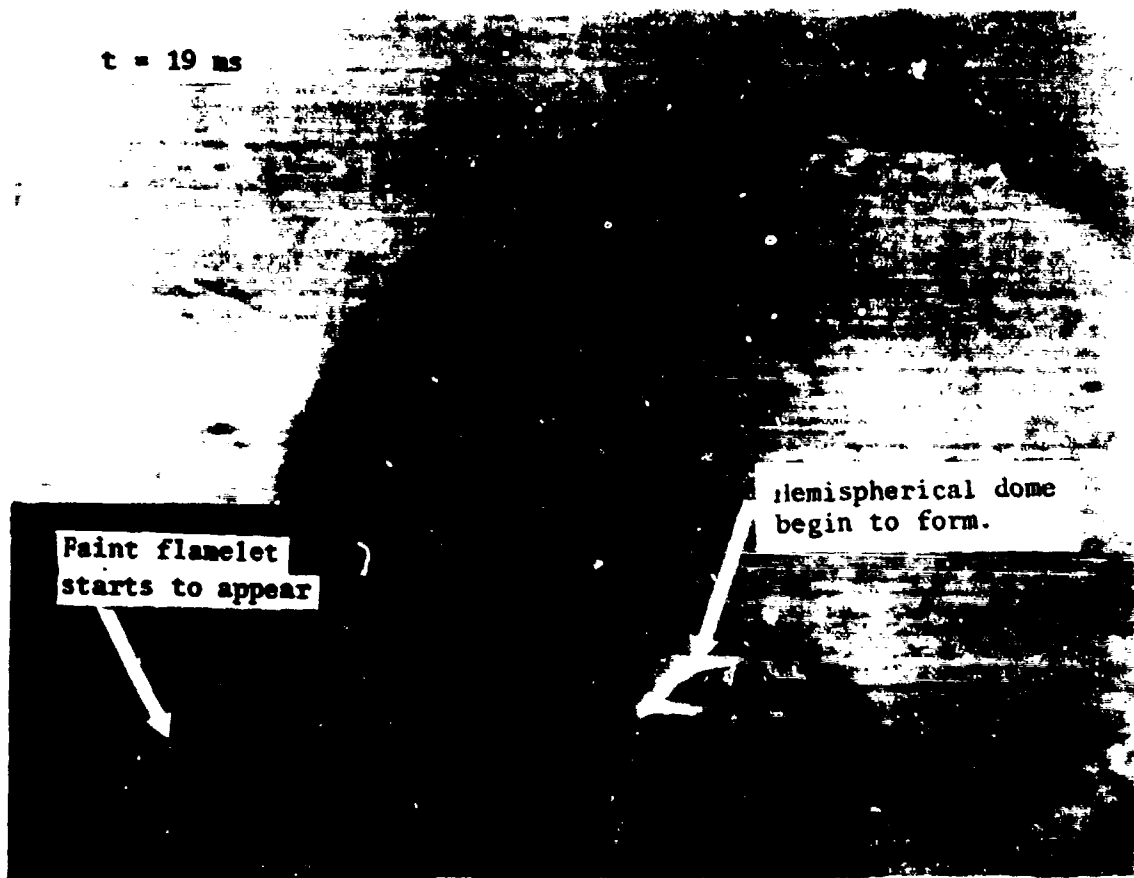


Fig. 22f Schlieren Pictures and Direct Pictures

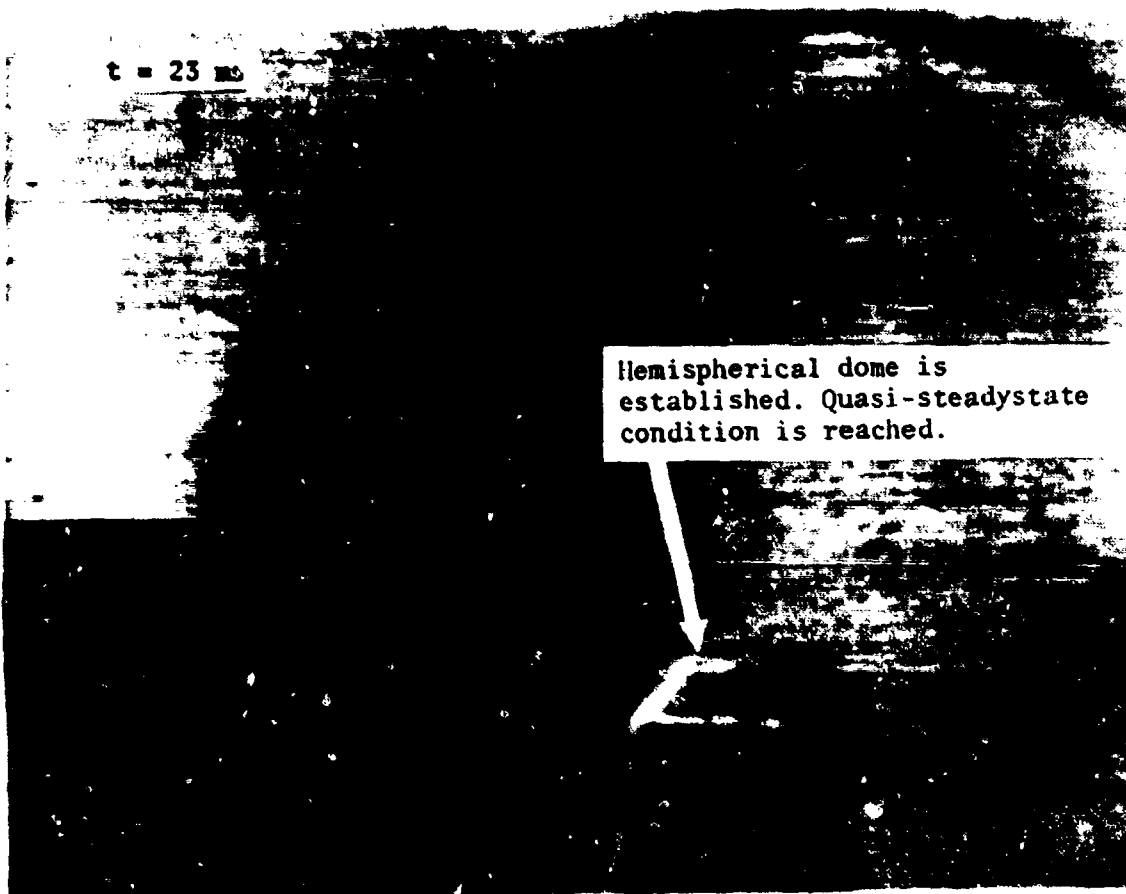


Fig. 22g Schlieren Pictures and Direct Pictures

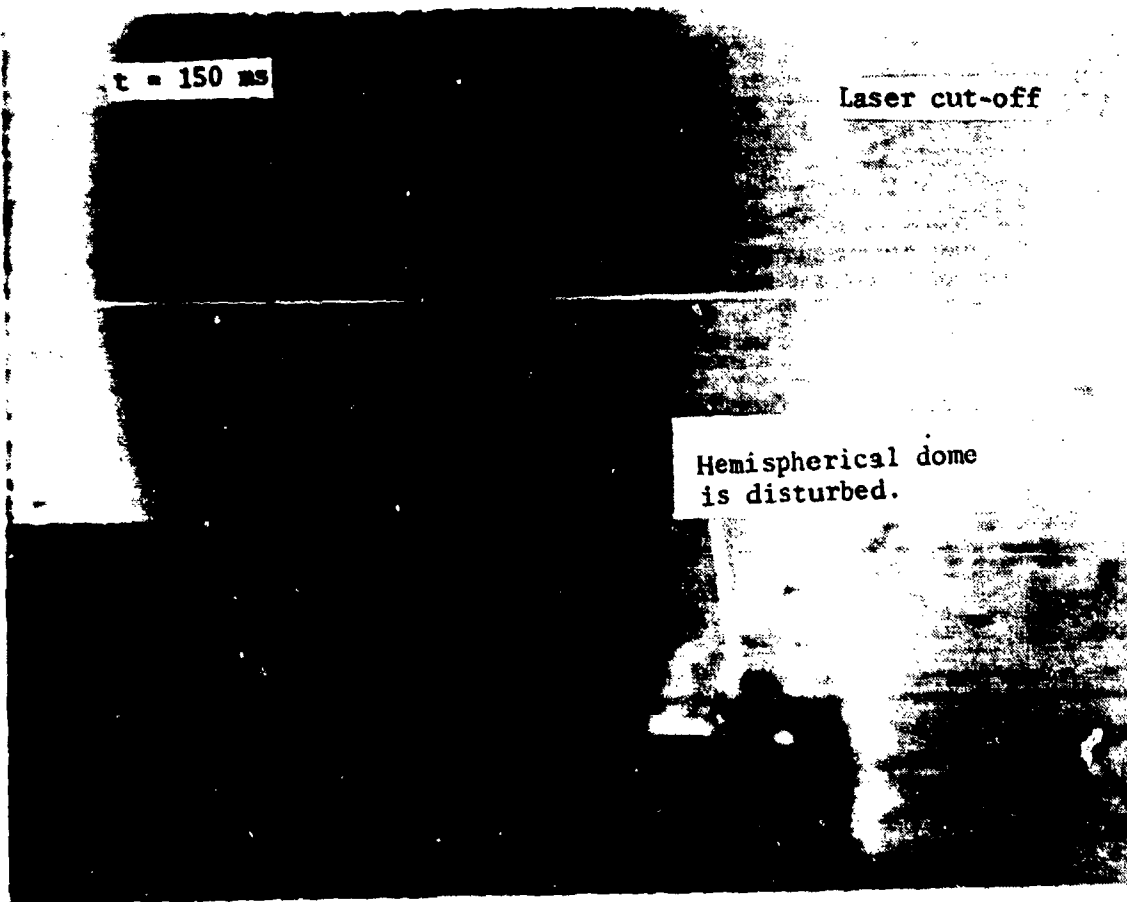


Fig. 22h Schlieren Pictures and Direct Pictures

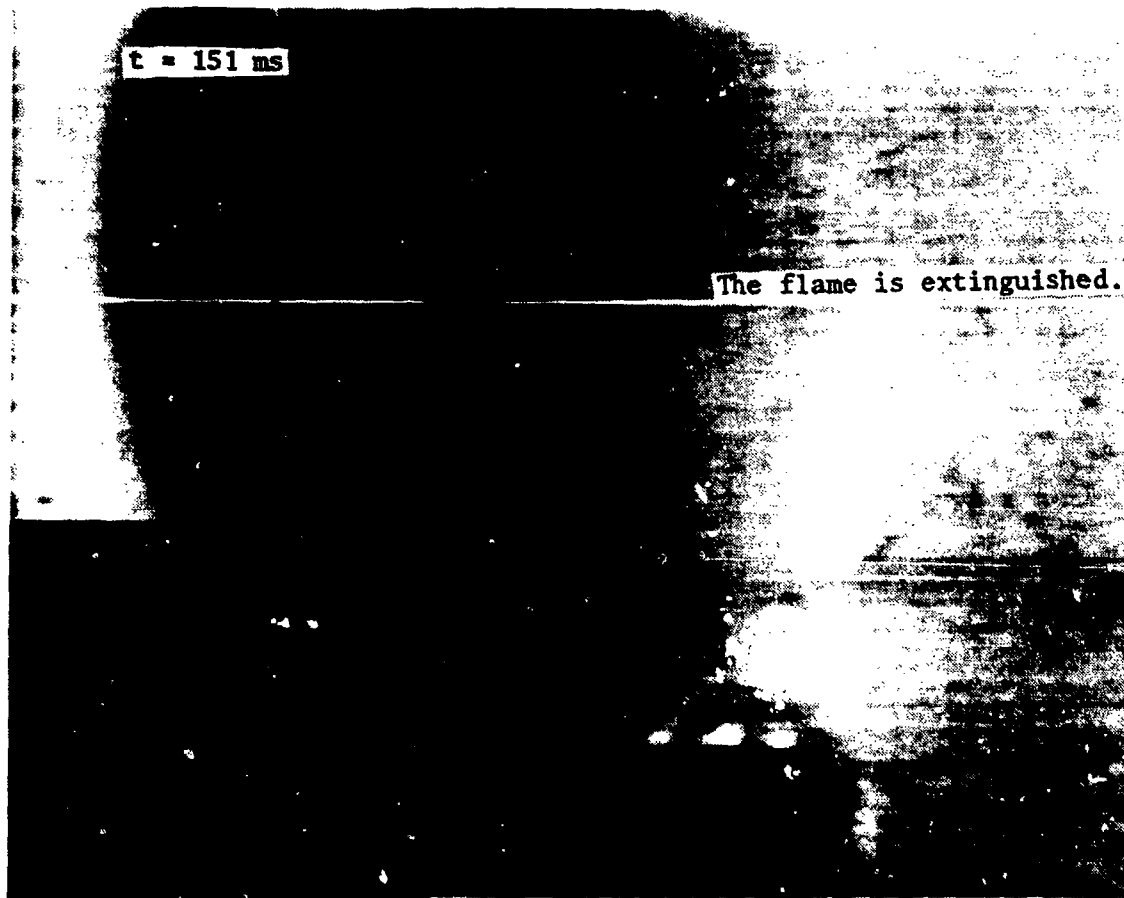


Fig. 22i Schlieren Pictures and Direct Pictures

of gasification and the movement of decomposed gases recorded on the high-speed video camera.

2.4.1.3 Thermal Wave Structure

The surface temperatures and temperature profiles in the gas phase were measured using the fine wire thermocouples described in the previous chapter. Figure 23 shows the surface temperature of BLX4 in an inert gas during radiative heating at 1000 W/cm^2 . After an initial transient, the surface temperature reached a constant temperature of about 480°C . When the laser is cut off, the surface temperature decreased abruptly.

Temperatures in the gas phase were measured while the surface of the propellant sample recessed during laser heating. The relative locations of the thermocouples to the propellant surface were changing with time. Figure 24 shows the gas temperature variation as the distance of the thermocouple from the surface changes from 4.7 mm to 6.5 mm. As in the surface temperature cases, after an initial transient the gas temperature reached a nearly steady value. In the variation of the distance between the thermocouple and the receding surface, the spatial distribution of the gas temperature was considered to be nearly uniform. This corresponds with the thermal wave structure in a steady-state combustion. In his study of steady-state combustion of nitramine composite propellants, Kubota[3] observed that the luminous flame stood some distance from the burning surface. He considered the non-luminous zone below the luminous flame as a preparation zone similar to the dark zone in the flame of double-base propellants. The gas temperature in the dark zone is nearly constant.

Both surface and gas temperatures were measured by means of a thermocouple. Before the energy flux is applied, the thermocouple wire is located on the surface



TEMPERATURE VS TIME (IGN4211)

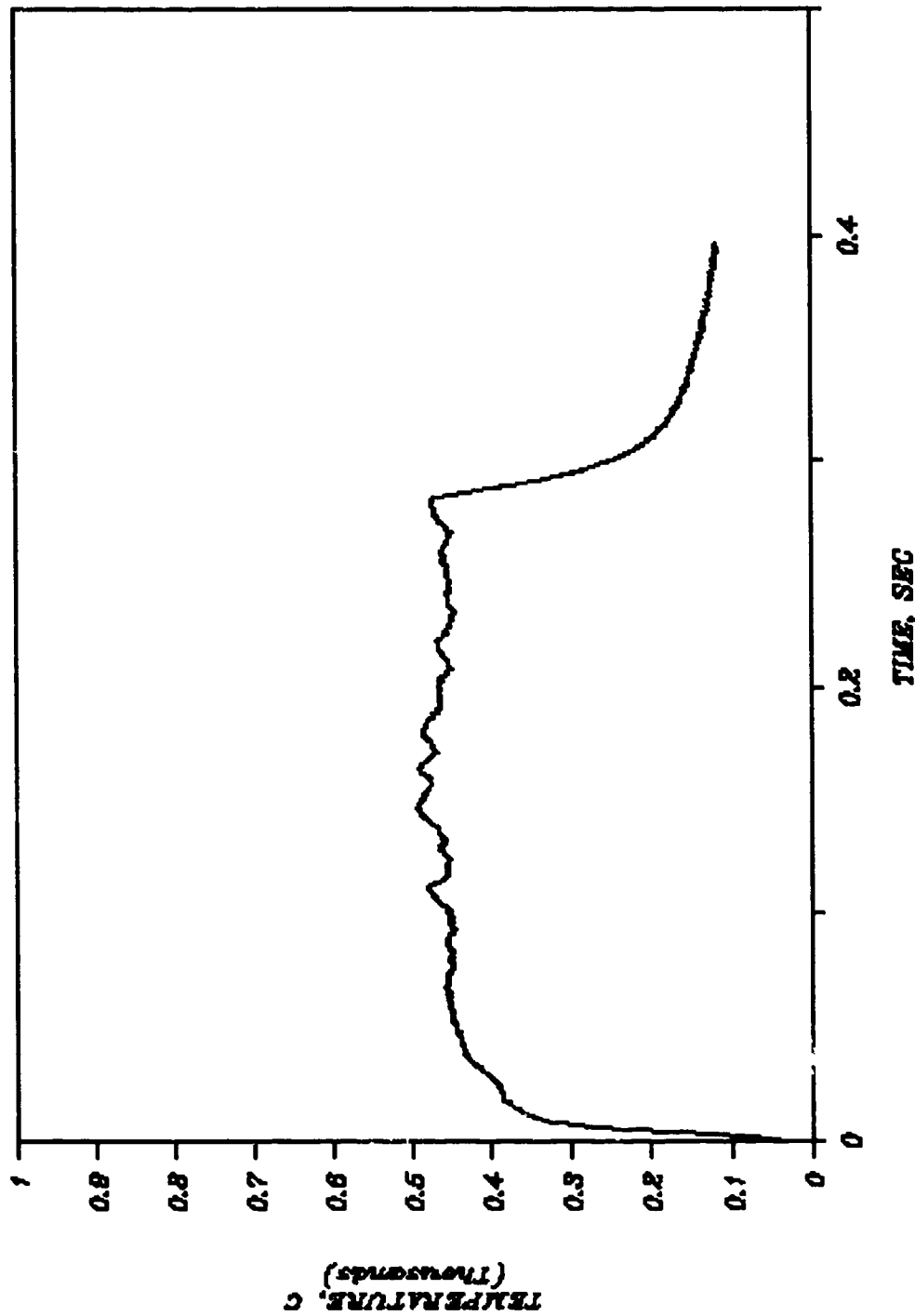


Fig. 23 Surface Temperature vs. Time ($\dot{q}'' = 1000W/cm^2, Hc$)

TEMPERATURE VS TIME (IGN4218)

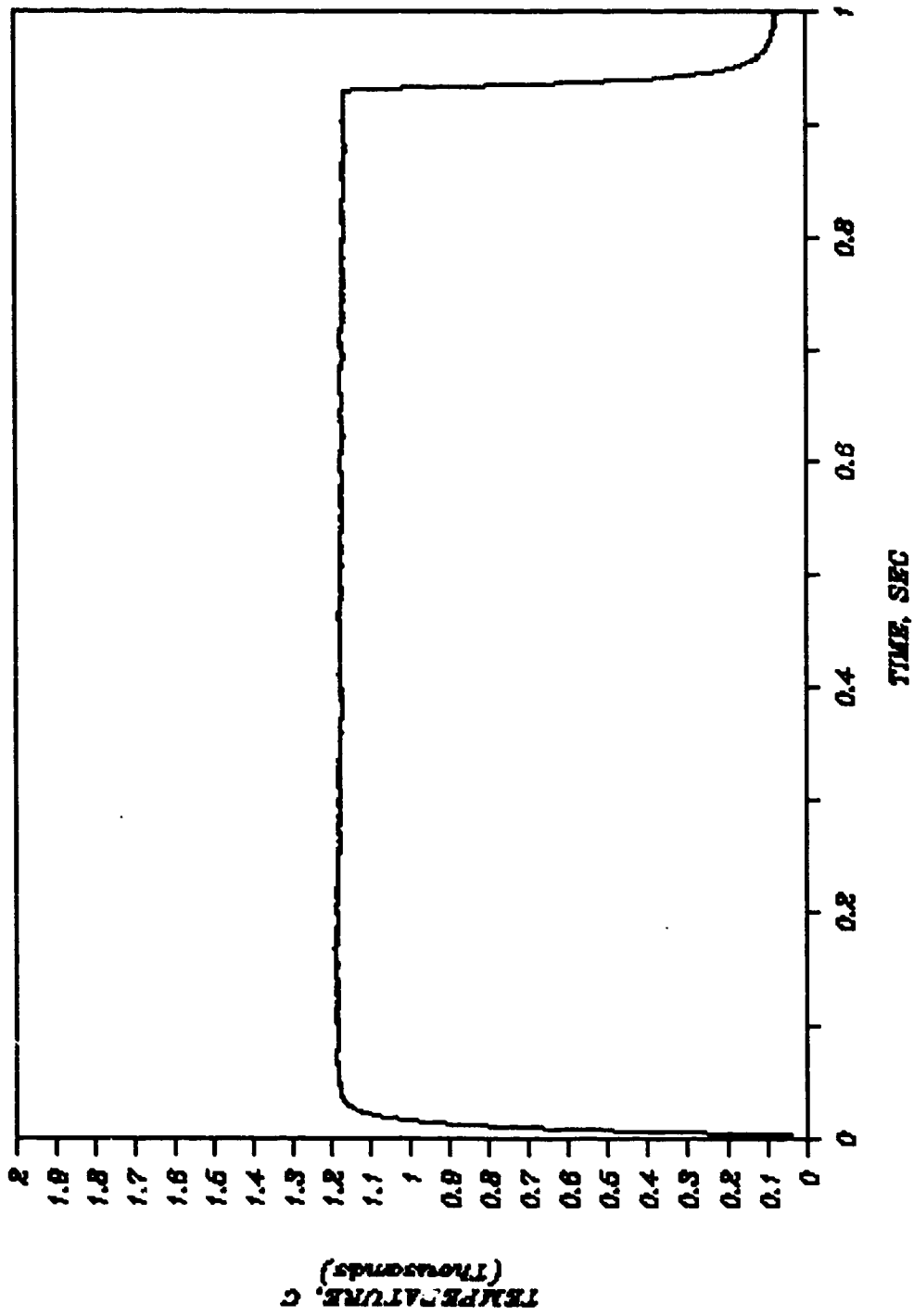


Fig. 24 Gas Temperature vs. Time ($q'' = 600 \text{ W/cm}^2, \text{ He}$)

TEMPERATURE VS TIME (IGN4322)

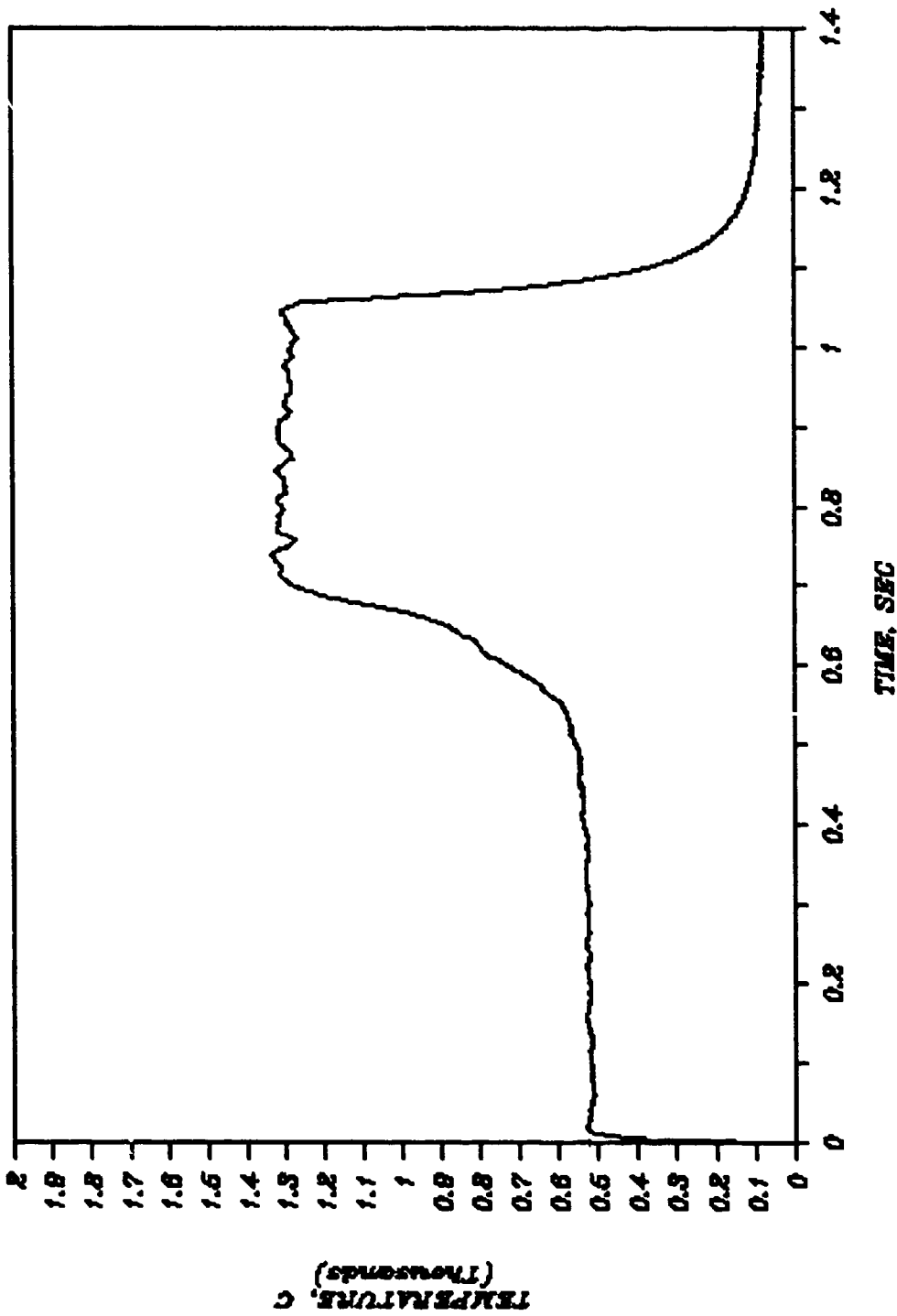


Fig. 25 Surface and Gas Temperature vs. Time ($\dot{q}'' = 1000W/cm^2$)

TEMPERATURE VS TIME (IGN4323)

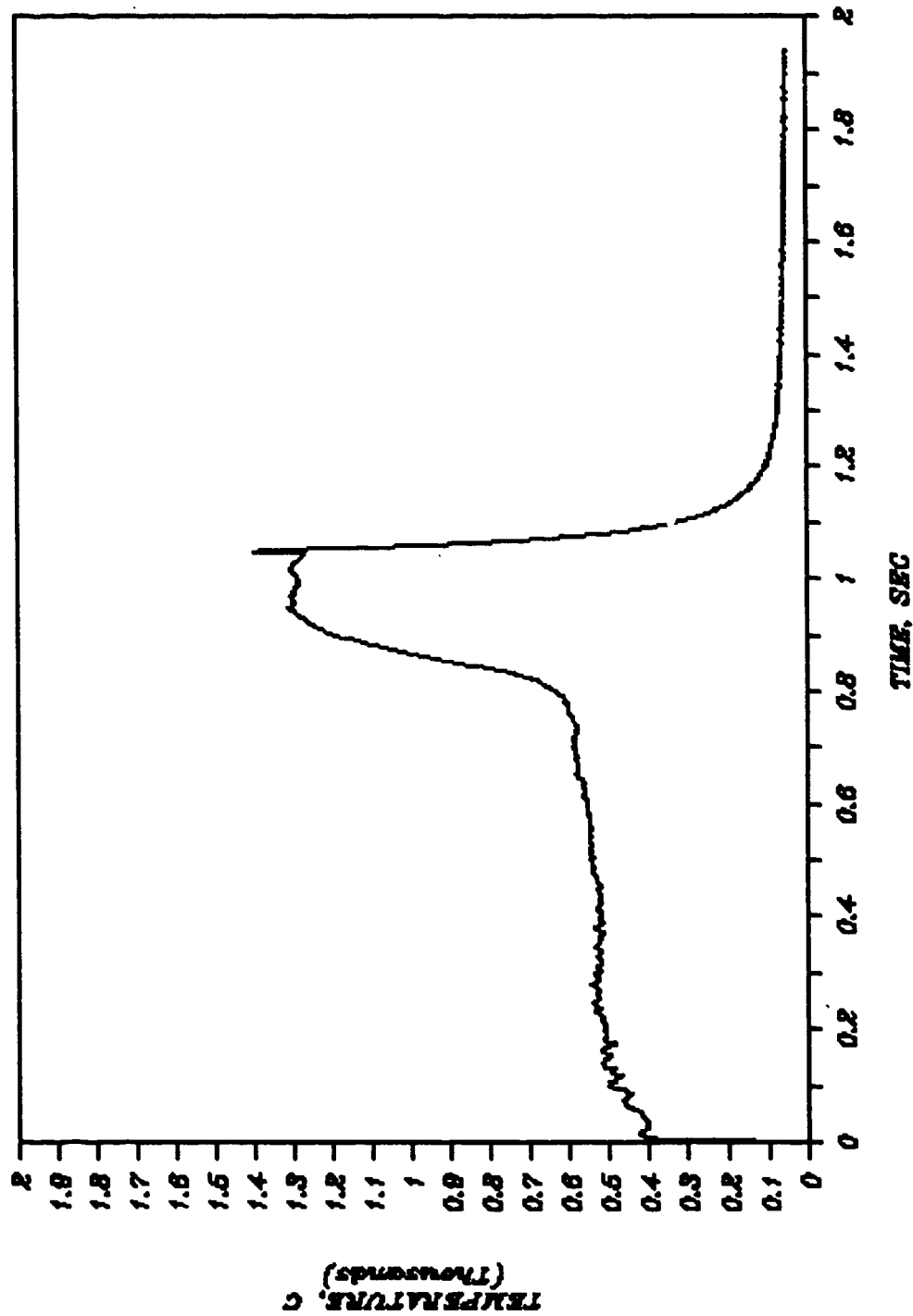


Fig. 26 Surface and Gas Temperature vs. Time ($q'' = 800W/cm^2$)

TEMPERATURE VS TIME (IGN4324)

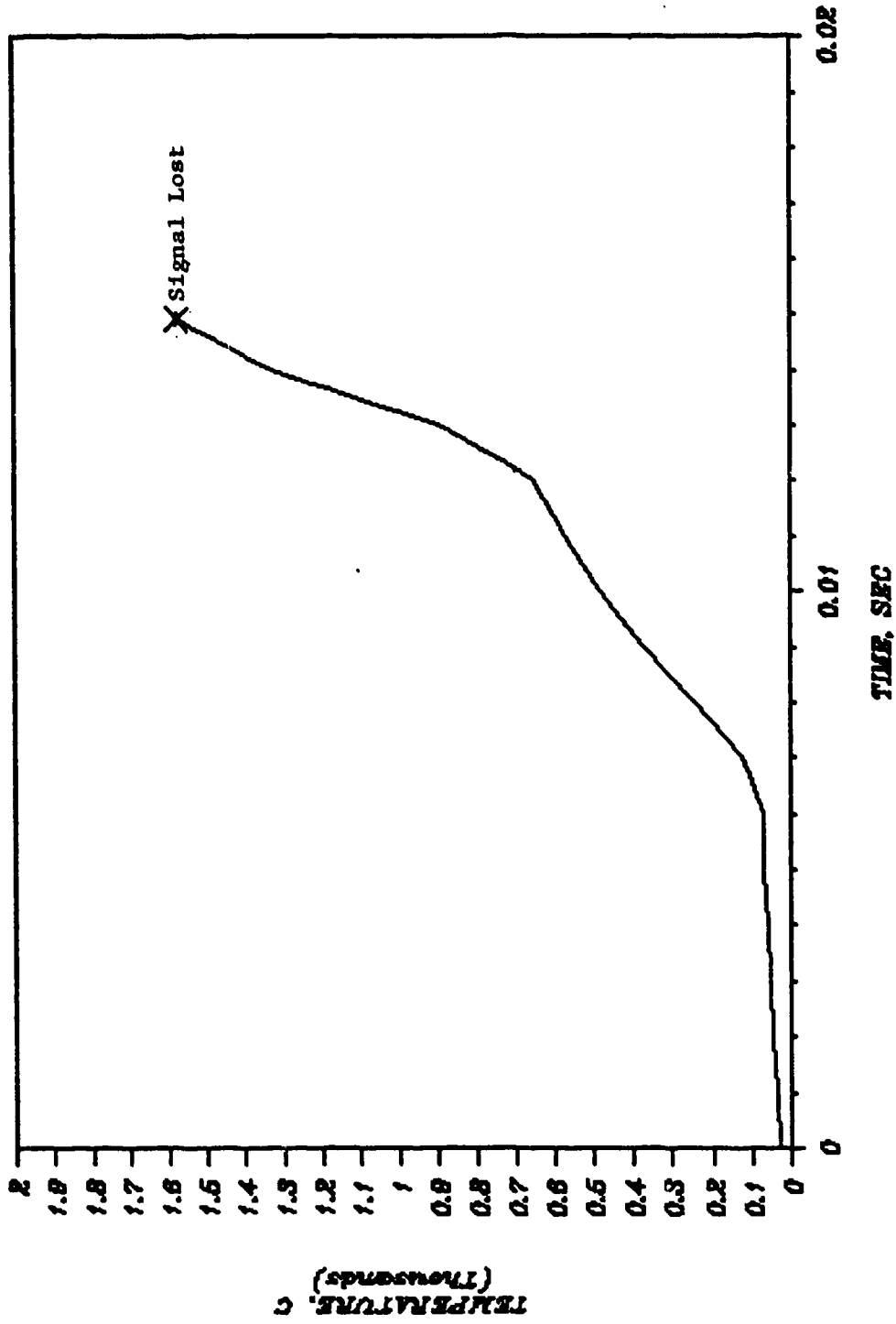


Fig. 27 Gas Temperature vs. Time ($q'' = 800W/cm^2$)

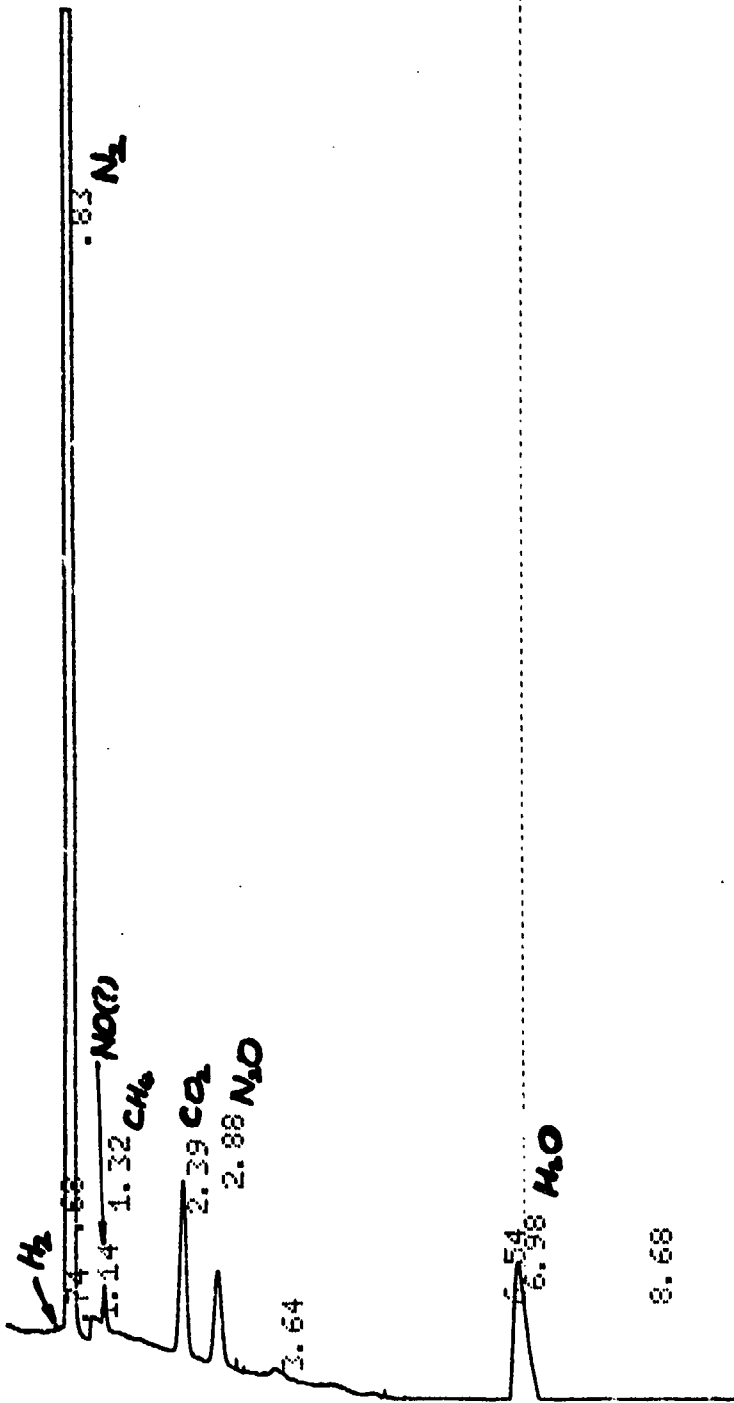
of a propellant sample. During the initial phase of radiative heating, the thermocouple measures surface temperature. As heating continues, the surface of the propellant sample recesses and the thermocouple wire leaves the surface and measures the temperature of the gas phase. The location of the thermocouple wire during the event is monitored by the schlieren pictures recorded on the Spin-Physics high-speed video camera. Figures 25 and 26 show the temperature traces for the incident energy fluxes 1000 W/cm^2 and 800 W/cm^2 , respectively. After an initial rise, the temperature reaches a constant value, about 510°C . As heating continues, the thermocouple wire leaves the propellant surface. Gas temperature near the surface increases slightly until the second temperature rise reaches the preparation-zone temperature, about 1300°C . It is interesting to note that the gas temperature near the propellant surface (about 2 or 3 mm above the surface) is nearly the same as the surface temperature. This indicates that the entire energy consumed for the surface pyrolysis comes from the incident laser energy. The contribution of conduction from the gas phase is negligible. Comparing the two temperature traces in Figs. 24 and 25, it can be seen that the surface and gas temperatures in the preparation zone are nearly the same.

Figure 27 shows the temperature trace measured by a thermocouple initially located away (12 mm) from the propellant surface. Once a luminous flame was established near the thermocouple, the temperature increased abruptly and the thermocouple wire broke. The temperature of the luminous flame was too high to be measured by the $25 \mu\text{m}$ Pt-Pt13%Rh thermocouple.

2.4.1.4 Gas Analysis

Gas samples from the pyrolysis and ignition of the nitramine composite propellants were analyzed, using gas chromatography to determine the concentrations

CHANNEL A INJECT 02/27/87 13:07:36



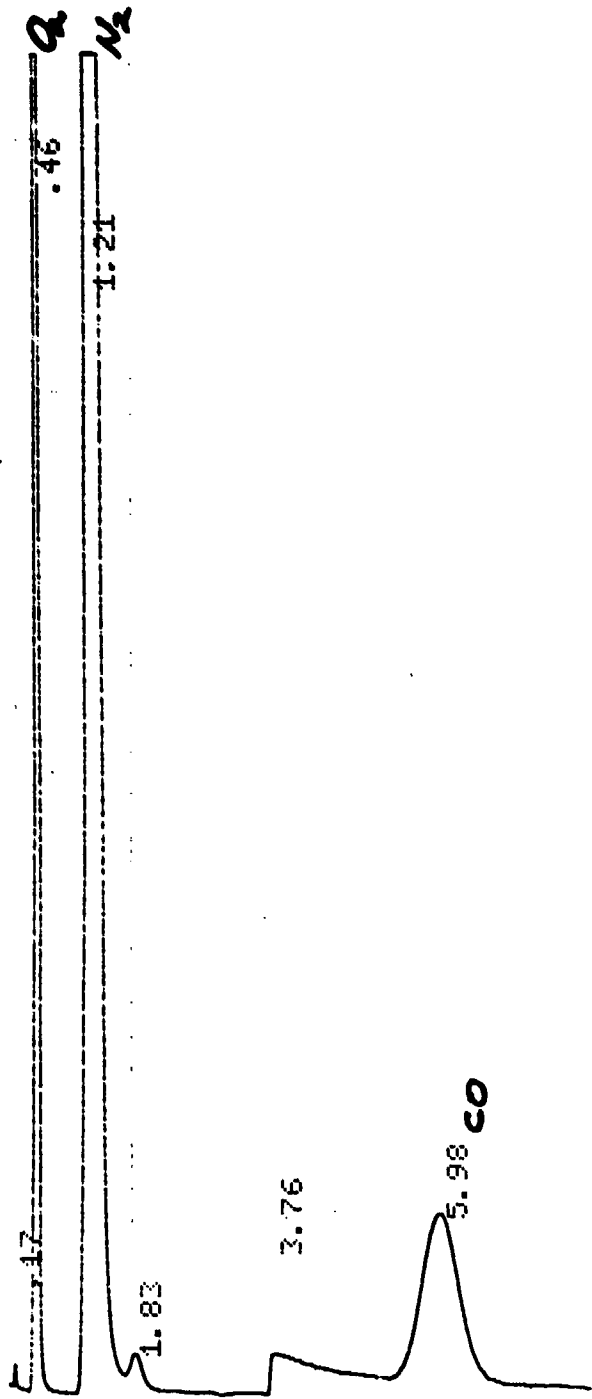
02/27/87 13:07:36 CH= "A" PS= 1.

FILE 1. METHOD 0. RUN 53 INDEX 53

PEAK#	AREA%	RT	AREA	BC
1	0.02	0.68	65	02
2	0.027	0.74	85	02
3	78.702	0.63	251581	03
4	0.293	1.14	937	02
5	0.348	1.32	1114	03
6	1.899	2.39	6072	01
7	1.174	2.88	3753	01
8	0.144	3.64	459	01
9	1.66	6.54	5305	02
10	13.12	6.98	41939	03
11	2.613	8.68	8354	01

TOTAL 100. 319664

Fig. 28 A Typical Output of Gas Chromatograph for Porapak Q and R Column



02/27/87 10:29:41 CH= "A" PS= 1.

FILE 1. METHOD 0. RUN 49 INDEX 49

PEAK#	AREA%	RT	AREA	BC
1	0.029	0.17	180	01
2	16.362	0.46	77807	01
3	75.169	1.21	357456	08
4	0.331	1.83	1575	05
5	1.358	3.76	6456	01
6	6.743	5.98	32065	01

TOTAL 100. 475539

Fig. 29 A Typical Output of Gas Chromatograph for MS 5A Column

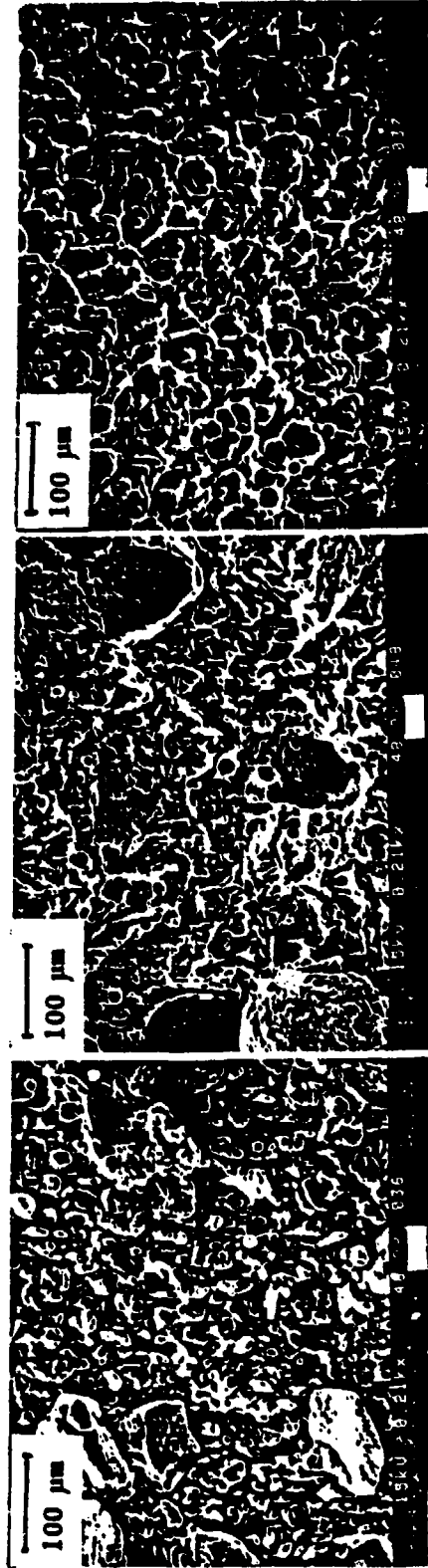
of stable species. Various sizes of syringes were used to take samples from the test chamber. Since N_2 is a product gas from the combustion of the nitramine composite propellants, He was used as a carrier gas for the gas chromatograph. Figures 28 and 29 show the typical outputs of the gas chromatograph for the test propellants. A Porapak Q in series with a Porapak R column was used to detect such stable species as H_2 , N_2 , CH_4 , N_2O , NO , and CO_2 . A molecular sieve (MS 5A) was used to detect O_3 , N_2 , and CO . Many of the peaks appearing on the outputs were identified through calibrations with standard gases and cross examination with results of a GC/MS. However, not all of the peaks that appeared on the figures were identified.

The relative amounts of the gaseous species in the product gases were obtained. The weight percentages of the gaseous species were estimated by normalizing the weight of the species by the total weight of the propellant sample consumed during the event. As the incident energy increased, the amounts of such stable species as H_2 , CO_2 , and CO increased. At a low pressure (ca. 10^{-3} atm), the amounts of the stable species decreased significantly. Additional tests with the gas analysis are necessary to understand the chemical reaction mechanisms involved in the pyrolysis and ignition of nitramine composite propellants.

2.4.1.5 Sample Surface Structure

Micrographs of the original and recovered BLX4 propellant samples are shown in Fig. 30. After a short exposure to laser radiation (before attaining light emission), large and small holes were found on the sample surface (see Fig. 30b). On the other hand, surfaces of recovered samples after onset of light emission do not exhibit large holes. Instead, they show more evenly distributed small holes surrounded by solidified binder melt (see Fig. 30c). By comparing the micrograph, one can conclude that during the initial phase of laser heating, materials between RDX particles and

fuel binder pyrolyze and react to create pressure buildup in the interface region. Local pressure buildup could be the main cause of RDX particle ejection from the surface. From this point on, the surface becomes more homogeneous.



a) Original

**b) After a Short Exposure
(Before Light Emission)**

**c) After a Longer Exposure
(After Light Emission)**

Fig. 30 Scanning Electron Micrographs of BLX4

2.5 SUMMARY AND CONCLUSIONS

Laser ignition of a series of RDX-based nitramine composite propellants has been studied theoretically and experimentally. Observations and findings available at present are summarized as follows:

- 1) A comprehensive theoretical model for radiative ignition of nitramine composite propellants was formulated. A computer code was developed to analyze the theoretical model.
- 2) A radiative ignition test setup using a high-power CO_2 laser was designed and constructed.
- 3) Ignition characteristics of a series of RDX-based composite propellants were studied experimentally, using the test setup.
- 4) Delay time for onset of light emission in the gas phase is strongly dependent on incident laser energy flux, oxygen concentration in the ambient gas, and the properties of propellant ingredients.
- 5) Propellants that contain energetic plasticizers (BLX4 and BLX9) are more strongly dependent upon ambient oxygen concentrations.
- 6) Critical energy fluxes exist for obtaining distant gas-phase flames.
- 7) Particle ejection into the gas-phase flame was observed; particle ejection is believed to be caused by local pressure buildup between RDX particles and binder material.
- 8) Micrographs of recovered samples before and after attaining light emission are quite different. Large holes on the propellant surface after tests indicate that the RDX particles leave the sample surface before the binder is pyrolyzed.
- 9) The effect of the incident energy flux on the surface temperature of the propellant samples is not significant during pyrolysis and ignition.

- 10) A preparation zone similar to the dark zone for double-base propellant flames was observed. A very small temperature gradient was observed near the propellant surface during ignition. This indicates that the energy consumed for pyrolysis of the condensed phase is supplied solely by the incident laser fluxes.
- 11) As the ambient pressure and incident energy flux are decreased, the amount of H_2 , CO_2 , and CO also decreased.

III. CRACK PROPAGATION AND BRANCHING IN BURNING SOLID PROPELLANTS

3.1 INTRODUCTION

3.1.1 Motivation and Objectives

Solid propellant rocket safety is a key factor in several of today's most important civilian and military propulsion systems. With both civilian and military agencies presently pursuing solid rocket booster safety and ballistic risk assessment programs, near-term advances in this area are foreseeable. Of particular concern is overpressurization and subsequent catastrophic failure of a rocket motor due to anomalous burning, which may be caused by the presence of voids, cracks, or debonded regions in the propellant grain. Such regions are susceptible to further damage under transient loading conditions. A theoretical model has been developed to predict the flame spreading and combustion processes inside a propellant cavity⁶² and various models have also been developed for crack initiation and growth in viscoelastic, inert material.⁶³⁻⁶⁶ However, the coupling effects of these two processes are complicated and not totally understood. Based on previous work by Kuo and co-workers⁶⁷⁻⁶⁹ on crack growth in burning propellant grains, a set of governing dimensionless parameters have been identified to obtain empirical correlations.

The primary objectives of this research are:

- a) to define a group of meaningful dimensionless parameters for characterizing the operating conditions and resulting damage of a solid propellant sample;

- b) to obtain test data necessary for developing correlations between the dimensionless parameters; and,
- c) to establish correlations, demonstrating a methodology for generating useful safety criteria.

3.1.2 Brief Survey of Related Work

Early studies of the crack propagation phenomena under burning conditions by Siefert and Kuo⁶⁷ provided good insight into the basic mechanisms involved. They studied the crack propagation process of a burning propellant sample of constant geometry under varying pressurization rates. Experimental evidence supported the assumption that the crack propagation velocity was limited by the rate of deformation of the crack cavity walls. In this case, a critical stress state was maintained in the failure zone at the crack tip. A nearly linear relationship between the crack velocity and pressurization rate was observed,

$$V_p \text{ (m/s)} = 0.086[\text{dp/dt(MPa/s)}]^{0.637} \quad (3-1)$$

For low pressurization rates the crack tip maintained its original contour. However, at pressurization rates on the order of 20 GPa/s, the crack tip appeared to square off and a fan structure developed suggesting the occurrence of crack branching and microstructure damage. It is interesting to note that the maximum crack velocities measured correspond to terminal velocities of inert propellants and rubber reported by Gent and Marteny.⁷⁰

Further studies by Kuo, Moreci and Mantzaras^{68,69} have identified four different modes of damage which were related to the

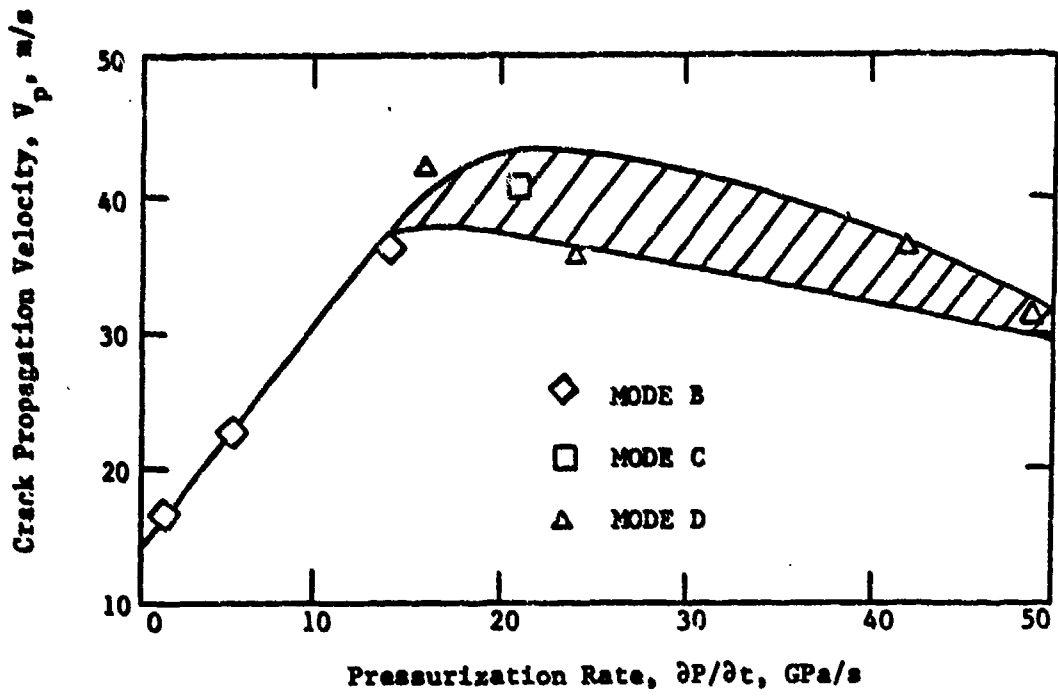


Fig. 31. Crack Propagation Velocity versus Pressurization Rate

pressurization rate of the crack cavity. Figure 31 shows the measured crack propagation velocity as a function of pressurization rate and where each of these modes was observed. Mode A represents little or no increase in crack length and corresponds to very low pressurization rates. No departure from normal burning is expected for this case. Mode B represents the propagation of a single crack. The rate of crack growth increases almost linearly with pressurization rate in the range of 1.4 to 15.0 GPa/s. Although burning is enhanced at the crack tip, the overall increase in burning due to the damage is not significant. Mode C represents an initial single crack propagation with local branching at various locations. This was observed for intermediate pressurization rates and has the potential of significantly increasing the burning surface area. Mode D represents crack branching from the initial crack tip location in either discrete macrocracks or a fan of numerous smaller cracks. This type of damage was characteristic of higher pressurization rates and also can significantly increase the burning surface area. Some of the data from these experiments, as well as newly acquired data, were used in the current analysis.

3.2 EXPERIMENTAL SETUP

3.2.1 Selection of Sample Propellant Type

In selecting a propellant sample for this research, the following criteria were considered:

- a) the propellant must be available for a basic study in a university environment;
- b) its combustion behavior must be well characterized;
- c) its mechanical properties and failure criterion under non-burning conditions must be known; and,
- d) propellants of the same family must be available so that similar tests can be conducted to determine the effect of burning rate and oxidizer size.

Two composite propellants (ARC 5051 and ARC 4525) were selected. Each of these contain 27% HTPB and 73% AP with average oxidizer particle sizes of 200 μ m (ARC 5051) and 20 μ m (ARC 4525). Due to the similarities in composition thermodynamic properties such as enthalpy, density, burning rate, etc., are nearly equal. Their combustion behavior and mechanical properties have been well characterized. In addition, propellants of similar composition but with different burning rates are available for future studies. Although these propellants have a lower solids loading than the typical high-energy solid propellants used in most of today's advanced rocket propulsion systems, once the basic method for determining crack combustion correlations has been established, similar studies can be made for other propellants.

3.2.2 Sample Configuration

The two-dimensional sample configuration used in previous studies is adopted for this study (Fig. 32). This general geometry is similar to one point of a star grain or to a segment of a grain containing a void. This configuration provides an initial crack of variable length and propagation along the horizontal axis. The geometric parameters ψ_0 and ψ_1 can also be varied to represent different local boundary conditions of the damaged zone.

3.2.3 Test Setup

The test setup was designed to induce combustion and mechanical damage in a localized zone of a pre-cut propellant sample by subjecting it to high-pressure, high-temperature gases and to interrupt the burning by rapid depressurization for sample recovery. In these tests variations of several independent parameters were made, including pressurization rate, initial crack length, sample geometry and propellant composition. The damage was then measured in terms of crack propagation velocity, extended crack length and number of cracks.

3.2.3.1 Test Chamber

The test rig (Fig 33) consisted of a high-pressure, windowed chamber with the following subsystems:

- a) a driving motor to pressurize the free volume of the chamber;
- b) a rupture disk and venting port to rapidly depressurize the chamber; and,
- c) a nitrogen injection system to cool the exposed surfaces and reduce the chance of sample reignition.

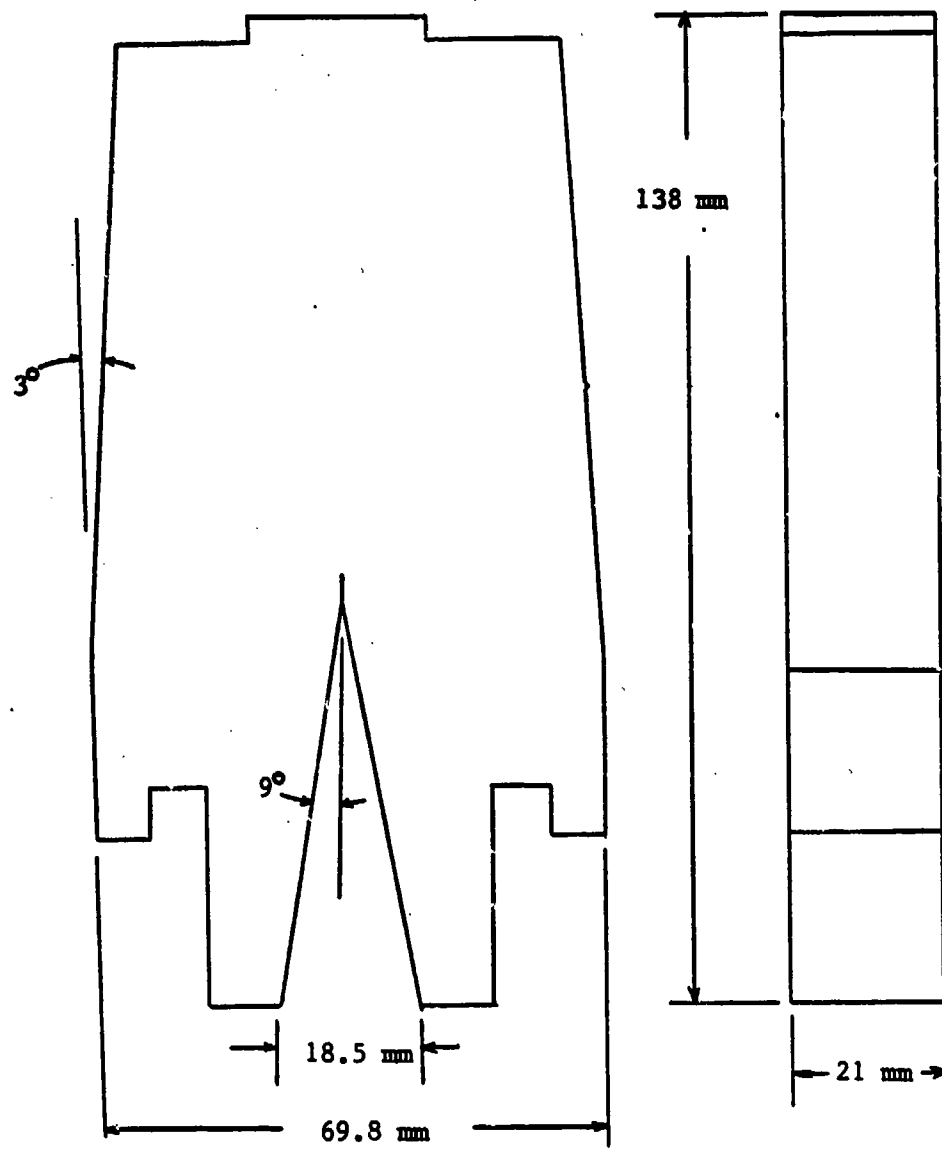


Fig. 32. Propellant Sample Configuration Before Loading

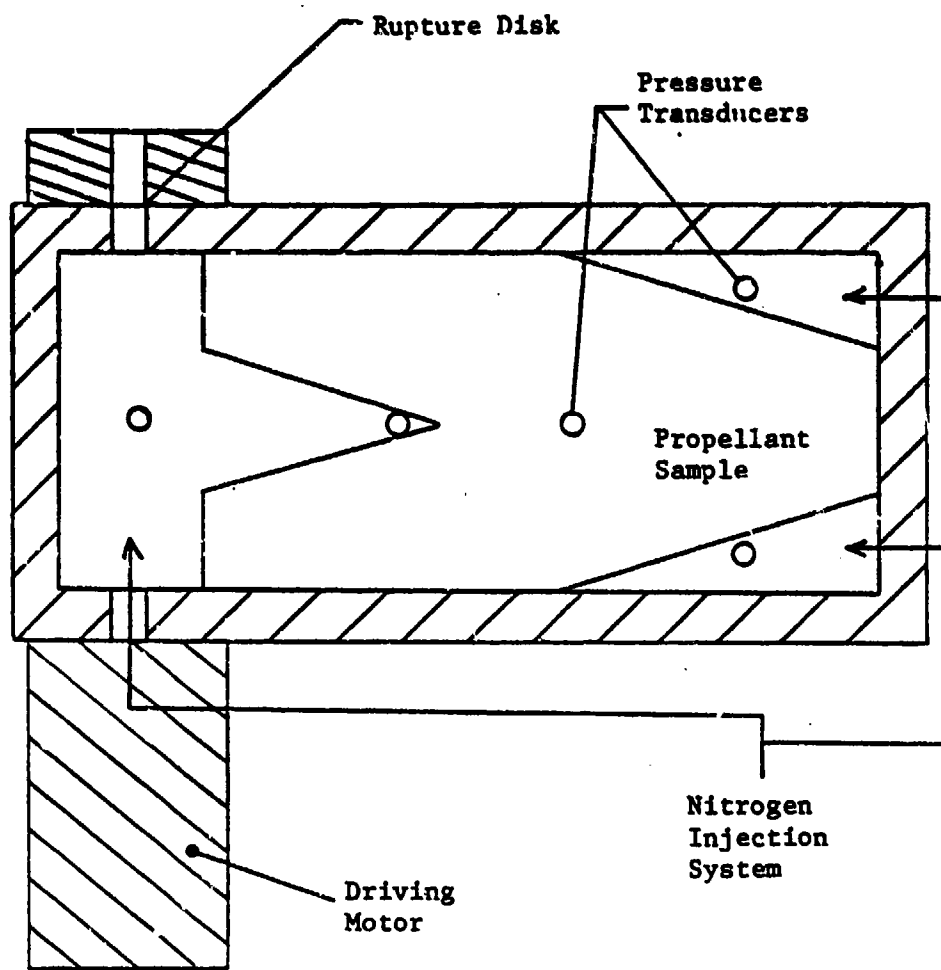


Fig. 33. Test Chamber

3.2.3.1.1 Driving Motor

The driving motor contained four key components (Fig 34). The ignition primer (type M52A3B1), when supplied with three to four volts DC, would fire and in turn ignite the propellant shavings. The shavings burn extremely fast due to their very high burning surface area. Their purpose was to supply hot gases and boost the pressure in the segment containing the main igniter charge. The igniter charge would then burn, exhausting through the perforated nozzle into the main chamber. By varying the mass of the main igniter charge, pressurization rates ranging from near zero to 50 Gpa/s were achieved.

3.2.3.1.2 Rupture Disk and Venting Port

When the chamber pressure exceeds a predetermined value the brass rupture disk bursts, allowing the high pressure gases to escape through the venting port. As described by De Luca,⁷² dynamic extinction can be achieved by exceeding a critical depressurization rate. This rate increases as chamber pressure increases and is also substantially affected by propellant composition. Due to its complexity, no attempt was made to characterize the extinction properties of the test propellants. Instead, an exit port area of 2.54 cm^2 , based on experimental data of Kuo and Moreci,⁶⁸ used with rupture pressures between 7.0 and 15.0 MPa proved to be sufficient.

3.2.3.1.3 Nitrogen Injection System

After the rupture disk bursts and the chamber pressure is reduced, hot spots on the chamber walls could reignite the propellant surfaces and the sample would be completely consumed. In an effort to improve the reliability of interrupting the burning process, nitrogen was

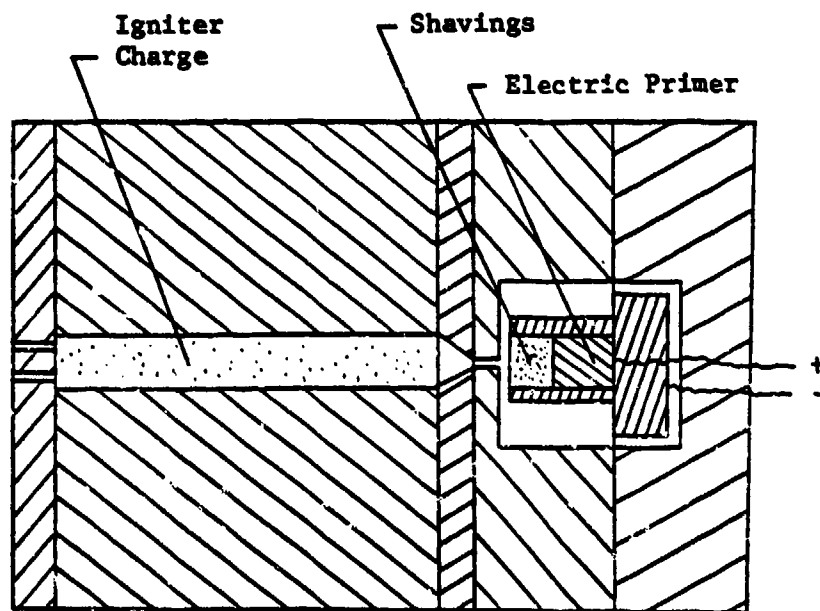
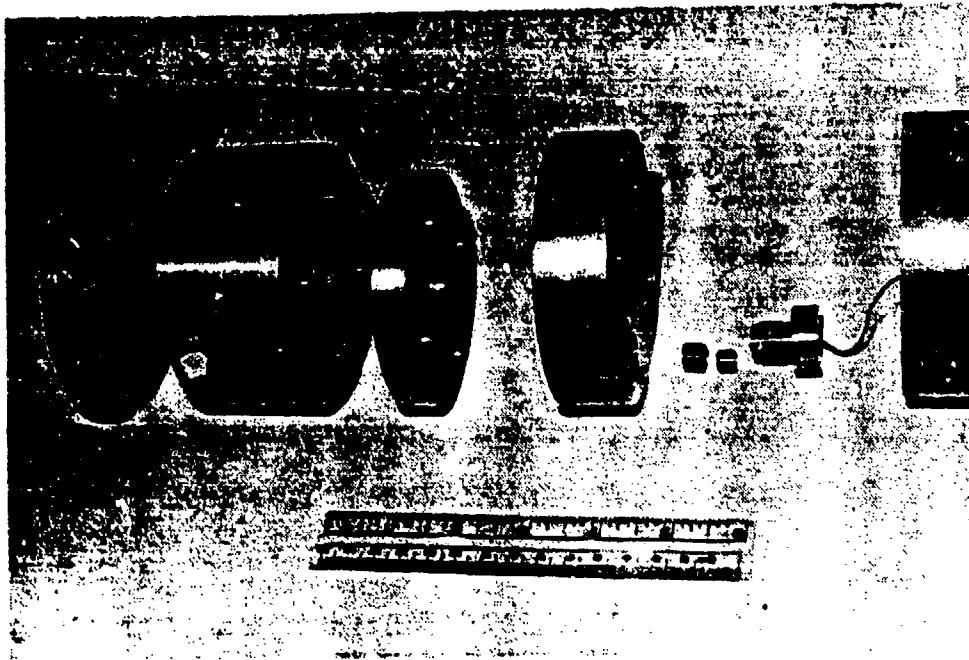


Fig. 34. Driving Motor

injected following depressurization to cool the surfaces of the free volume.

3.2.3.2 Data Acquisition System

The data needed from these tests to calculate key parameters consisted of a pressure-time trace of the crack cavity as well as a visual record of the crack itself as it propagated. A complete schematic of the data acquisition system is shown in Fig 35.

3.2.3.2.1 Pressure Measurements

The pressure measuring device selected was a miniature piezoelectric quartz transducer (Kistler Model 601B1). This transducer has a 10% to 90% rise time of 3.0 microseconds over the range of 0 to 15,000 psi. This was more than adequate for measuring pressurization rates of up to 50 GPa/s with rise times on the order of 1 millisecond. To protect the transducers from the high temperature product gases, they were recess-mounted in water-cooled adapters. An insulated high-impedance cable with a nominal capacitance of 30 pF/ft was used to transmit the signal from the transducer to the charge amplifiers. The signal attenuation under the test conditions was less than one percent.

The charge amplifiers (Kistler Model 504E) output the transducer charge signal as an amplified voltage. Calibration is achieved in the charge amplifier by supplying a DC voltage of equal magnitude to that of the pressure transducer sensitivity. The output voltage of the charge amplifier is then adjusted to satisfy the equation

$$V_{out} = \frac{-V_{in} \times 1000pF}{Range \times Sensitivity} \quad (3-2)$$

A typical range setting of 2000 psi/volt resulted in a calibration

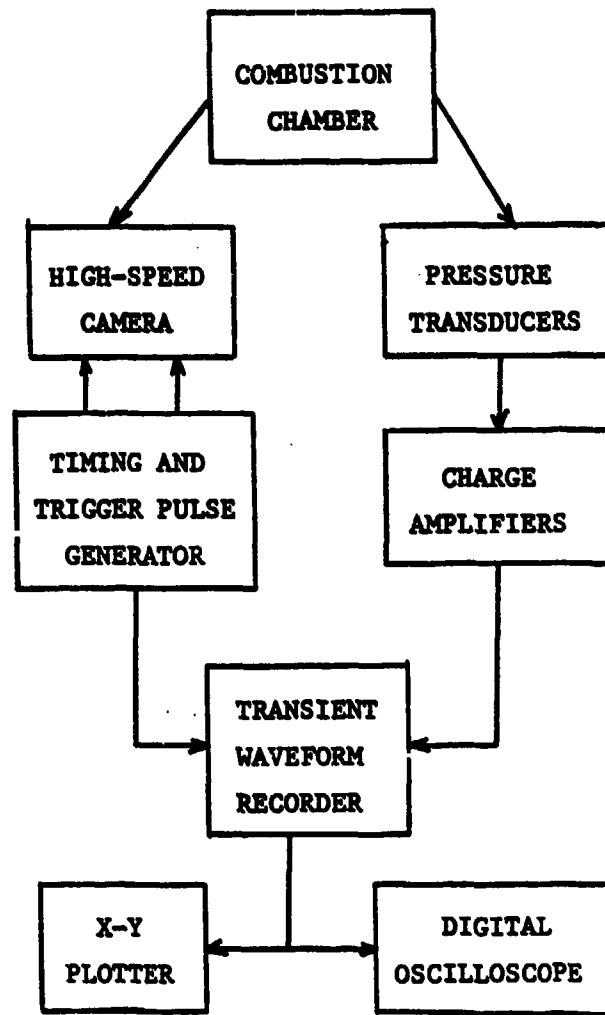


Fig. 35. Data Acquisition System

output of 0.5 volts. A long time constant was used to provide a continuous signal.

The output from the charge amplifiers was recorded on a Physical Data Model 515A Transient Waveform Recorder. It recorded the voltage signals at sampling intervals of 5 to 50 microseconds for the initial pressurization period and then shifted to a sampling rate of 2.5 to 5 milliseconds in order to extend the total time recorded. The limiting factor was its maximum capacity of 4096 data points. The recording mechanism was triggered by a small signal from the transducer in the crack cavity. A negative delay of 512 data points was used to insure the beginning of the event was recorded. The recorded signal could then be played back to a Nicolet Digital Oscilloscope for analysis and recording on floppy disk or to an X-Y plotter for a hardcopy.

3.2.3.2.2 High Speed Film Recording

A Hycam, 16 mm camera was used to record the ignition, combustion, and crack propagation of the propellant sample through a viewing port in the chamber. Typical framing rates were 5,000 frames per second in a half frame format resulting in 10,000 pictures per second. In order to insure the event occurred before the roll of film was completely exposed, the camera was used to trigger the ignition of the driving motor. The camera was started and when a prescribed footage of film was exposed, allowing the camera to reach the set film speed, an internal switch would close the igniter circuit. This would also trigger a common time pulse which was recorded both on the film and on the Physical Data Recorder. Another light pulse with a frequency of 1 KHz was also recorded on the film, to one side of the main image, in order to verify

the framing rate.

3.2.4 Test Procedure

Appendix F contains a complete checklist and sample data sheet used for the interrupted crack propagation tests. The following is a brief description of the key steps in a typical test firing:

- a) measure the main ignitor charge and shavings and assemble ignitor. Measure the resistance of the primer and short the primer circuit;
- b) measure and record the crack geometry of the propellant sample. Cover all surfaces, except crack cavity, with flame retardant grease to prevent flame spreading over those surfaces. Install the sample and bolt on the window and retainer;
- c) install pressure transducers and calibrate the charge amplifiers. Connect amplifier outputs to the Physical Data recorder;
- d) set up the high-speed camera and test ignition circuit;
- e) put charge amplifiers in the OPERATE position, reset the Physical Data recorder and start the camera;
- f) when the rupture disk bursts, open the nitrogen line;
- g) turn off charge amplifiers, store and plot the pressure traces and disassemble the chamber to examine the recovered sample.

3.3 THEORETICAL ANALYSIS

3.3.1 Crack Sample Geometry

Figure 36 shows the damaged sample geometry considered in this analysis. From this geometry, some key parameters can be defined. First, ψ_0 and ψ_1 are direct geometric factors affecting the crack propagation process, and the number of cracks n , is a key factor in defining the degree of damage.⁷² The affected volume, or damaged-zone volume is defined as

$$V_a = \pi L_D^2 b \quad (3-3)$$

The burning surface surface area in the affected region is given by

$$A_b = 2\pi(n+1)L_D b \quad (3-4)$$

For this analysis, a specific burning surface area is defined as

$$A_s = \frac{A_b}{V_a} = \frac{2(n+1)}{L_D} \quad (3-5)$$

The functional forms of equations (3-3) and (3-5) are

$$V_a = V_a(L_D, b) \quad (3-6)$$

$$A_s = A_s(L_D, n) \quad (3-7)$$

3.3.2 Determination of Mechanical Properties

A series of mechanical tests was conducted by Harbert and Schapery⁷³ to determine the mechanical properties of the two propellants (ARC 5051 and ARC 4525) under non-burning conditions.

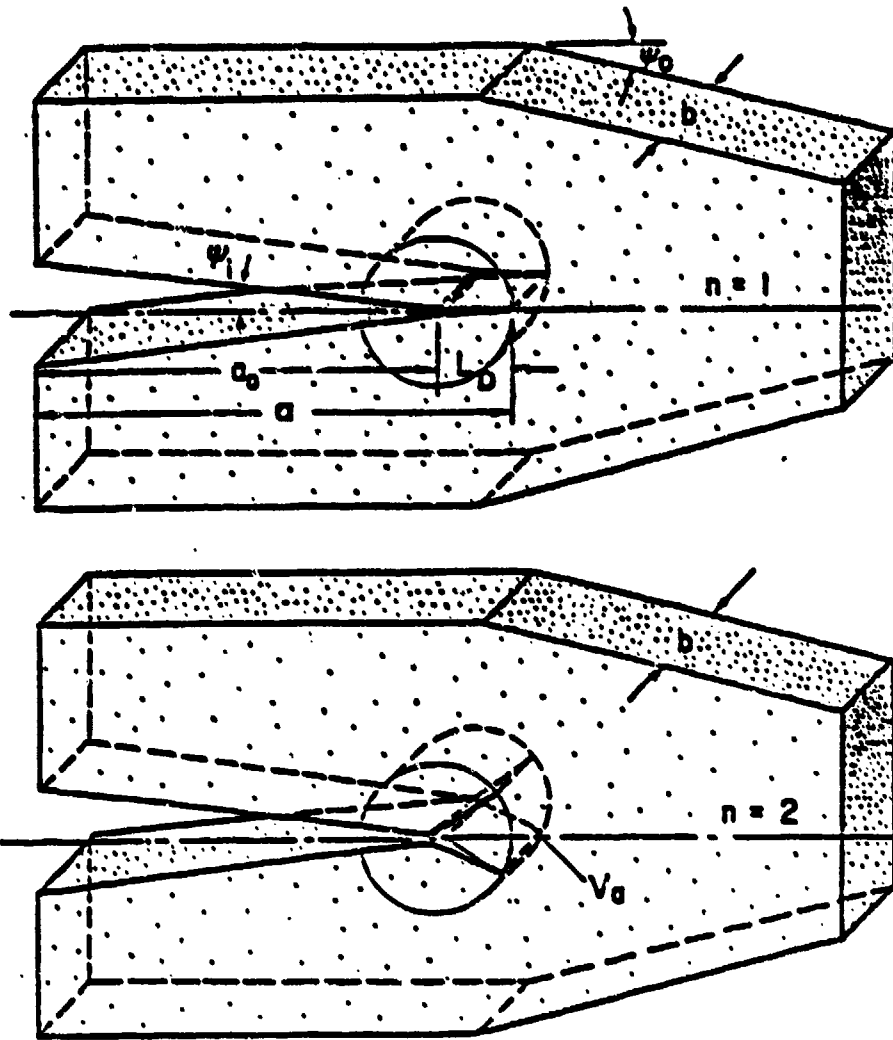


Fig. 36. Geometry of the Damaged Propellant Sample

3.3.2.1 Relaxation Modulus

Uniaxial constant strain tests on propellant bar specimens were performed at various temperatures. Relaxation moduli versus time data are plotted for each temperature. In order to obtain a continuous curve for all temperatures, the relaxation moduli are plotted versus a shifted time ξ , where

$$\xi = t/a_T \quad (3-8)$$

The time shift factor a_T was determined based on a reference temperature of 297 K (i.e., $a_T = 1.0$ at 297 K). Figure 37 shows the functional relationship between temperature and time shift factor. The resulting master relaxation curve for each propellant is shown in Figure 38.

3.3.2.2 Crack Propagation Velocity

Crack growth tests were conducted on strip specimens with a precut crack (Fig. 39) at different crosshead rates. The crack velocity and strain were measured directly and the stress intensity was calculated using

$$K_I = \sigma \sqrt{h/2(1-\nu^2)} \quad (3-9)$$

where Poisson's ratio $\nu = 0.5$ and σ is the stress far from the crack tip exerted by the crosshead.⁷⁴ Figure 40 shows the relationship between crack propagation velocity and stress intensity factor for ARC 4525 propellant. It can be seen that the lines of constant strain are parallel (i.e independent of strain). This fact suggests the applicability of linear viscoelastic theory to characterize the crack propagation velocity.⁷⁵ The results of this theory can be expressed by the following power law

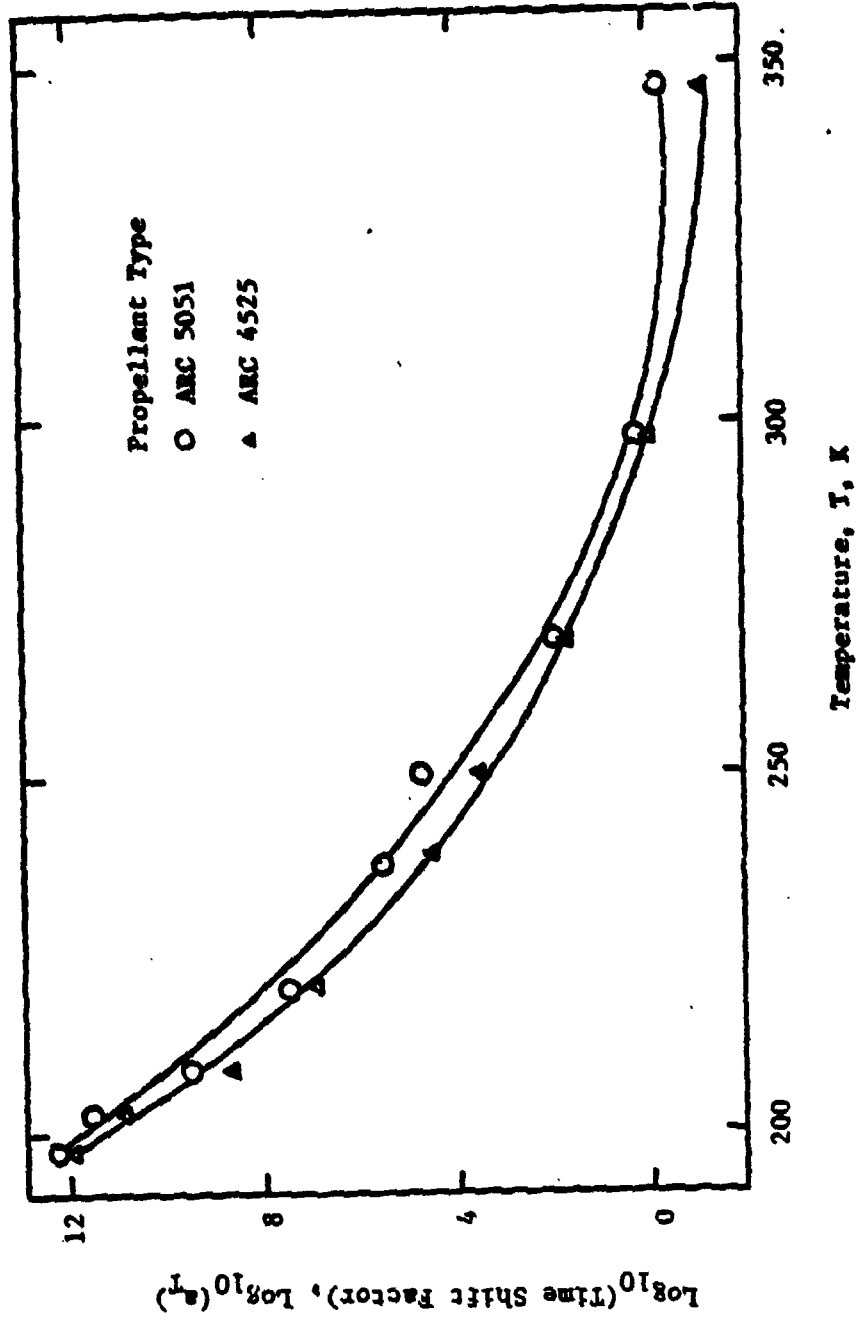


Fig. 37. Relaxation Modulus Time Shift Factor versus Temperature

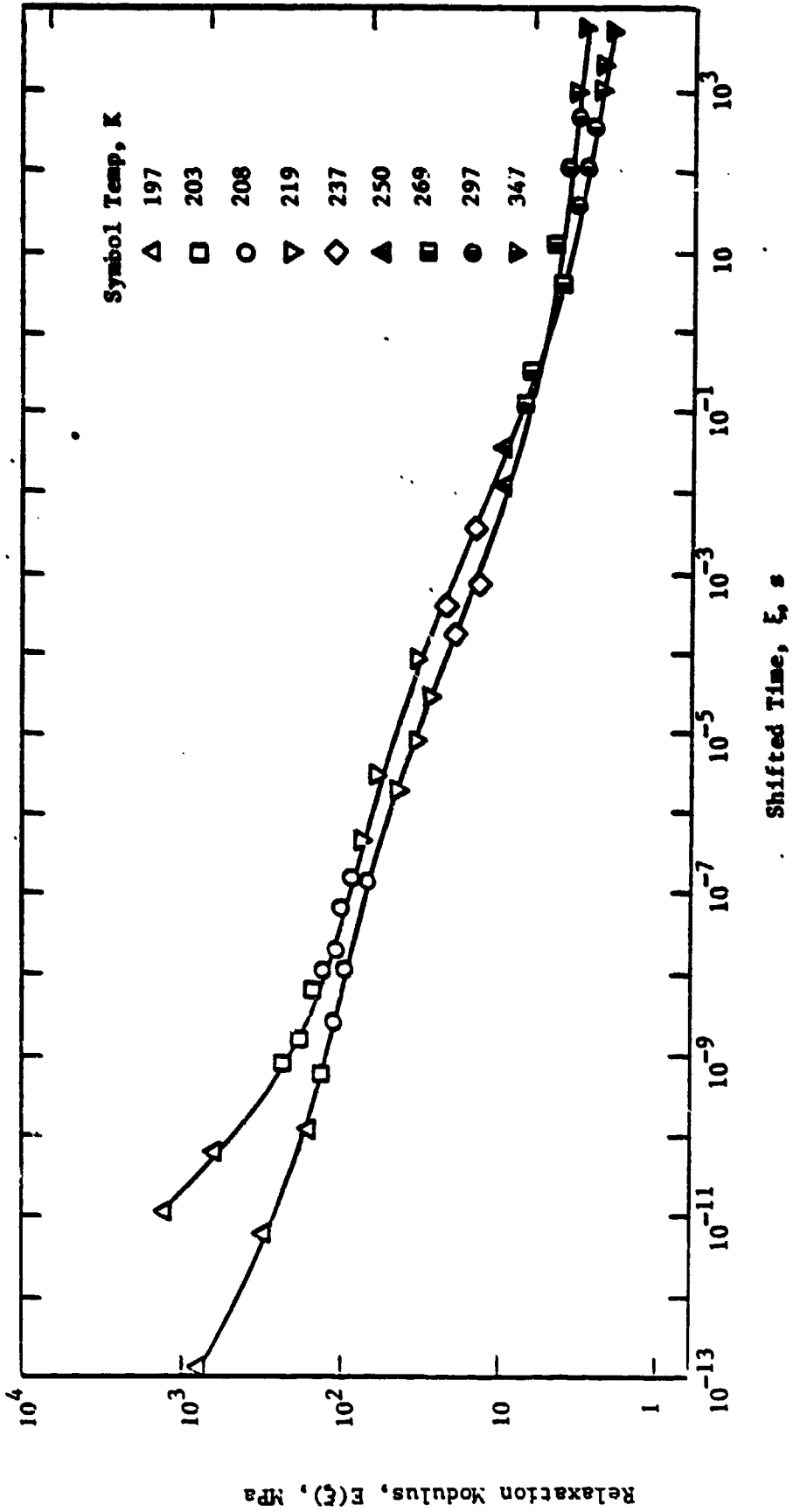


Fig. 38. Master Relaxation Curve

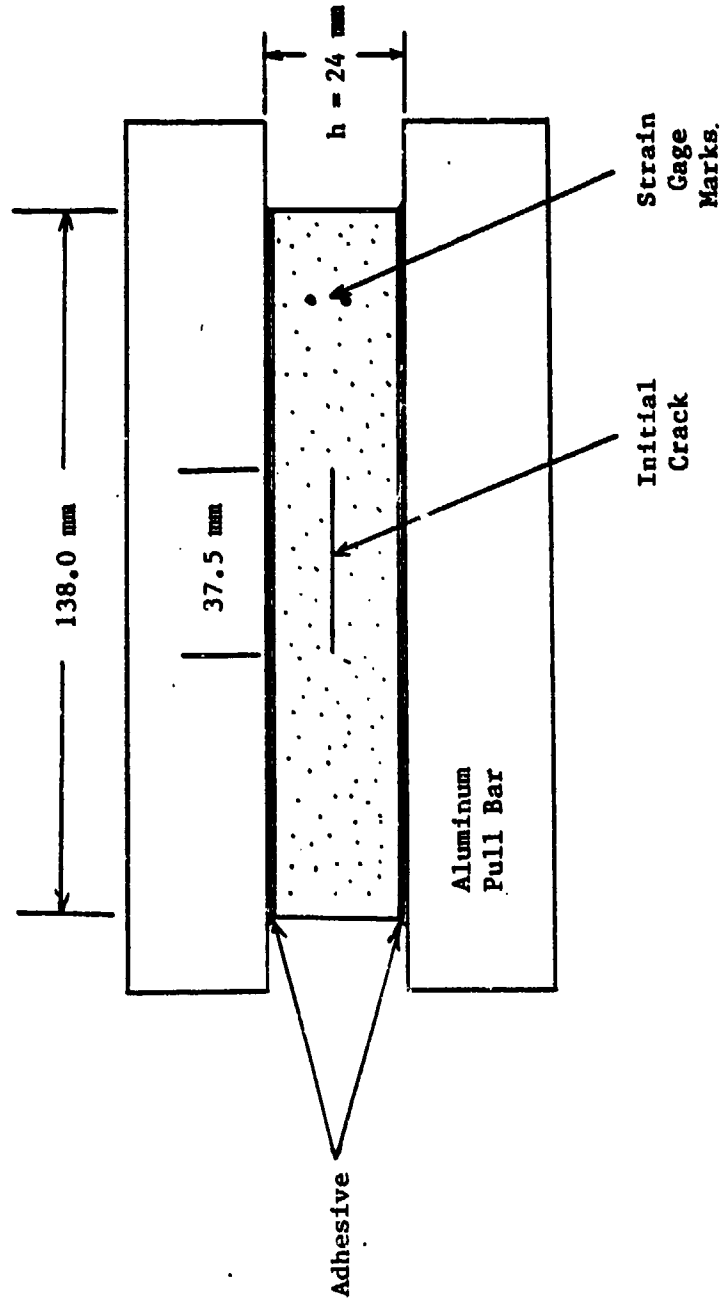


Fig. 39. Test Configuration for Crack Velocity Characterization

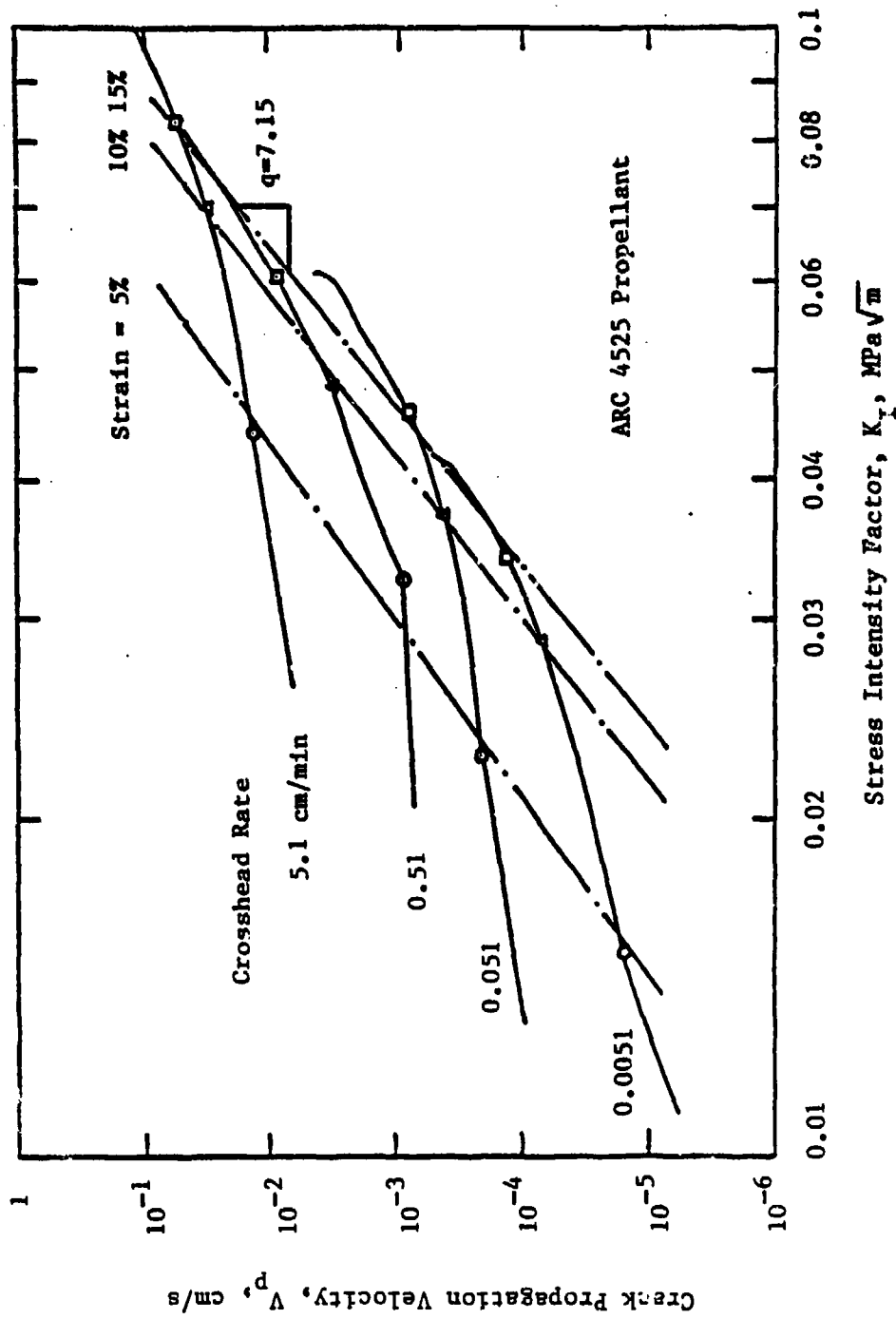


Fig. 40. Crack Propagation Velocity versus Stress Intensity Factor for ARC 4525

$$V_p = \frac{C}{a_T} (K_I)^q \quad (3-10)$$

In this equation q is the strain-independent slope obtained from Figure 40, and C is a material parameter which varies with strain. The functional representation of equation (3-10) is then

$$V_p = V_p(K_I, \epsilon, a_T) \quad (3-11)$$

3.3.2.3 Fracture Energy and Related Parameters

From an idealized crack propagation model for viscoelastic media as used by Knauss⁶³ and Schapery⁶⁴⁻⁶⁶, the fracture energy (Γ) can be defined as the energy required to elongate a segment of area dA to the point of failure. This quantity has the functional relationship

$$\Gamma = \Gamma(K_I, V_p, \sigma_{fm}) \quad (3-12)$$

where σ_{fm} is the maximum stress in the failure zone. The stress intensity factor is generally a function of the geometry of the continuum in which the failure zone is embedded and the stress in that zone, represented by chamber pressure in this application. Thus

$$K_I = K_I(a_0, \psi_0, \psi_1, P) \quad (3-13)$$

and

$$K_{Ic} = K_I \quad (3-14)$$

for crack initiation. From Langlois and Gonard,⁷⁶ the extended crack length can be related to stress intensity factor and the maximum stress in the failure zone

$$L_D = L_D(K_I, \sigma_{fm}) \quad (3-15)$$

3.3.3 Energy Balance on the Control Volume

An energy balance is applied to the control volume (Figure 41) in order to relate key parameters in the combustion process. The basic assumptions are:

a) The heat loss from the control volume to the surroundings is negligible since the damage occurs in an extremely short time interval (of the order of 10 ms).

b) The combustion gases of the driving motor are considered to follow the perfect gas law. This assumption is valid since the gas temperature is high (2000 K) and the maximum chamber pressure is less than 35 MPa.

c) $\dot{m}_{out} = 0$ for the time of interest since the initial damage occurs before the rupture disk bursts.

d) The gas phase control volume can be treated as a constant since the volume increase due to flow work and surface burning is extremely small compared to the total control volume during the time of interest. The conservation of energy for the gas phase can be written as

$$\frac{\partial E}{\partial t} = \dot{m}_{ign} h_{t,ign} + \dot{m}_p h_p - \dot{m}_{out} c_p T - \dot{Q} - P \frac{\partial V_c}{\partial t} \quad (3-16)$$

Using the basic assumptions, equation (3-16) reduces to

$$\frac{V_c}{\gamma-1} \frac{\partial P}{\partial t} = \dot{m}_{ign} h_{t,ign} + \dot{m}_p h_p \quad (3-17)$$

After replacing \dot{m}_p according to

$$\dot{m}_p = p_b^r A_b t \quad (3-18)$$

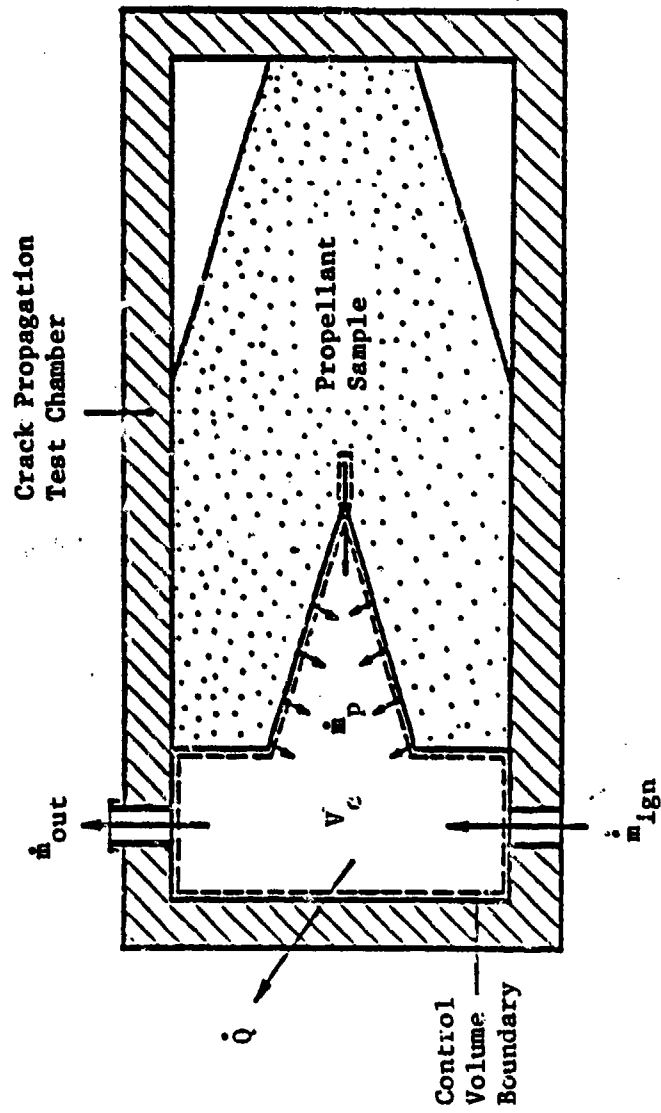


Fig. 41. Control Volume Used in Energy Analysis

where the total burning surface area A_{bt} can further be related to the crack geometry

$$A_{bt} = A_{bt}(V_a, A_s, L_D, a_o, \psi_i) \quad (3-19)$$

Equation (3-17) then takes on the functional form

$$\frac{\partial P}{\partial t} = \frac{\partial P}{\partial t}(V_o, \dot{m}_{ign}, h_{t,ign}, r_b, V_a, a_o, L_D, \rho_p, \psi_i, A_s, h_p) \quad (3-20)$$

The burning rate under a pressure transient has been characterized by Krier⁷⁷ as

$$r_b(t) = r_o \left[1 + \phi \frac{n\alpha_p}{P(t)r_o^2} \frac{dp}{dt} \right] \quad (3-21)$$

where r_o is the steady state burning rate according to the Saint-Robert law,⁷⁸ α_p is the solid phase thermal diffusivity, and n and ϕ are numerical constants. Since the thermal diffusivities were the same for both propellants⁷³ it also was treated as a numerical constant. The instantaneous burning rate can therefore be related as

$$r_b = r_b(P, \partial P/\partial t) \quad (3-22)$$

Since the flow from the driving motor is choked and the ignitor charge is made of the same propellant as the sample, the propellant enthalpy can be related to the stagnation enthalpy of the igniter gases as

$$h_p = \frac{2}{\gamma-1} h_{t,ign} \quad (3-23)$$

The propellants are essentially incompressible and of equal density, therefore

$$\rho_p = \text{constant} \quad (3-24)$$

From evidence obtained in crack propagation experiments,⁷² crack propagation velocity in the burning solid propellants is related to the following parameters:

$$V_p = V_p(\partial P/\partial t, P, m_{ign}, \Gamma, \psi_o, \psi_i, V_c, A_s, a_o, a_T) \quad (3-25)$$

3.3.4 Dimensional Analysis

Equations (3-6), (3-7), (3-11)-(3-15), (3-20) and (3-22)-(3-25) relate the twenty-three parameters (γ was assumed to be a numerical constant for the combustion product gases) affecting the crack propagation process. These twelve equations may be reduced to one equation involving twelve of the more significant parameters, namely

$$V_p = V_p(\partial P/\partial t, r_b, a_o, h_p, K_{I_C}, V_a, A_s, L_D, \psi_o, \psi_i, a_T) \quad (3-26)$$

3.3.4.1 Arrangement into Meaningful Dimensionless Groups

The Buckingham Pi Theorem⁷⁹ indicates that there exist nine independent dimensionless parameters involved in the crack propagation process. Three of the key parameters are already dimensionless, thus ψ_o , ψ_i and a_T were chosen as dimensionless parameters describing the geometry of the continuum around the damaged zone and the effect of initial propellant temperature on mechanical properties. In order to develop additional meaningful groups, the parameters which describe the degree of damage (i.e., L_D , V_a , A_s and V_p) were examined individually.

A desirable dimensionless parameter defining the extended crack length was the percentage increase in overall crack length. This dimensionless parameter was defined as

$$\pi_A = \frac{L_D}{a_0} = \frac{\text{Length of extended macrocrack}}{\text{Length of the initial crack}} \quad (3-27)$$

From the parameters V_a and A_s , two meaningful dimensionless groups could be formed,

$$\pi_B = \frac{V_a A_s^2}{L_D^2} = \frac{\text{Rate of increase of crack surface area}}{\text{Rate of increases of cross-sectional area of the affected region}} \quad (3-28)$$

$$\pi_C = L_D A_s^{-1} = n, \text{ number of macrocracks of length } L_D \quad (3-29)$$

The crack propagation velocity was normalized to the normal regression rate of the surface due to burning,

$$\pi_D = \frac{V_p}{r_b} = \frac{\text{Crack propagation Velocity}}{\text{Burning rate of the main propellant}} \quad (3-30)$$

The remaining dimensionless parameters relate the input energy from the propellant and the pressurization rate to the critical values for crack propagation and were grouped as follows:

$$\pi_E = \frac{h_p \rho_p r_b A_s \pi L_d^2}{v_p [K_{Ic}^2 (1-\nu^2)/E_{ref}]} = \frac{\text{Rate of thermal energy input from propellant product gases}}{\text{Strain energy release rate required for crack propagation}} \quad (3-31)$$

$$\pi_F = \frac{\frac{dP}{dt} L_d^{3/2}}{K_{Ic} r_b} = \frac{\text{Rate of change of pressure force exerted on the crack surface}}{\text{(critical stress for fracture) x (rate of increase of flow area in the damaged zone)}} \quad (3-32)$$

The additional constants such as density, sample thickness and Poisson's ratio were added to give the groups their respective physical meaning.

3.3.4.2 Functional Relationships Between Dimensionless Parameters

The Dimensionless parameters π_A , π_B , π_C , π_D characterize the

degree of damage in the propellant sample. The driving force causing this damage (i.e. the initial pressurization rate and thermal energy input from the propellant gases) are characterized by the dimensionless parameters π_E and π_F . These parameters were used together with ψ_0 , ψ_1 and a_T for constructing the following empirical correlations to predict the crack propagation and branching processes:

$$\pi_A = \pi_A(\pi_E, \pi_F, \psi_0, \psi_1, a_T)$$

$$\pi_B = \pi_B(\pi_E, \pi_F, \psi_0, \psi_1, a_T)$$

$$\pi_C = \pi_C(\pi_E, \pi_F, \psi_0, \psi_1, a_T)$$

$$\pi_D = \pi_D(\pi_E, \pi_F, \psi_0, \psi_1, a_T)$$

(3-33)

3.4 RESULTS

3.4.1 Determination of Dimensionless Parameters

Several tests were conducted using the apparatus previously described. From the pressure data, film data and known mechanical and thermodynamic properties, values for each of the parameters could be deduced.

3.4.1.1 Pressure Loading in the Damaged Zone

Figure 42 shows the pressure-time trace at three key locations in a typical test. Location 1 corresponds to the chamber free-volume and location 2 corresponds to the initial crack tip location and the 3rd is further along the crack propagation direction. The first curve is the driving pressurization rate used in calculating the dimensionless parameters since it is generally independent of the initial crack configuration. The pressure trace for the second location illustrates the increased pressurization rate and peak pressure experienced at the tip of an opening crack. This may be caused by the delayed opening of the crack and/or the increased burning rate in the failure zone. As seen, the peak pressure in this case was 13.8 MPa (2000 psi) when the rupture disk burst. The chamber pressure then dropped rapidly, and the sample was recovered. Figure 43 is a close-up photograph of the damaged zone showing the branching which occurred.

Figure 44 is a similar pressure trace for another test. The rupture disk burst earlier in this case (7.0 MPa), which may have contributed to the reignition and burn-out of the sample. The early

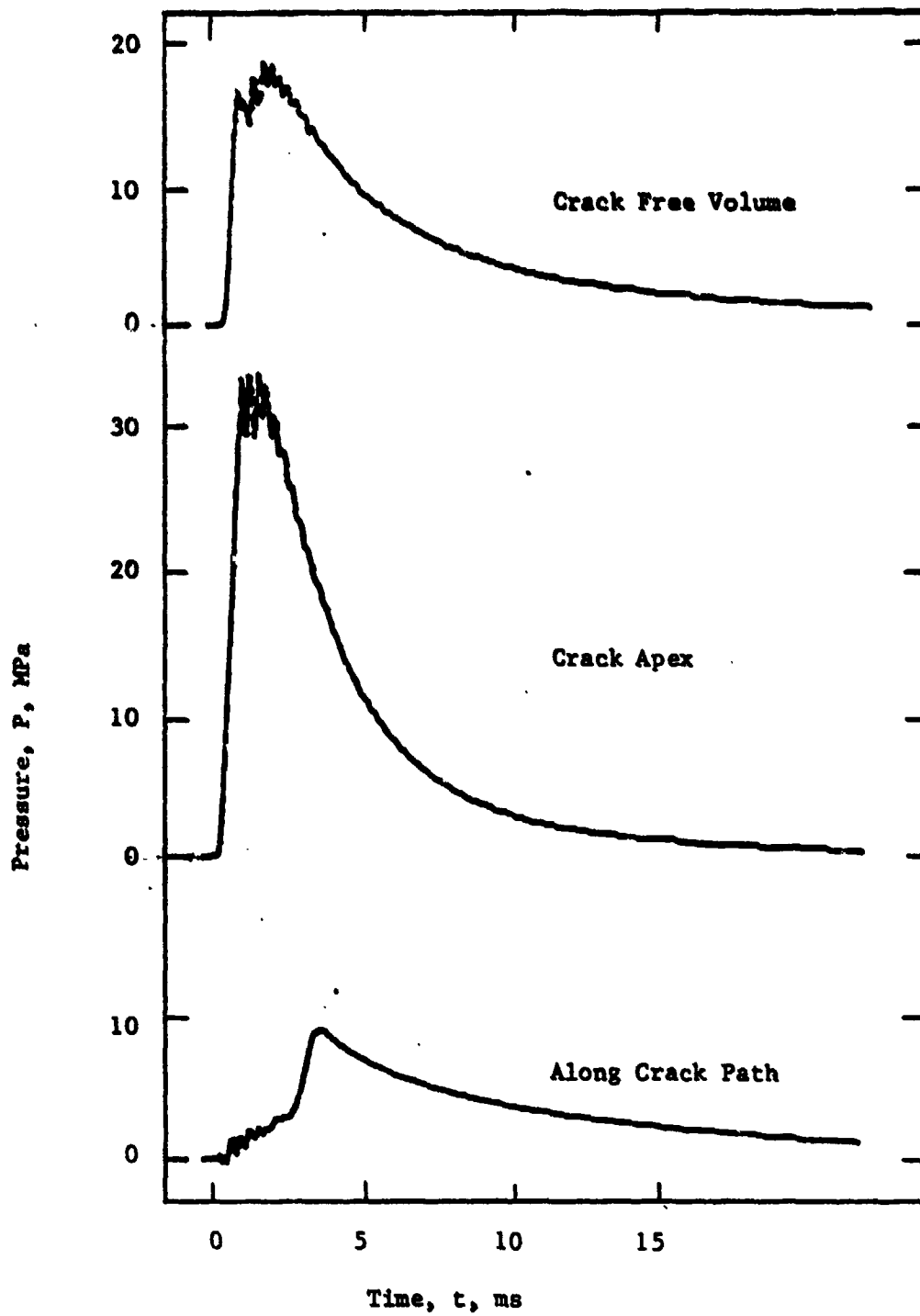
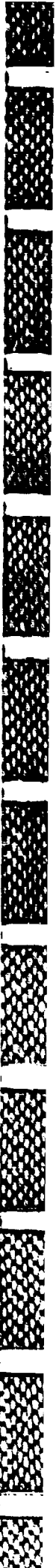


Fig. 42. Pressure-Time Trace for DNICP 27



Fig. 43. Recovered Sample from DNICP 27



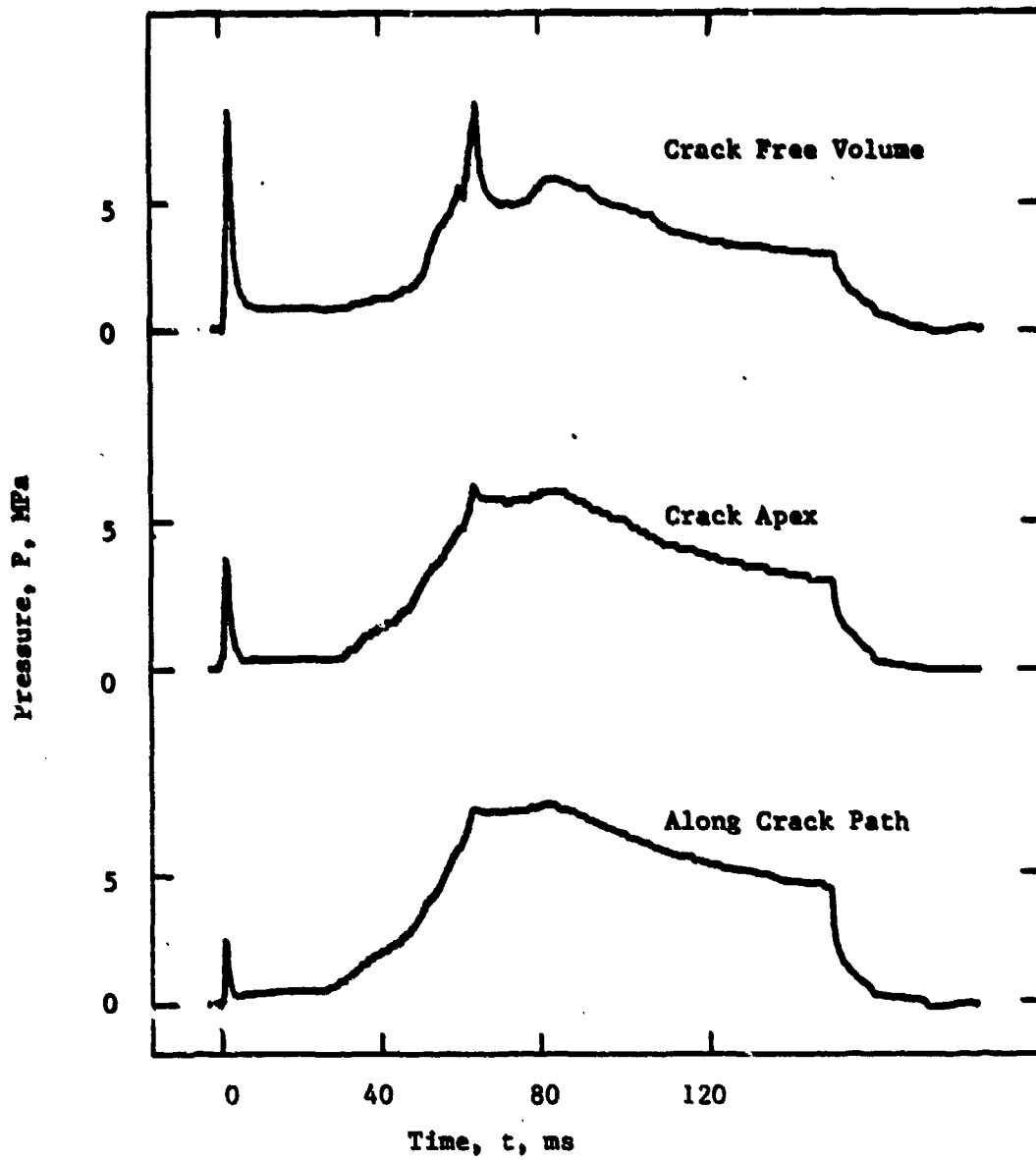


Fig. 44. Pressure-Time Trace for DNICP 40

rupture appeared to affect the peak pressure at the crack tip as it occurred during the depressurization of the free volume.

3.4.1.2 Interpretation of the Film Data

The degree of damage to the propellant sample was characterized by examining the film record of the event. A typical film record of a Mode B, single crack propagation is shown in Figure 45. Table IV contains a frame-by-frame description of the event. The instantaneous bright flame contours caused by burning in the crack are used to define the crack shape and length. From the contour (Figure 46), the crack tip location was measured as a function of time. Thus the crack velocity, extended length and number of macrocracks were deduced. In this test the initial crack length was longer than in previous tests. Figure 47 shows that the luminous flame front moved through the initially closed region and the crack propagation region at the same rate. The sharp reduction in propagation rate was caused by the depressurization of the chamber. A typical instantaneous bright flame contour for a branching experiment is shown in Figure 48.

3.4.1.3 Determining Other Key Parameters

In order to calculate each dimensionless parameter the values of r_b , K_{IC} and E_{ref} must be determined. To represent the normal regression of the propellant surface in relation to the crack propagation, a steady state burning rate was calculated using Saint Robert's law⁷⁸

$$r_b = aP^n \quad (3-34)$$

where P was the pressure at the time of crack initiation and a and n are burning rate constants given in Table V.⁸⁰

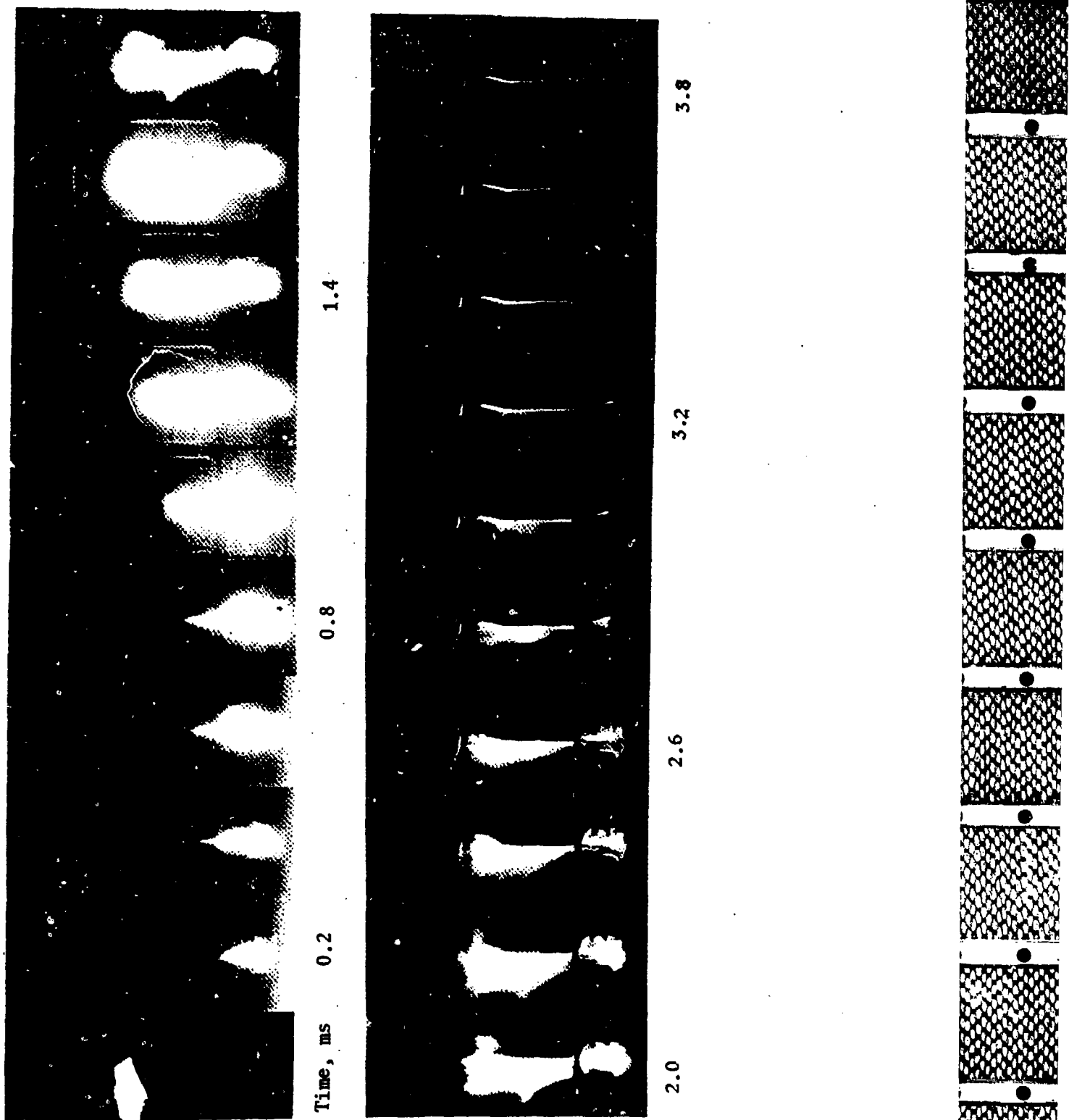
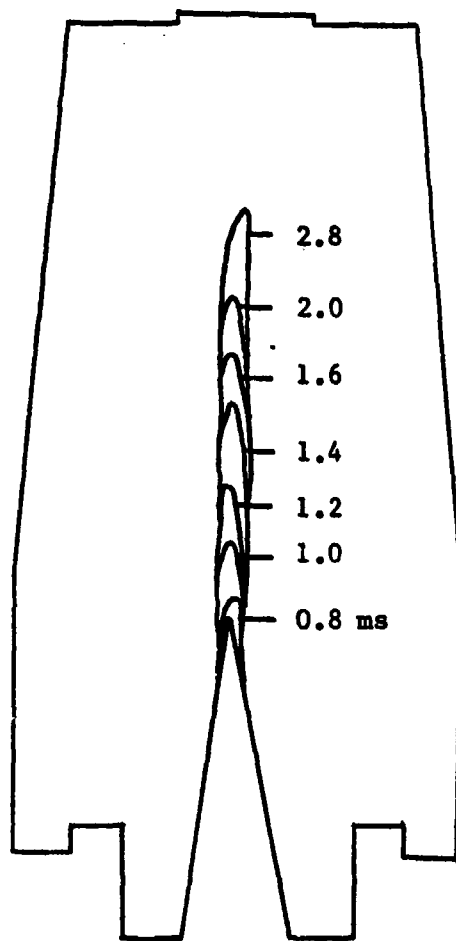


Fig. 45. Film Record from DNICP 40

Table IV. Film Interpretation of Crack Propagation Process

Picture No.	Time (ms)	Event
1-6	0-0.6	Igniter gases fill crack cavity.
7-12	0.6-1.2	Flame penetrates precut crack.
13-16	1.2-1.6	A single crack propagates. High pressure gas continues to flow into crack region.
17-28	1.6-2.8	Crack cavity is clearly seen. Propagation has stopped.
29-34	2.8-3.4	Rupture disk bursts and flame intensity is reduced.
35-	3.4-	Propellant sample is not extinguished and burns completely.





$$\frac{\partial P}{\partial t} = 12.0 \text{ GPa/s}$$

$$v_p = 35.4 \text{ m/s}$$

$$n = 1$$

Fig. 46. Instantaneous Bright Film Contour From DNICP 40

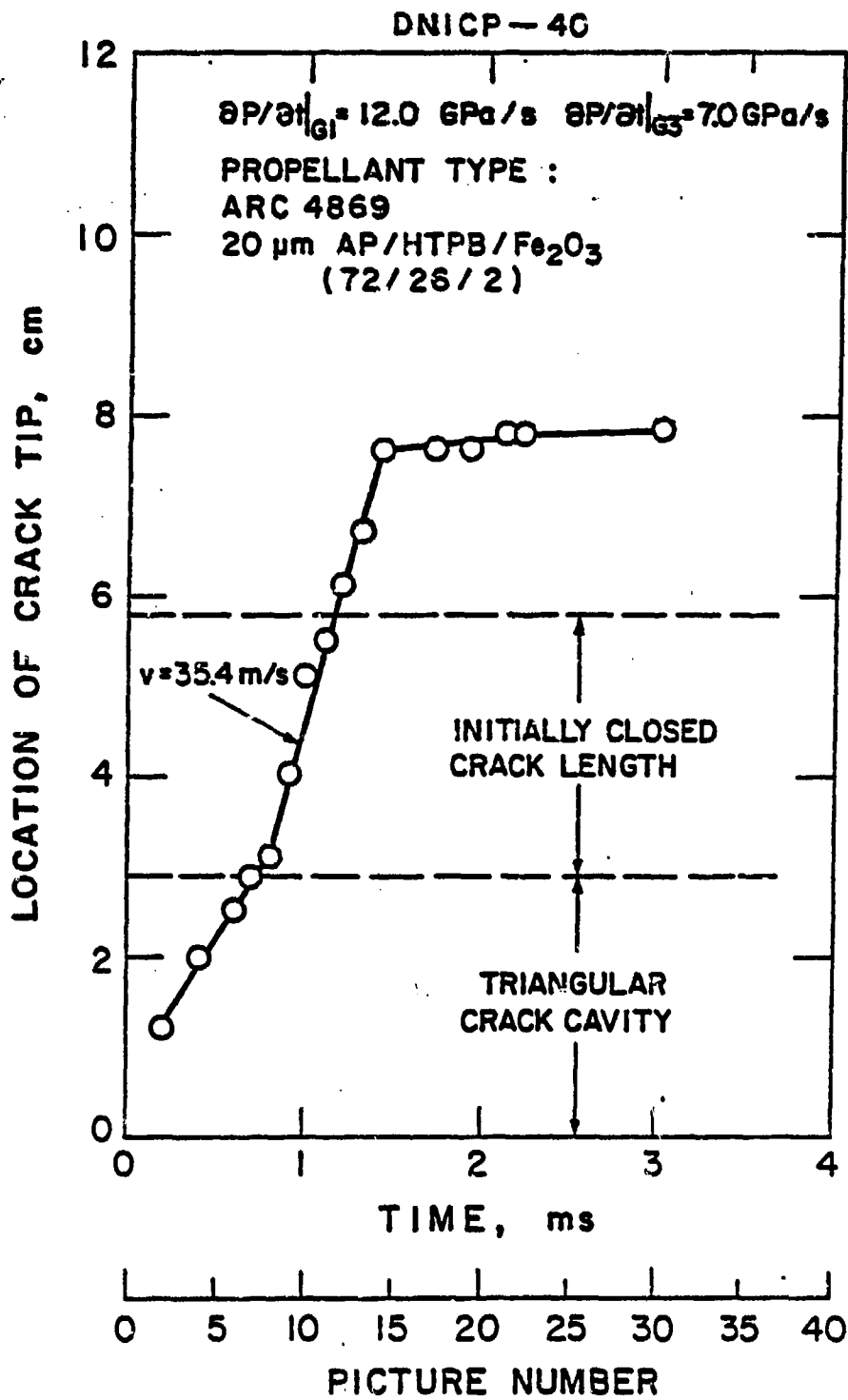
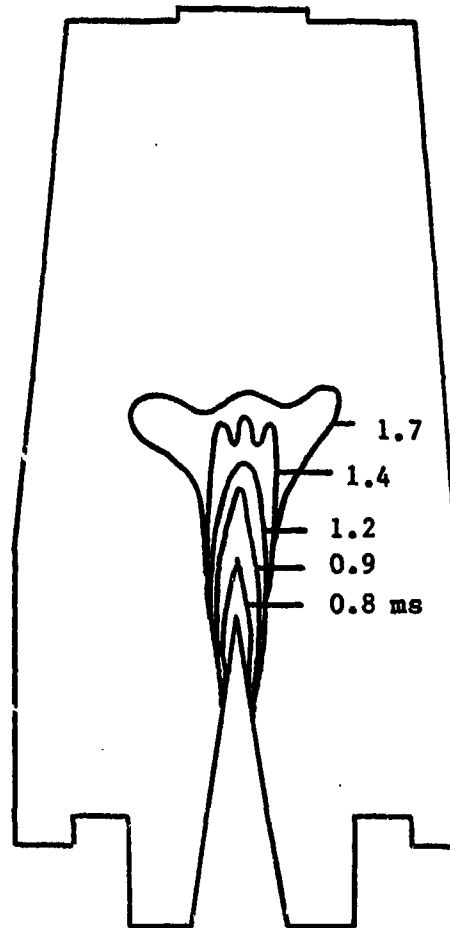


Fig. 47. Crack Tip Location versus Time for DNICP 40



$$\partial P / \partial t = 49.0 \text{ GPa/s}$$

$$V_p = 29.0 \text{ m/s}$$

$$n = 3$$

Fig. 48. Instantaneous Bright Film Contour From DNICP 31

Table V. Steady State Burning Rate Constants

Type	a (mm/s/(atm) ⁿ)	exponent n
ARC 4525	0.5849	0.5427
ARC 5051	0.8441	0.5611

The critical stress intensity factor K_{I_C} , was calculated using equations (3-9), (3-14) and the relationship

$$\sigma = P \cos \psi_i \quad (3-35)$$

The relaxation modulus E_{ref} , was taken from Figure 38 where t was the time of crack initiation.

3.4.2 Relationships Between Dimensionless Parameters

Using the data obtained from numerous experiments, several sets of values for the nine dimensionless parameters have been deduced (Table VI). With this data, the functional relationships of these parameters were obtained statistically using a multiple regression analysis program. The results can be expressed as

$$\pi_A = 20.697 \pi_E^{0.107} \pi_F^{0.181} a_T^{0.321} (\sin \psi_i)^{2.49} (\sin \psi_o)^{0.645} \quad (3-36)$$

$$\pi_B = 6.16 \times 10^{-7} \pi_E^{0.065} \pi_F^{0.254} a_T^{-0.78} (\sin \psi_i)^{-6.45} (\sin \psi_o)^{-0.985} \quad (3-37)$$

$$\pi_C = 7.389 \pi_E^{0.274} \pi_F^{0.042} a_T^{-0.021} (\sin \psi_i)^{1.14} (\sin \psi_o)^{-0.045} \quad (3-38)$$

$$\pi_D = 10.9 \times 10^4 \pi_E^{0.217} \pi_F^{0.076} a_T^{0.478} (\sin \psi_i)^{2.05} (\sin \psi_o)^{-0.117} \quad (3-39)$$

It is important to note that although the exponents of π_E and π_F are small compared to the other exponents, the values of these two

Table VI. Experimental Values of Dimensionless Parameters

Test No.	π_A	π_B	π_C	τ_D	τ_E	π_F	a_T	ψ_1	ψ_0
13	0.25	3.963	1	4420	0.309	2970	1.3	9.0	11.5
14	0.221	2.981	1	2420	0.115	1060	1.3	9.0	11.5
15	0.428	2.238	1	5960	1.077	6530	1.1	9.0	11.5
21	0.467	29.470	5	13490	18.930	186900	1.3	9.6	3.0
23	0.342	28.920	3	13400	8.163	110800	1.1	9.1	3.0
24	0.204	4.528	1	5940	0.439	3910	1.8	9.7	3.5
26	0.441	36.910	3	17000	18.300	132100	1.5	8.8	3.5
27	0.329	27.370	4	10250	13.120	41500	1.8	8.8	3.5
31	0.338	29.110	3	10900	15.310	79300	1.2	8.8	3.5
40	0.236	2.945	1	2720	0.473	3500	2.5	8.9	5.0

parameters are, in general, large compared to $\sin\psi_1$, $\sin\psi_0$ and a_T , and therefore have a dominant effect.

In order to check the reliability of these predictions, equations (3-36) through (3-39) are plotted with the values obtained from test data (Figures 49 through 52). These figures show that the predictions adequately characterize the experimental data. The multiple regression analysis calculated R^2 values greater than 89% for all correlations. R^2 is defined as the sample multiple coefficient of determination given by

$$R^2 = \frac{\sum(Y_i - \hat{Y}_i)^2}{\sum(Y_i - \bar{Y})^2} \quad (3-40)$$

where Y_i are the measured values, \bar{Y} is the mean value of Y_i and \hat{Y}_i is the predicted value of Y_i .

3.4.3 Discussion of Results

The expressions for π_A , π_B , π_C and π_D characterize the damage in the sample in terms of the extended macrocrack length, increase in burning surface area, number of macrocracks, and crack propagation velocity. From equations (3-36) through (3-39), the effects of the operating conditions characterized by π_E , π_F , ψ_0 , ψ_1 and a_T on the sample damage can be analyzed individually. The equations show that all damage parameters increase with π_E and π_F . The pressurization rate (π_F) is particularly dominant in extending the crack length and increasing the specific surface area. This agrees with previous studies⁶⁷⁻⁶⁹ which showed an increase in damage for higher rates of thermal energy input and higher pressurization rates.

Changes in ψ_0 change the confinement of the damaged zone allowing

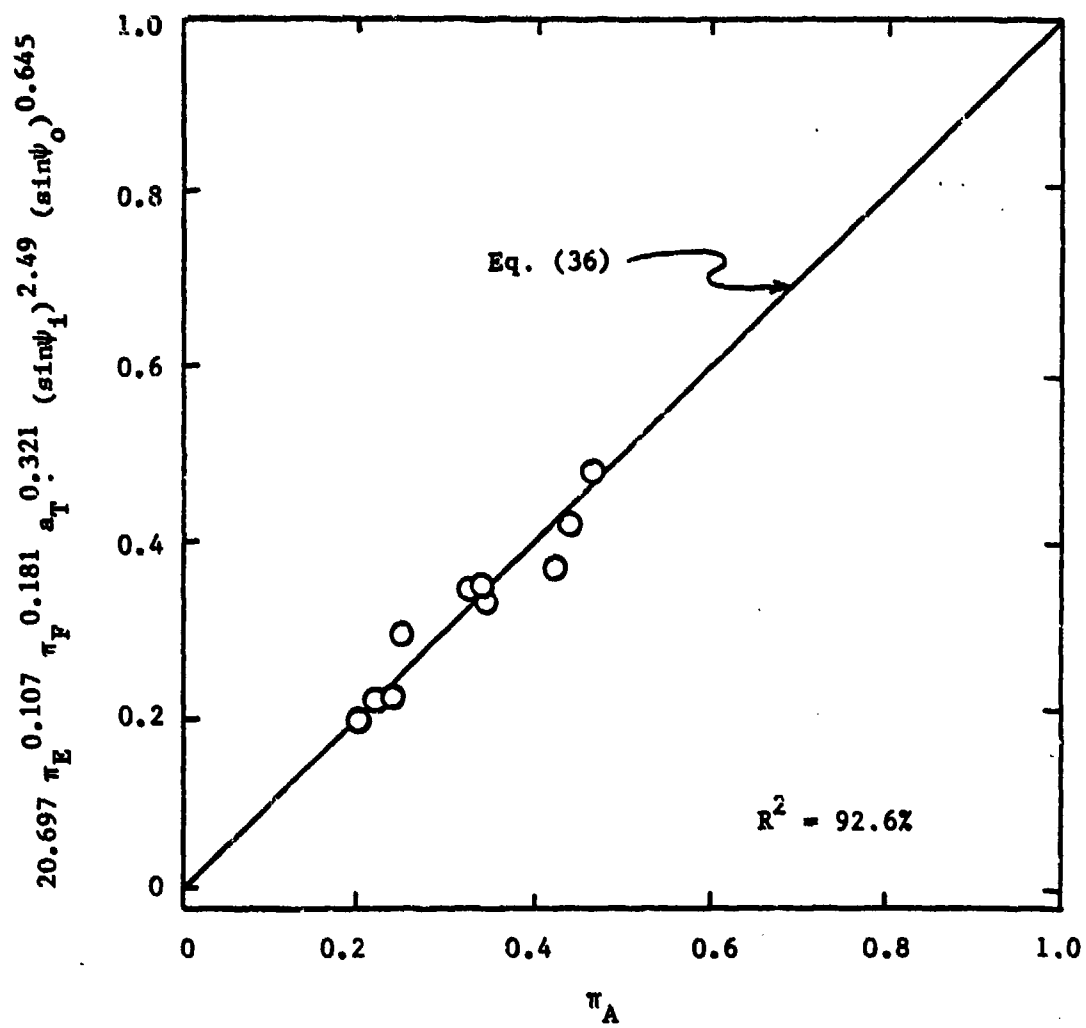


Fig. 49. Data Correlation for the Extended Crack Length π_A

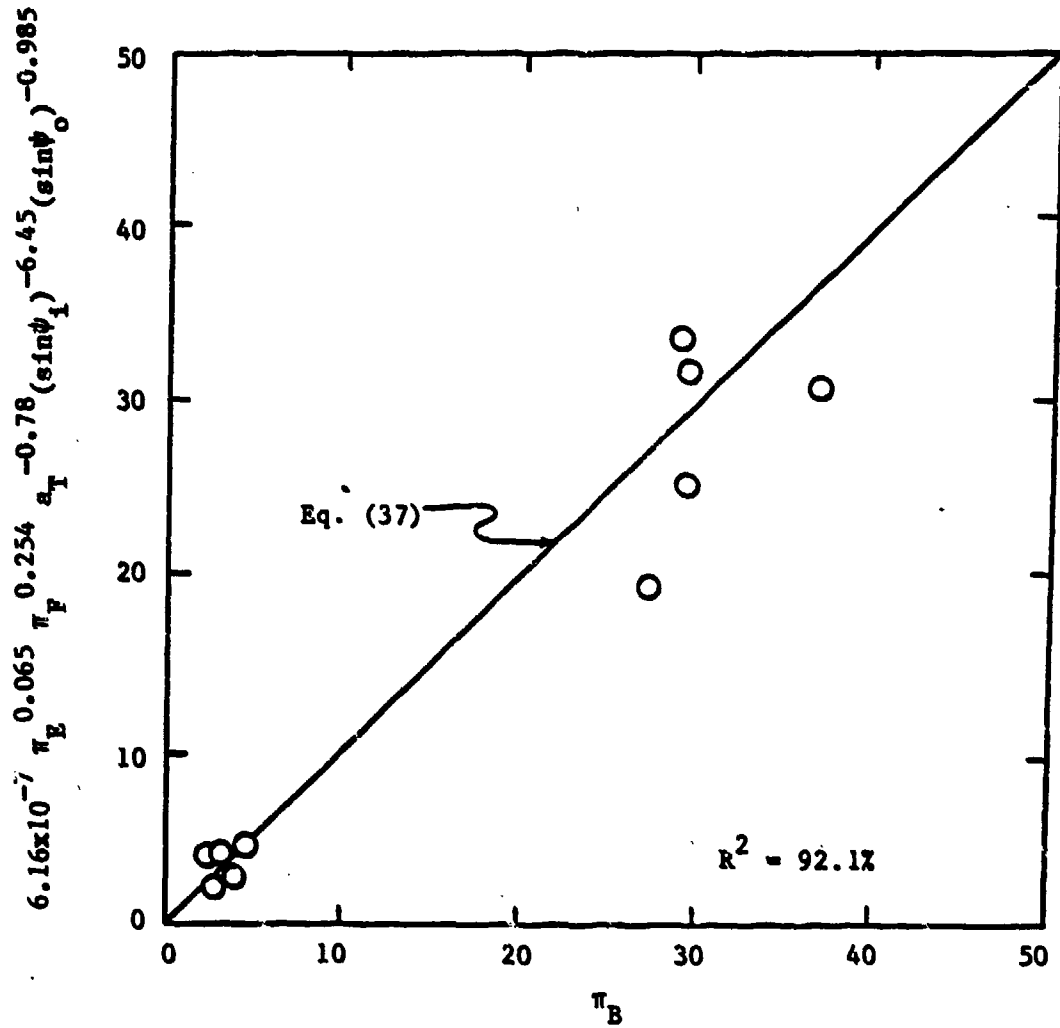


Fig. 50. Data Correlation for the Rate of Increase in Specific Surface Area Π_B

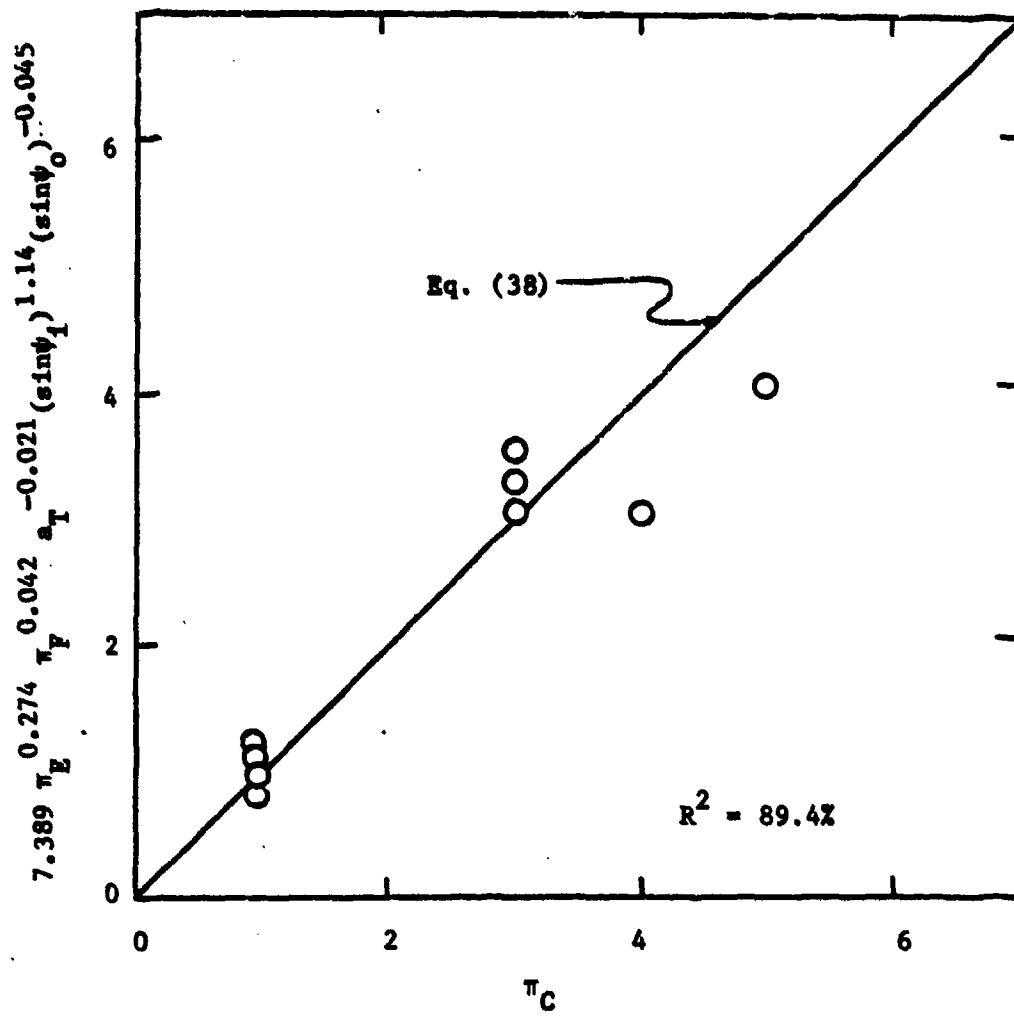


Fig. 51. Data Correlation for the Number of Macrocracks π_C

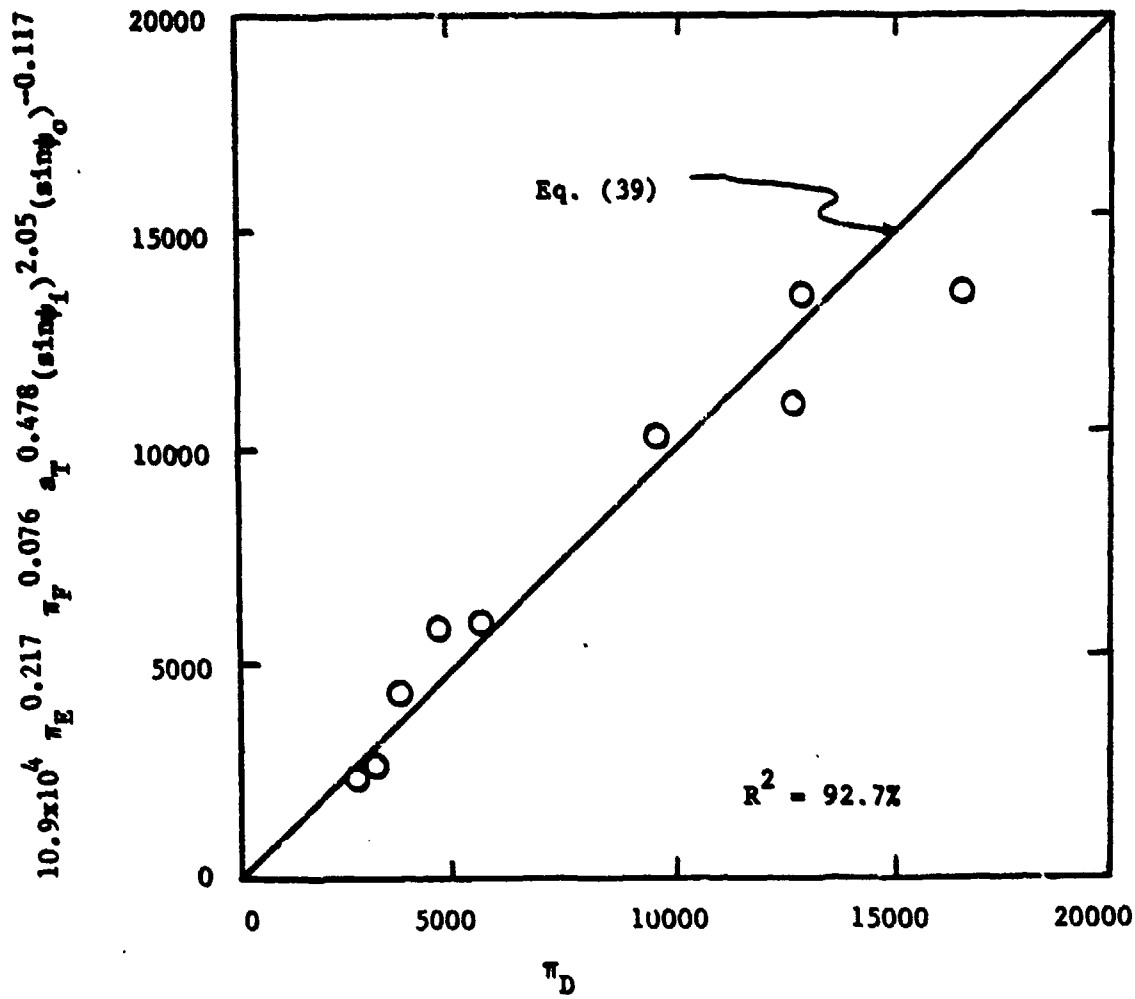


Fig. 52. Data Correlation for the Crack Propagation Velocity Π_D

varying degrees of sample deformation. The equations predict that a greater angle will increase crack growth while each of the other parameters will decrease. Under these conditions the angle at the crack tip is likely to be greater resulting in a higher local stress concentration. Thus, the single crack propagation mode is more probable. With a longer, single crack, equation (3-37) indicates that these two effects contribute to a decrease in π_p . Also, higher sample deformation work implies less energy is available to propagate the crack, reducing V_p .

The effects of initial propellant temperature on the crack propagation process can be very important. At lower temperatures (higher values of a_T) the propellant becomes more brittle, lowering its fracture energy. Higher crack velocities and longer cracks are expected. However, the range of initial temperatures in this study was limited by the test conditions. Broader ranges are needed to more accurately predict its effect. ψ_1 was essentially unchanged in these tests but was included for the completeness of the correlations.

The agreement of these predictions with previous observations and basic principles in fracture mechanics indicates that the methodology for their development is valid. Similar correlations for different propellant types with different crack configurations could be developed using this method to determine guidelines for the safe operation of high performance rocket motors.

3.5 SUMMARY AND CONCLUSIONS

Two types of composite propellants were selected for this study (ARC 5051 and ARC 4525). They have similar composition but different oxidizer particle sizes and mechanical properties. Several tests were conducted under different loading conditions and sample geometries. The damage to the sample was measured in terms of crack length, number of cracks and crack propagation velocity. Using a dimensional analysis of the key variables involved in the crack propagation phenomena, a set of governing dimensionless parameters were established. These parameters can provide some insight into the cause and effect relationship between the momentum and energy input to a propellant sample with existing flaws and the resultant damage.

Correlations of the dimensionless parameters were obtained by performing a multiple regression analysis on the test data. The driving parameters, π_E and π_F have positive relationships with the damage parameters π_A , π_B , π_C and π_D . This indicates that higher momentum and energy inputs to the crack cavity will cause a greater degree of damage. The geometry and initial temperature of the propellant sample have additional effects characterized by the correlations. These correlations are only valid for the small ranges of temperature and crack cavity angles studied, however, additional tests could expand the applicability and validity of this method. Enough data has been obtained to predict the strong dependence on the rate of energy input and pressurization on crack propagation. The good agreement with test data and reasonable physical interpretation

suggests that the methodology outlined in this study can provide a basis for future development of similar correlations defining safe operating conditions for solid propellant rockets.

Future research in this area should include:

- a) development of correlations for high-energy propellants used in actual propulsion systems today, including high-elongation propellants;
- b) extension of the present analysis to include propagation and flame spreading along a motor casing due to an initially debonded area, and;
- c) integration of a crack/debond model into the Rocket Performance Prediction Code.

REFERENCES

1. McCarty, K. P., Isom, K. B., and Jacox, J. L., "Nitramine Propellant Combustion," AIAA Paper 79-1132, AIAA/SAE/ASME 15th Joint Propulsion Conference, June 18-20, 1979, Las Vegas, Nevada.
2. Kubota, N., Takizuka, M., and Fukuda, T., "Combustion of Nitramine Composite Propellants," AIAA Paper 81-1582, AIAA/SAE/ASME 17th Joint Propulsion Conference, July 27-29, 1981, Colorado Springs, Colorado.
3. Kubota, N., "Combustion Mechanisms of Nitramine Composite Propellants," Eighteenth Symposium (Int.) on Combustion, The Combustion Institute, pp. 195-206, 1981.
4. Kuwashara, T. and Kubota, N., "Combustion of RDX/AP Composite Propellants at Low Pressure," AIAA Paper 82-1114, AIAA/SAE/ASME 18th Joint Propulsion Conference, June 21-23, 1982, Cleveland, Ohio.
5. Kubota, N., "Physicochemical Processes of HMX Propellant Combustion," 19th Symposium (Int.) on Combustion, The Combustion Institute, pp. 777-785, 1982.
6. Kubota, N. and Okuhara, H., "Burning Rate Temperature Sensitivity of HMX Propellants," AIAA Paper 86-1593, AIAA/ASME/SAE/ASEE 22nd Joint Propulsion Conference, June 16-18, 1986, Huntsville, Alabama.
7. Cohe-Nir, E., "Combustion Characteristics of Advanced Nitramine-Based Propellants," Eighteenth Symposium (Int.) on Combustion, The Combustion Institute, pp. 195-206, 1981.
8. BenReuven, M., Caveny, L. H., Vichnevetsky, R. J., and Summerfield, M., "Flame Zone and Sub-Surface Reaction Model for Deflagrating RDX," Sixteenth Symposium (Int.) on Combustion, The Combustion Institute, pp. 1223-1233, 1976.
9. BenReuven, M. and Caveny, L. H., "Nitramine Flame Chemistry and Deflagration Interpreted in Terms of a Flame Model," AIAA Paper 79-1133, AIAA/SAE/ASME 15th Joint Propulsion Conference, June 18-20, 1979, Las Vegas, Nevada.
10. Ben-Reuven, M. and Summerfield, M., "Combustion of Nitramine Propellants," Contract Report ARBRL-CR-00507, March 1983.
11. Cohen, N. S., Lo, G. A., and Crowley, J. C., "Model and Chemistry of HMX Combustion," AIAA Paper 83-1195, AIAA/SAE/ASEE 19th Joint Propulsion Conference, June 27-29, Seattle, Washington.
12. Kim, J. U., Torikai, T., and Kuo, K. K., "Comparison of Ignition Characteristics of a Series of RDX-based Composite Propellants Under Rapid Pressurization," AIAA Paper 85-1175, AIAA/SAE/ASME/ASEE 21st Joint Propulsion Conference, Monterey, California, July 8-10, 1985.

13. Roller, C., Strauss, B., Downs, D. S., and Varney, M., "Development of OXITE - A Strand Igniter Material for LOVA Propellants," 22nd JANNAF Combustion Meeting, CPIA Publication 432, Vol. II, Oct., pp. 377-390, 1985.
14. Ohlemiller, T. J. and Summerfield, M., "A Critical Analysis of Arc Image Ignition of Solid Propellants," *AIAA Journal*, Vol. 6, May 1968, pp. 878-886.
15. Ohlemiller, T. J. and Summerfield, M., "Radiative Ignition of Polymeric Material in Oxygen/Nitrogen Mixture," Thirteenth Symposium (Int.) Combustion, 1971, pp.1087-1094.
16. Ohlemiller, T. J., Caveny, L. H., DeLuca, L., and Summerfield, M., "Dynamic Effects on Ignitability Limits of Solid Propellants Subjected to Radiative Heating," Fourteenth Symposium (Int.) on Combustion, The Combustion Institute, pp. 1297-1307, 1973.
17. DeLuca, L., Ohlemiller, T. J., Caveny, L.H., and Summerfield, M., "Radiative Ignition of Double Base Propellants: II. Pre-Ignition Events and Source Effects," *AIAA Journal*, Vol. 14, No. 8, Aug. 1976, pp.1111-1117.
18. DeLuca, L., Caveny, L. H., Ohlemiller, T. J., and Summerfield, M., "Radiative Ignition of Double base Propellants: I. Some Formulation Effects," *AIAA Journal*, Vol. 14, No. 7, July 1976, pp.940-946.
19. Price, E. W., Bradley, H. H. Jr., Dehority, G. L., and Ibiricu, M. M., "Theory of Ignition of Solid Propellants," *AIAA Journal*, Vol. 4, No. 7, July 1966, pp. 1153-1181.
20. Kulkarni, A. K., Kumar, M., and Kuo, K. K., "Review of Solid Propellant Ignition Studies," AIAA Paper 80-120, June 1980.
21. Hermance, C. E., "Solid-Propellant Ignition Theories and Experiments," Chapter 5 in *Progress in Astronautics and Aeronautics: Fundamentals of Solid-Propellant Combustion*, edited by K. K. Kuo and M. Summerfield, AIAA, 1984, Vol. 90, pp. 239-304.
22. Shannon, L. J., "Composite Solid-Propellant Ignition by Radiant Energy," *AIAA Journal*, Vol.8, No.2, Feb. 1970, pp.346-353.
23. Kashiwagi, T., "Experimental Observation of Radiative Ignition Mechanism," *Combustion and Flame*, Vol. 34, 1979, pp.231-244.
24. Kashiwagi, T., "Effects of Attenuation of Radiation on Surface Temperature for Radiative Ignition," *Combustion Science and Technology*, Vol. 20, 1979, pp.225-234.
25. Kashiwagi, T., "Effects of Sample Orientation on Radiative Ignition," *Combustion and Flame*, Vol.44, 1982, pp.223-245.

26. Kashiwagi, T. and Ohlemiller, T. J., "A Study of Oxygen Effects on Nonflaming Transient Gasification of PMMA and PE During Thermal Irradiation," Nineteenth Symposium (Int.) on Combustion, The Combustion Institute, pp.815-823, 1982.
27. Kashiwagi, T., Ohlemiller, T. J., and Kashiwagi, T., "Ignition Mechanism of a Liquid Fuel by High Intensity Radiation," AIAA Paper 81-0180, AIAA 19th Aerospace Sciences Meeting, Jan. 12-15, 1981, St. Louis, Missouri.
28. Saito, T., Maruyama, T., Higashi, K., and Iwama, A., "Ignition of Laminated Composite Propellants Composed of Ammonium Perchlorate Single Crystal and Fuel-Binder Slab by Means of CO₂ Laser," *Combustion Science and Technology*, Vol.15, 1977, pp.161-168.
29. Harayama, M., Saito, T., and Iwama, A., "Ignition of Composite Solid Propellant at Subatmospheric Pressure," *Combustion and Flame*, Vol.52, 1983, pp.81-89.
30. Mutoh, N., Hirano, T., and Akita, K., "Experimental Study on Radiative Ignition of Polymethylmethacrylate," 17th Symposium (Int.) on Combustion, The Combustion Institute, pp. 1183-1190, 1977.
31. Ostrowski, P. P., Dabora, E. K., and Downs, D. S., "Laser Ignition of Black Powder," 16th JANNAF Combustion Meeting, Sep., 1978, pp.499-513.
32. Ostrowski, P.P., Grant, J. F., and Downs, D. S., "Laser Ignition Characteristics of M-26 Gun Propellant," 17th JANNAF Combustion Meeting, CPIA Publication 329, Vol. II, Nov. 1980, pp.55-61.
33. Beckel, S. A. and Matthews, R. D., "Ignition of Polyoxymethylene," *Combustion and Flame*, Vol.57, 1984, pp.71-86.
34. Kashiwagi, T., "A Radiative Ignition Model of a Solid Fuel," *Combustion Science and Technology*, Vol.8, 1974, pp. 225-236.
35. Kumar, R. K. and Hermence, C. E., "Role of Gasphase Reactions During Radiant Ignition of Solid Propellants," *Combustion Science and Technology*, Vol.14, 1976, pp. 169-175.
36. Kumar R. K., "Gas Phase Ignition of a Composite Solid Propellant Subjected to Radiant Heating," *Combustion Science and Technology*, Vol.30, 1983, pp. 273-288.
37. Phuoc, T. X. and Durbetaki, P., "Radiative Ignition of Polymethylmethacrylate," 1985 Fall Technical Meeting, Eastern Section of Combustion Institute, Nov. 4-6, 1985, Philadelphia, Pennsylvania.

38. Kindelan, M. and Williams, F. A., "Gas-Phase Ignition of a Solid with In-Depth Absorption of Radiation," *Combustion Science and Technology*, Vol.16, 1977, pp. 47-58.
39. Baumann, G. C., Cheung, W. Y., and Harris, L. E., "CARS Spectroscopy of the Reaction Zone of Nitramine Propellants," Proceedings of 16th Annual Conference, Fraunhofer-Institute for Propellants and Explosives (ICT), V27, July 2-5, 1985.
40. Harris, L. E., "CARS Spectroscopy of the Reaction Zone of Methane-Nitrous Oxides and RDX Propellant Flames," ARAED-TR-85007, January, 1986.
41. Parr, T. and Hanson-Parr, D., "Species and Temperature Profiles in Ignition and Deflagration of HMX," Spring Meeting, Western State Section, The Combustion Institute, April 6-7, 1987, Provo, Utah.
42. Isom, K. B., Caldwell, D. J., and Greene, F. T., "Pyrolysis of Nitramine Propellants II - Kinetic Experiments," 18th JANNAF Combustion Meeting, CPIA Publication 308, 1979, pp. 514-540.
43. Schroeder, M. A., "Critical Analysis of Nitramine Decomposition Data: Some Comments on Chemical Mechanism," Proceedings of the 16th JANNAF Combustion Meeting, Sept. 1979, Vol. II, pp. 13-34.
44. Schroeder, M. A., "Critical Analysis of Nitramine Decomposition Data: Activation Energies and Frequency Factors for HMX and RDX Decomposition," Proceedings of the 17th JANNAF Combustion Meeting, CPIA Publication 329, Vol. II, Sept. 1980, pp. 493-508.
45. Schroeder, M. A., "Critical Analysis of Nitramine Decomposition Data: Product Distributions for HMX and RDX Decomposition," Proceedings of the 18th JANNAF Combustion Meeting, CPIA Publ. 347, Vol. II, Oct. 1981, pp. 395-423.
46. Schroeder, M. A., "Critical Analysis of Nitramine Decomposition Data: Some Preliminary Comments on Autoacceleration and Autoinhibition on HMX and RDX Decomposition," Proceedings of the 19th JANNAF Combustion Meeting, Oct. 1982.
47. Schroeder, M. A., "Critical Analysis of Nitramine Decomposition Data: Activation Energies and Frequency Factors for HMX and RDX Decomposition," BRL-TR-2673, Sept. 1985.
48. Boggs, T. L., "The Thermal Behavior of Cyclotrimethylenetrinitramine (RDX) and Cyclotetramethylenetetranitramine (HMX)," in *Progress in Astronautics and Aeronautics: Fundamentals of Solid-Propellant Combustion*, edited by K. K. Kuo and M. Summerfield, AIAA, 1984, Vol. 90, pp. 121-175.
49. Fifer, R. A., "Chemistry of Nitrate Ester and Nitramine Propellants," in *Progress in Astronautics and Aeronautics: Fundamentals of Solid-Propellant*

Combustion, edited by K. K. Kuo and M. Summerfield, AIAA, 1984, Vol. 90, pp. 177-237.

50. Kraeutle, K. J., "A Contribution to the Knowledge of HMX Decomposition and Application of Results," Proceedings of the 17th JANNAF Combustion Meeting, CPIA Publication 329, Vol. II, Nov. 1980.
51. Kraeutle, K. J., "Thermal Decomposition of HMX: Effect of Experimental Conditions and of Additives," Proceedings of the 18th JANNAF Combustion Meeting, CPIA Publication 347, Vol. II, Oct. 1981.
52. Kraeutle, K. J., "The Differential Thermal Analysis of HMX at Atmospheric and Subatmospheric Pressure," Proceedings of the 19th JANNAF Combustion Meeting, 1982.
53. Kimura, J. and Kubota, N., "Thermal Decomposition Process of HMX," *Propellants and Explosives*, 5, 1980, pp. 1-8.
54. Maruzumi, H., Fukuma, D., Shiota, K., and Kubota, N., "Thermal Decomposition of RDX Composite Propellants," *Propellants, Explosives, Pyrotechnics*, 7, 1982, pp. 40-45.
55. Fifer, R. A., "Cage Effects in the Thermal Decomposition of Nitramines and Other Energetic Materials," Proceedings of the 19th JANNAF Combustion Meeting, Oct. 6-7, 1982.
56. Karpowicz, R. J., Gelfand, L. S., and Brill, T. B., "Application of Solid-Phase Transition Kinetics to the Properties of HMX," *AIAA Journal*, Vol. 21, Jan. 1983, pp. 310-312.
57. Dubovitskii, F. I. and Korsunskii, B. L. "Kinetics of the Thermal Decomposition of N-Nitro-Compound," *Russian Chemical Reviews*, Vol. 50, No. 10, 1981, pp. 958-978.
58. Shaw, R. and Walker, F. E., "Estimated Kinetics and Thermochemistry of Some Initial Unimolecular Reactions on the Thermal Decomposition of 1,3,5,7-Tetranitro-1,3,5,7-Tetraazacyclooctane in the Gas Phase," *Journal of Physical Chemistry*, Vol. 81, No. 25, 1977, pp. 2572-2576.
59. Farber, M. and Srivastava, R. D., "Mass Spectrometric Studies of the Thermal Decomposition of 1,3,5,7-Tetranitro-1,3,5,7-Tetraazacyclooctane (HMX)," *Chemical Physics Letters*, Vol. 80, No. 2, June 1981, pp. 345-349.
60. Farber, M. and Srivastava, R. D., "Mass Spectrometric Investigation of the Thermal Decomposition of RDX," *Chemical Physics Letters*, Vol. 64, No. 2, July 1979, pp. 307-310.
61. Suryanarayana, B., Graybush, R. J., and Auiera, J. R., "Thermal Degradation of Secondary Nitramines: A Nitrogen-15 Tracer Study of HMX (1,3,5,7-Tetranitro-1,3,5,7-tetraazacyclooctane)," *Chemistry and Industry (London)*, Vol. 52, 1967, pp. 2177-2178.

62. Kumar, M. and Kuo, K. K., "Ignition of Solid Propellant Crack Tip Under Rapid pressurization," AIAA Journal, Vol. 18, No. 7, July 1980, pp. 825-833.
63. Knauss, W. G., "On the Steady Propagation of a Crack in a Viscoelastic Sheet: Experiments and Analysis," Deformation and Fracture of High Polymers, edited by H. H. Kausch, J. A. Hassel and R. I. Jaffee, Plenum Press, 1974.
64. Schapery, R. A., "A Theory in Crack Initiation and Growth in Viscoelastic Media, I. Theoretical Development," Int. J. Fracture, Vol. 11, Feb. 1975, pp. 141-159.
65. Schapery, R. A., "A Theory in Crack Initiation and Growth in Viscoelastic Media, II. Approximate Methods of Analysis," Int. J. Fracture, Vol. 11, June 1975, pp. 369-388.
66. Schapery, R. A., "A Theory in Crack Initiation and Growth in Viscoelastic Media, III. Analysis of continuous Growth," Int. J. Fracture, Vol. 11, Aug. 1975, pp. 549-562.
67. Siefert, J. G. and Kuo, K. K., "Crack Propagation in Burning Solid Propellants," Dynamics of Shock Waves, Explosions and Detonations, edited by J. R. Bowen, N. Manson, A. K. Oppenheim and R. I. Soloukhin, Vol. 94 of Progress in Astronautics and Aeronautics, 1985, pp. 575-595.
68. Kuo, K. K. and Moreci, J. A., "Crack Combustion and Branching in Burning Solid Propellants," 21st International Combustion Symposium, 1987.
69. Kuo, K. K., Moreci, J. A. and Mantzaras, J., "Diferent Modes of Crack Propagation in Burning Solid Propellants," J. Propulsion and Power, vol. 3, no. 1, Jan.-Feb 1987, pp. 19-25.
70. Gent, A. N. and Marteny, P., "The Effect of Strain upon the Velocity of Sound and the Velocity of Free Retraction for Natural Rubber," ONR Technical Report No. 16, University of Akron, 1982.
71. De Luca, L., "Extinction Theories and Experiments," AIAA Progress Series, Vol. 90, edited by K. K. Kuo and M. Summerfield, 1984.
72. Kuo, K. K., Moreci, J. A., Kim, J. U., Torikai, T., Grubelich, M., Chang, L. K. and Beelitz, P., "Crack Propagation and Branching in Burning Solid Propellants and Ignition of Nitramine-Based Composite Propellants," Annual Report to Office of Naval research Power Program, Jan. 1986, 114 pages.
73. Harbert, B. C. and Schapery, R. A., "Some Mechanical Properties of Two HTPB Composite Solid Propellants," Report No. MM 5222-86-20, Texas A&M University, 1986.
74. Mueller, H. K. and Knauss, W. G., "Crack Propagation in a Linearly Viscoelastic Strip," J. Applied Mechanics, June 1971, pp. 141-158.

75. Schapery, R. A., "Fracture Mechanics of Solid Propellants," Fracture Mechanics, edited by N. Perrone, H. Liebowitz, D. Mulville and W. Pilkey, U. Press of Va., 1978, pp. 387-398.
76. Langlois, G. and Gonard, R., "New Law for Crack Propagation in Solid Propellant Material," J. Spacecraft, Vol. 16, No. 6, Nov.-Dec. 1979, pp. 357-360.
77. Krier, H., "Solid Propellant Burning Rate During a Pressure Transient," Combustion Science and Technology, Vol. 5, 1972, pp. 69-73.
78. Cornelisse, J. W., Schoyer, H. F. R. and Walker, K. F., Rocket Propulsion and Spaceflight Dynamics, The Pitman Publishing Co., London, 1979, pp.174-179.
79. White, F. M., Fluid Mechanics, 2nd edition, McGraw-Hill Book Co., 1986, pp. 253-259.
80. Kumar, M., Kovacic, S. M. and Kuo, K. K., "Gas Penetration, Flame Propagation, and Combustion Processes in Solid Propellant Cracks," AIAA-80-1206, July 1980
81. Velikanov, M. A., Measurement Errors and Empirical Relations, Israel Program for Scientific Translations Ltd., 1965, pp. 172-177.

Appendix A

MEASUREMENT OF CO₂ LASER ENERGY FLUXES

It is very important to define the energy fluxes delivered by the incident laser beam for ignition studies. In order to define the CO₂ laser energy fluxes, it is necessary to measure the laser intensity distribution precisely. In this study, three different devices were used for the measurement of energy fluxes; a thin film heat flux gage, a fine wire thermocouple and a pyroelectric sensor. Each device has its own advantages and disadvantages in the measurement of laser energy flux. In this appendix, the three energy flux measurement techniques using the three devices will be discussed. The method which employed a fine wire thermocouple was found to be most convenient and reliable.

A thin film heat flux gage was tried first among the three devices to measure the incident energy. Since the sensing area of the thin film heat flux gage was too large to measure the distributions of energy fluxes, a mask with a small hole ($\phi 1.0mm$) was used to block the incident laser beam except the portion which passes through a hole which has a predetermined diameter on the mask. An anodized aluminum mask block (1"x1"x3/4") was mounted on a Medtherm Rh-Pt heat flux gage. Fig. A1 shows the assembly of the mask block and the thin film heat flux gage. The assembly is mounted on a positioning bed to scan the energy intensity distribution. Calibration is necessary to obtain heat flux values from the output of the heat flux gage. However, no absolute calibration was attempted, since not all the incident laser is absorbed by the gage due to nonunity of the surface absorptivity. Only relative energy flux distribution was measured. One way to estimate absolute energy flux distribution is through the integration of the relative profile and redistribution of the total incident energy. The total energy of incident laser beam was measured

by a laser power probe. This value is proportionally distributed depending on the local relative intensities.

Another technique used to measure the laser beam intensity profile was using fine wire thermocouple. A fine wire thermocouple ($\phi 25\mu m$) was installed as shown in Fig. A2. In order to minimize the effects of reflected beam, a thin stainless deflector was placed under the thermocouple. A distance should be kept between the thermocouple and the deflector to prevent the effect of hot plume generated from the deflector due to laser heating. Energy fluxes were deduced from the temperature profile measured by the thermocouple. As in the thin film sensor technique, a positioning table was used to scan the beam profile with the thermocouple. Figure A3 shows the intensity profile of the CO₂ laser beam.

The last method employed in this study for measurement of incident laser energy flux is using a pyroelectric sensor. The schematic diagram Fig. A4 shows the setup using a pyroelectric sensor to measure beam intensity distribution. A PZT(lead zirconate titanate) sensor was mounted on a support which was attached on a positioning table. The PZT sensor is directed to the direction parallel to the incoming laser beam. The rise time was 10 ns with 50 ohm resistor. The responsivity was $1.5 \mu a/W$ and the capacitance of the sensor was 250 pf. Additional two 100 $K\Omega$ were used to increase sensitivity. The resistance was 75 $K\Omega$ and the output sensitivity was 75 mV/W . A chopper is required to measure intensity for a longer duration than the rise time which is about 100 μs .

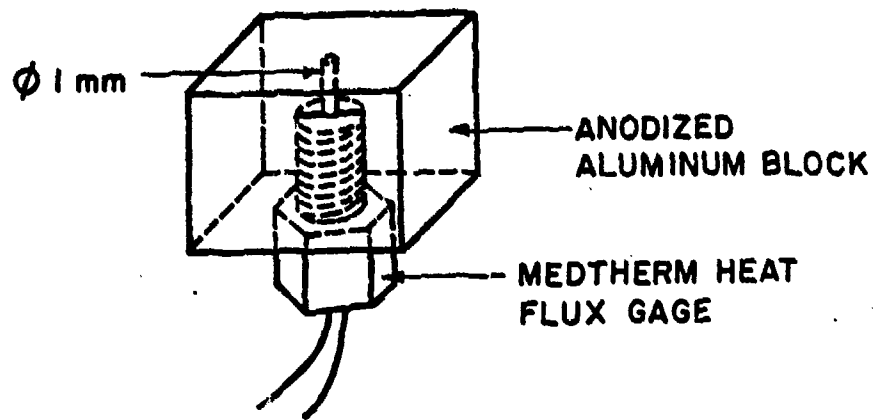


Fig. A1 Assembly of Heat Flux Gage

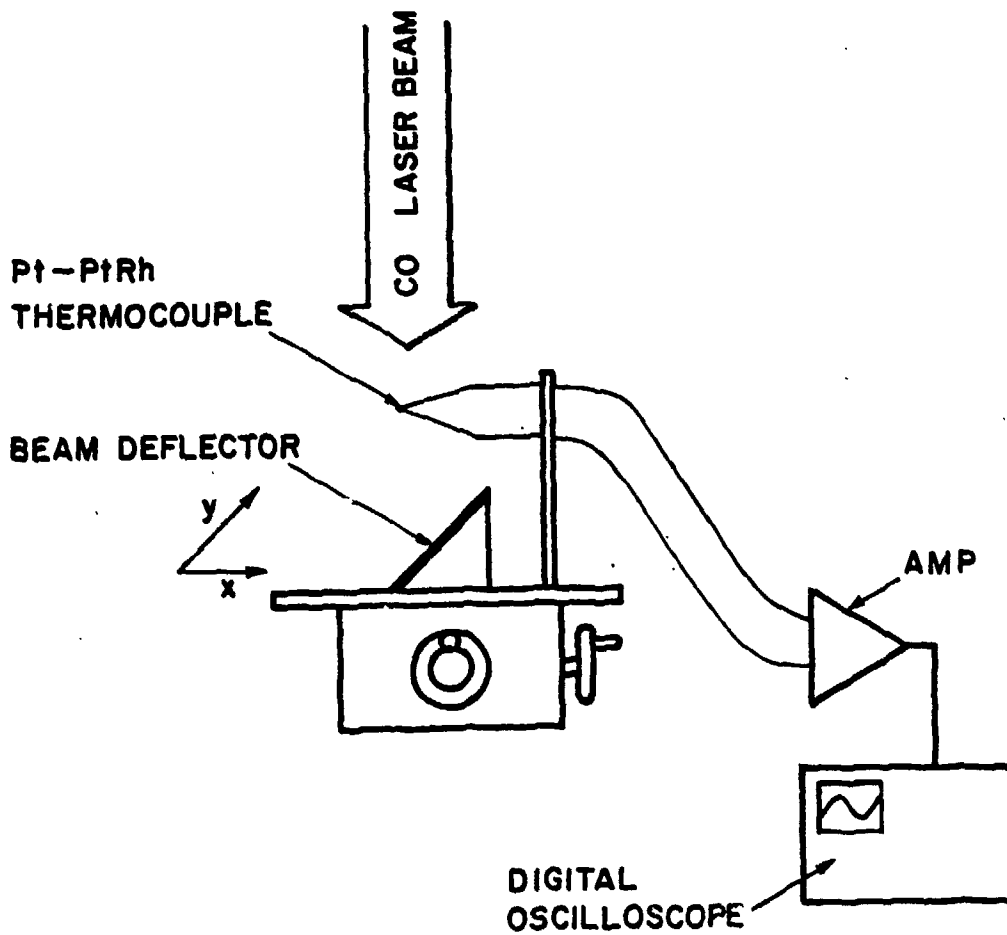


Fig. A2 Intensity Measurement by Fine Wire Thermocouple

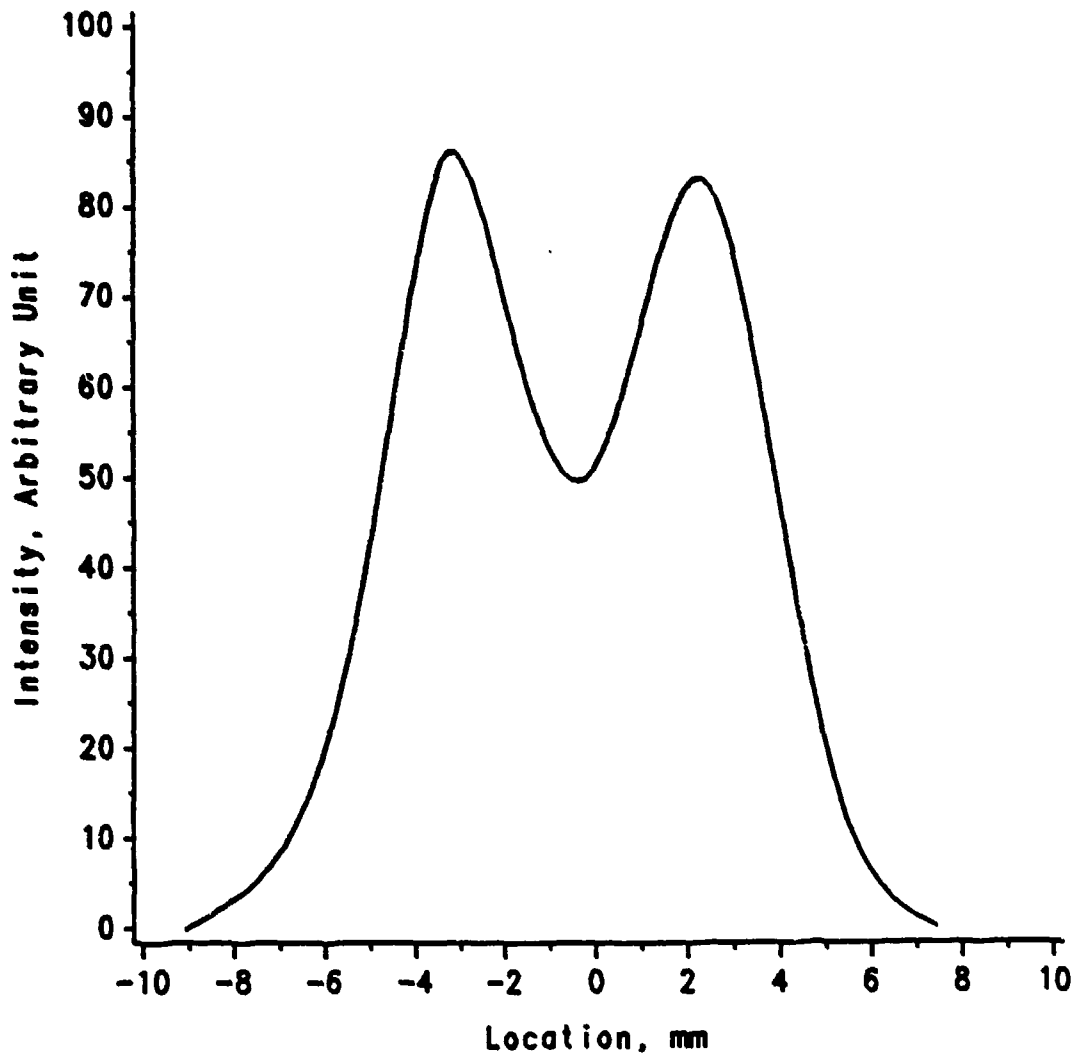


Fig. A3 Laser Beam Intensity Distribution

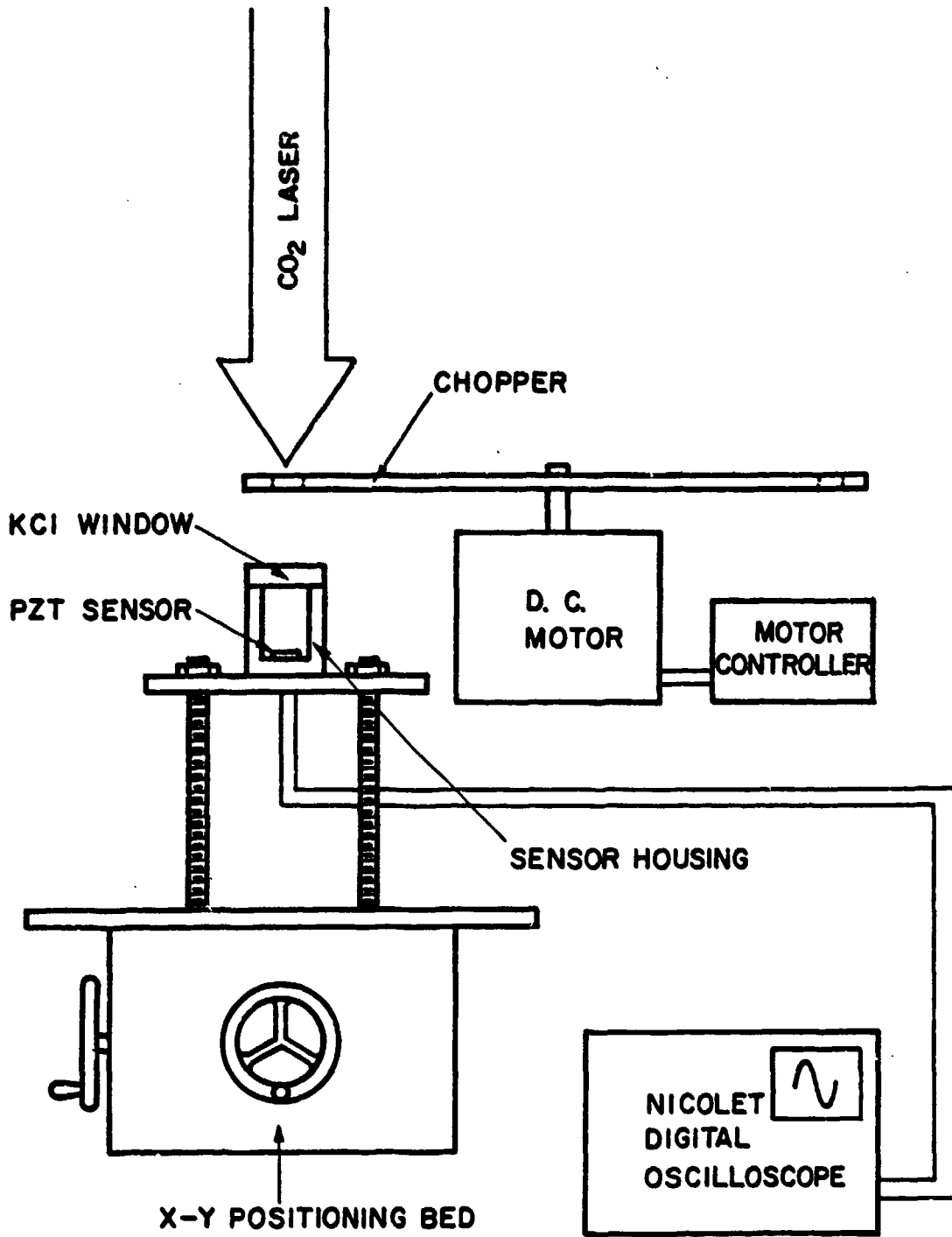


Fig. A4 Schematic Diagram of Pyroelectric Sensor Measurements

Appendix B

DIFFERENT TECHNIQUES USED FOR ACHIEVING BEAM UNIFORMITY

Uniformity of beam intensity is one of the most important properties of laser beam when the laser beam is used as a energy source for ignition study. However, due to the inherent structure of the laser, the intensity of laser beams are generally not uniform. Unless the laser beam intensity is spatially uniform, the energy flux can not be defined with a single value.

Many different techniques were discussed to uniformize the intensity of laser beams which were originally nonuniform[A1]. Some of the uniformizing techniques are from solar energy research. A Kaleidoscope was considered as the most promising device.

The operation and construction of kaleidoscopes were discussed extensively by Ohlemiller and Summerfield[A1]. In this appendix, only brief description on the principle of kaleidoscopes will be presented. Kaleidoscope is a square channel consisting of four parallel reflecting surfaces. Expanding laser beam which enters the kaleidoscope will be reflected off of the inner walls at the given angle of incidence and continue through the channel. Since the inner walls of the kaleidoscope are parallel, the angle of incidence is unchanged as the beam proceeds through the channel. Thus, the kaleidoscope breaks expanding beam entering it and recombines the segments of the beam at the exit of the kaleidoscope. Figure A5 shows the schematic diagram of the Kaleidoscope. The CO₂ laser beam is focused and diverges entering a square mirror channel. Some part of the laser beam reflects from the inner mirror surface two or three times, while the center portion of the incoming beam does not experience any reflections due to small angles from the center of the beam. The beam emerging out of the channel, which is composed of many

different beam segments, is recombined by a reimaging lens. Figure A5 also shows the pattern of CO₂ laser beam at different locations after the Kaleidoscope. Due to the coherence of laser beams, a strong interference appears on the output pattern. Thus, it is necessary to uniformize the beams further by using vibrating or rotating mirrors which average the interfered beam patterns timewise.

Another device used to achieve a uniform laser beam is a mask. As discussed in Appendix I, the intensity distribution of the laser used in this study is not a totally Gaussian. The pattern was closer to TEM₁₀. The intensity at the center of the beam was lower than those of surrounding locations. To invert this profile, a stainless mask (125 μm thick) with a hole (φ5mm) was placed on the laser beam path. Due to the converging effect of the mask, the original intensity distribution became quite uniform in the area of a circle of radius 4mm from the center. Figure 6 shows the intensity distribution of the CO₂ laser beam uniformized using a mask. Figure A6 shows the intensity distribution of the laser beam when the beam mask was used. Figure A7 shows one cross-sectional distribution of the laser intensity. Since the radius of the sample was about 4mm, the intensity of the laser directed on sample surface became uniform with a variation of 10%.

REFERENCES

- A1. Ohlemiller, T. J. and Summerfield, M., "Radiative Ignition of Polymeric Fuels in an Oxidizing Gas," AFOSR Contract Report No. AFOSR 69-2147TR, August 1969.

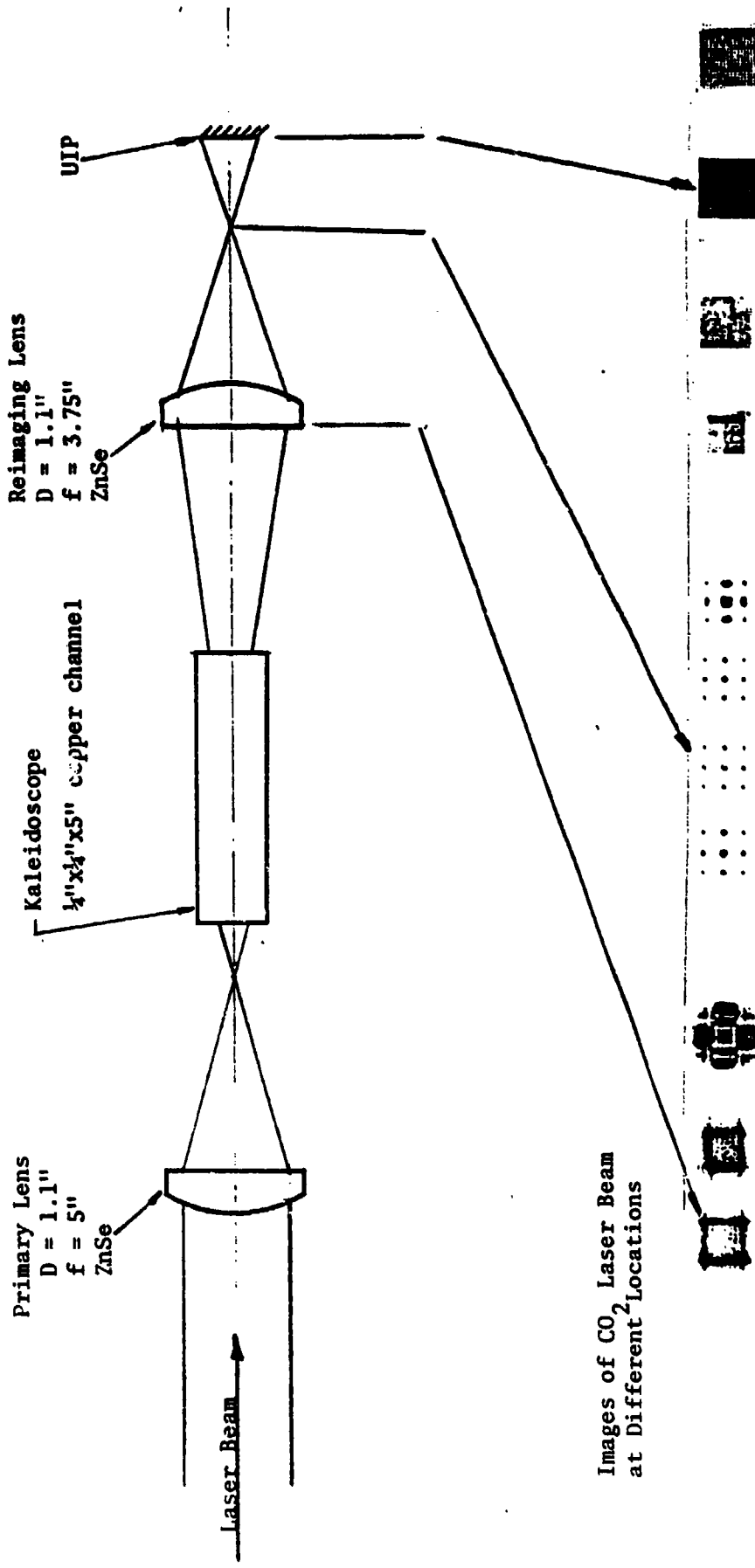


Fig. A5 Schematic Diagram of Kaleidoscope

LASER INTENSITY DISTRIBUTION

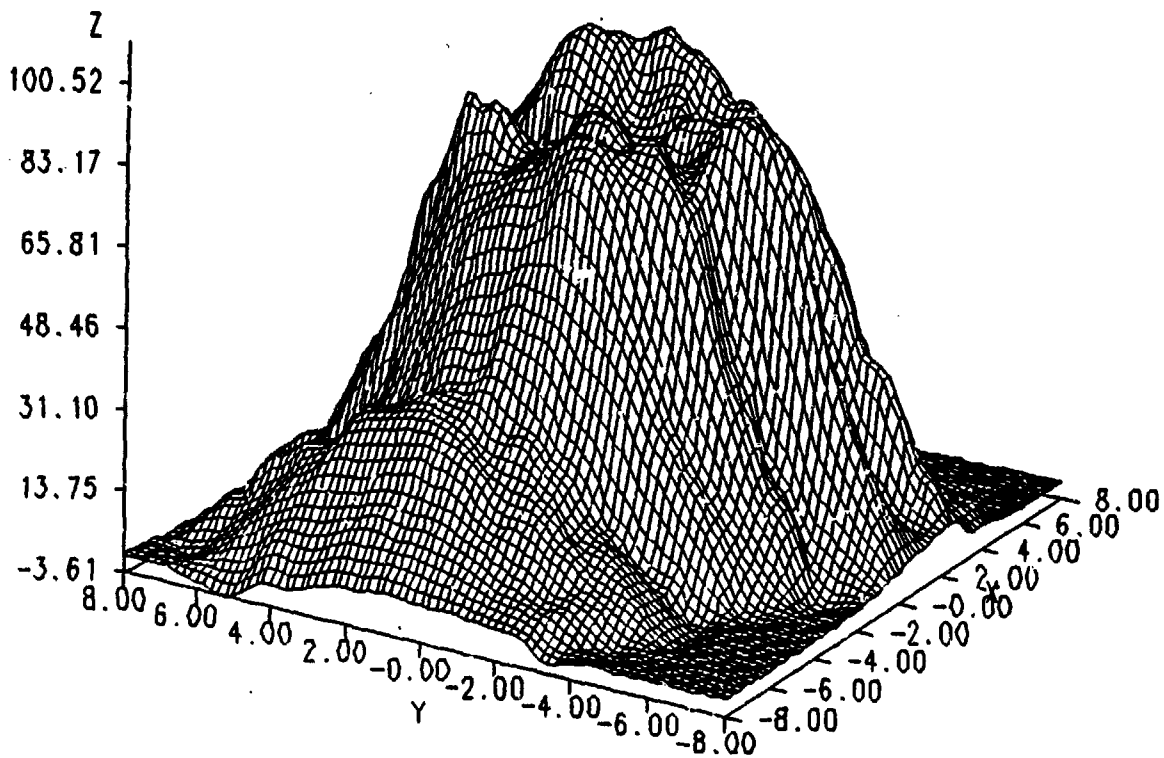


Fig. A6 Modified Intensity Distribution by Beam Mask

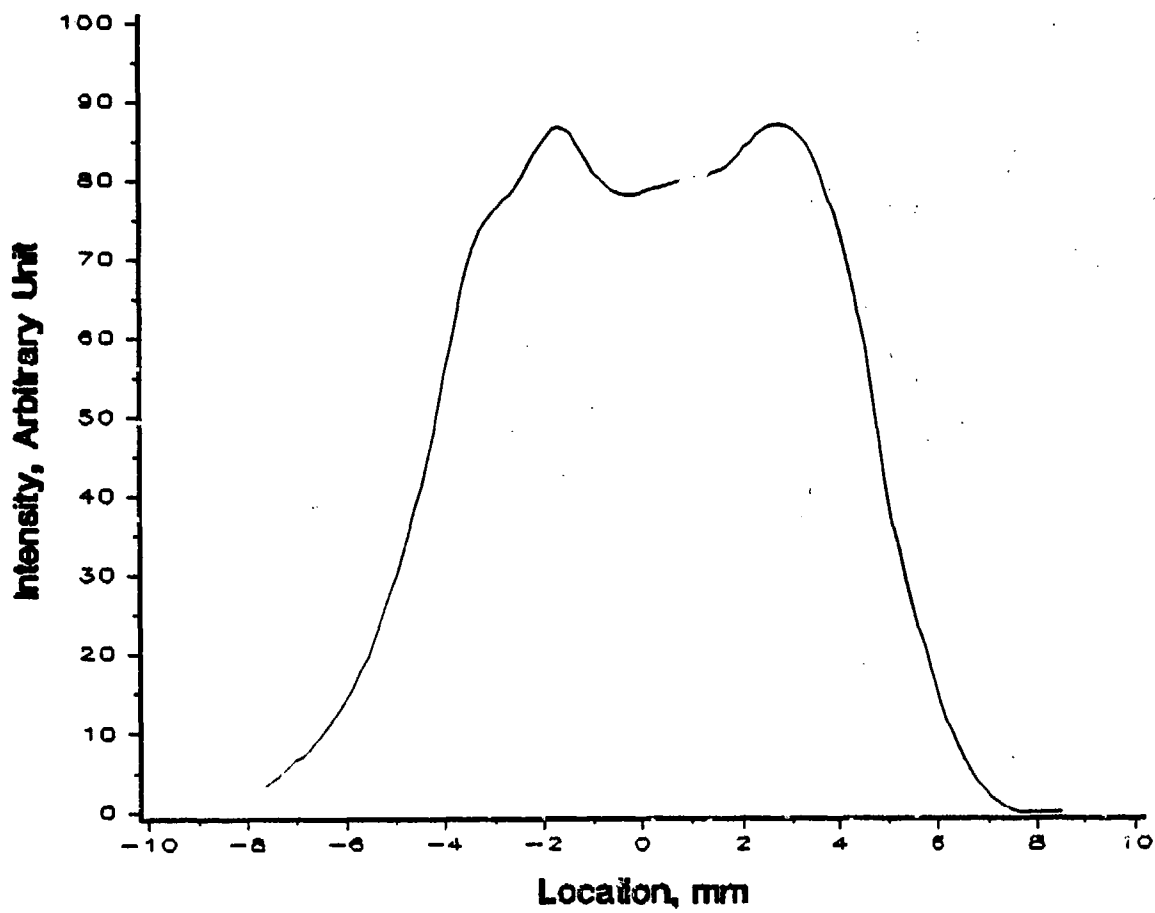


Fig. A7 A Cross-Sectional Distribution of the Modified Beam

Appendix C

ABSORPTION OF CO₂ LASER BEAM ENERGY BY CO₂ GAS

The problems related to the absorption of the CO₂ laser beam energy by the combustion product gases were addressed by Kashiwagi[24] in his ignition study of PMMA and red oak. Edwards et al.[A2] studied the band absorption characteristics of CO₂ gas for a range of wave lengths. The study shows the existence of a major absorption band near 10.4 μm . As the temperature of the gas increases, the width of the absorption band is widened so that the absorptance at 10.6 μm is significantly increased. The absorption band of H₂O near 10.6 μm shows a significant amount of the CO₂ laser energy can be absorbed by H₂O vapor.

In order to investigate the CO₂ laser absorption by CO₂ gas, an attenuation test chamber was designed (Fig. A8). A cylindrical plexiglass tubing (ID=2", OD=2.5", L=variable) was placed between two aluminum closures. KCl windows were mounted on the two closures, one on the top and the other on the bottom of the chamber. The length of the test chamber can be varied using different plexiglass tubing with different length. Since the O-ring grooves are on the aluminum closures, no machining on the plexiglass tubing is necessary.

Figure A9 shows the attenuation of the CO₂ laser beam intensity by CO₂ gas present in the path of the beam. At atmospheric pressure the attenuation increased monotonously between 0% to 60% of CO₂ concentration. As the CO₂ concentration increases further, the slope of the curve becomes less steep. As approaching 80% of CO₂ gas concentration, the attenuation reaches a limit value.

The attenuation results show a significant amount of the incident laser beam is absorbed by the CO₂ gas in the beam path. One of the main absorption bands of CO₂ gas is at 10.4 μm . Since the wave length of the CO₂ laser is at 10.6 μm ,

a substantial portion of the laser beam can be absorbed if the absorption band is widened at elevated temperatures. Water vapor is known to be one of the absorber of the CO₂ laser. However, absorption data for water vapor was scarce. The absorption test with water vapor has not been carried out in this study. Further studies are necessary for absorption of CO₂ laser by other gases as well as water vapor.

REFERENCES

- A2. Edwards, D. K., "Molecular Gas Band Radiation," *Advances in Heat Transfer*, Edited by T. F. Irvine, Jr. and J. P. Hartnett, Vol. 12, Academic Press, N.Y., 1976, pp.156-193.

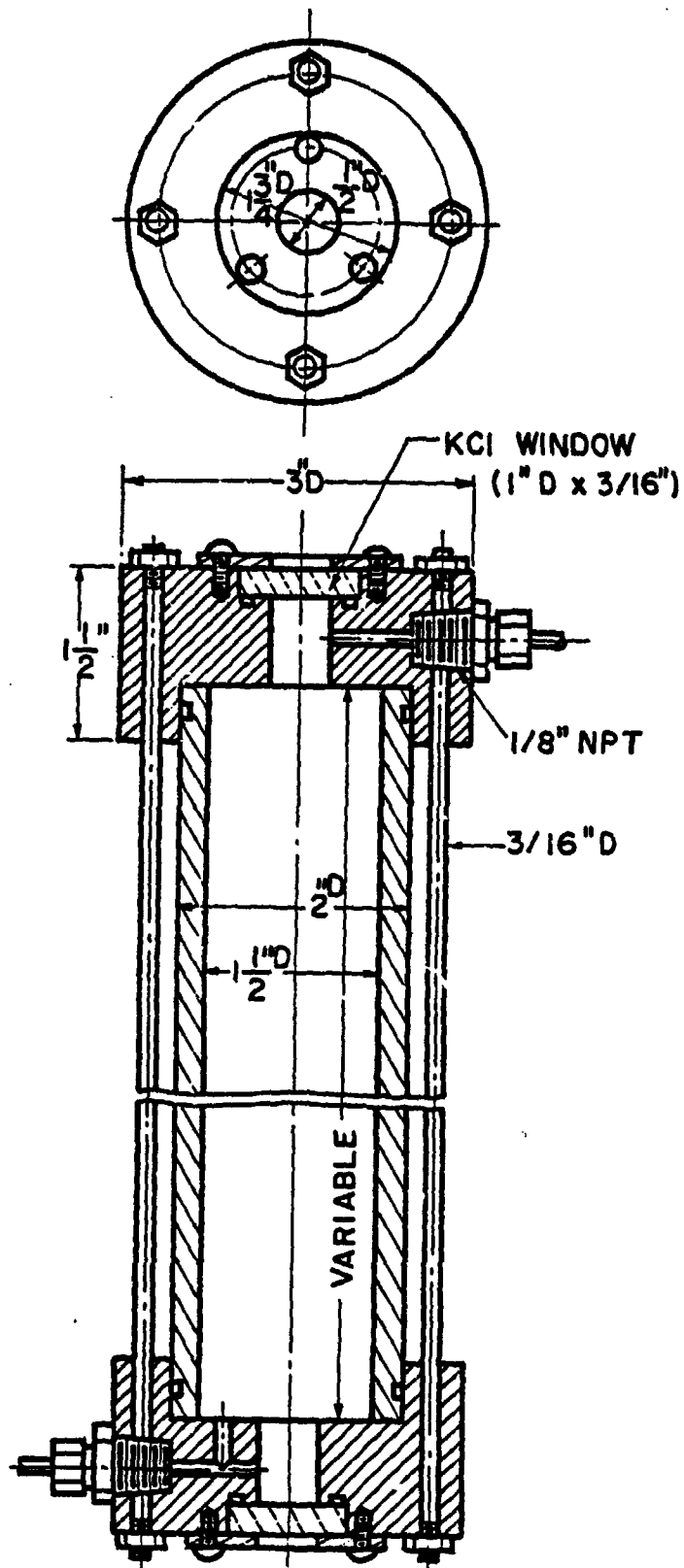


Fig. A8 Beam Attenuation Test Chamber

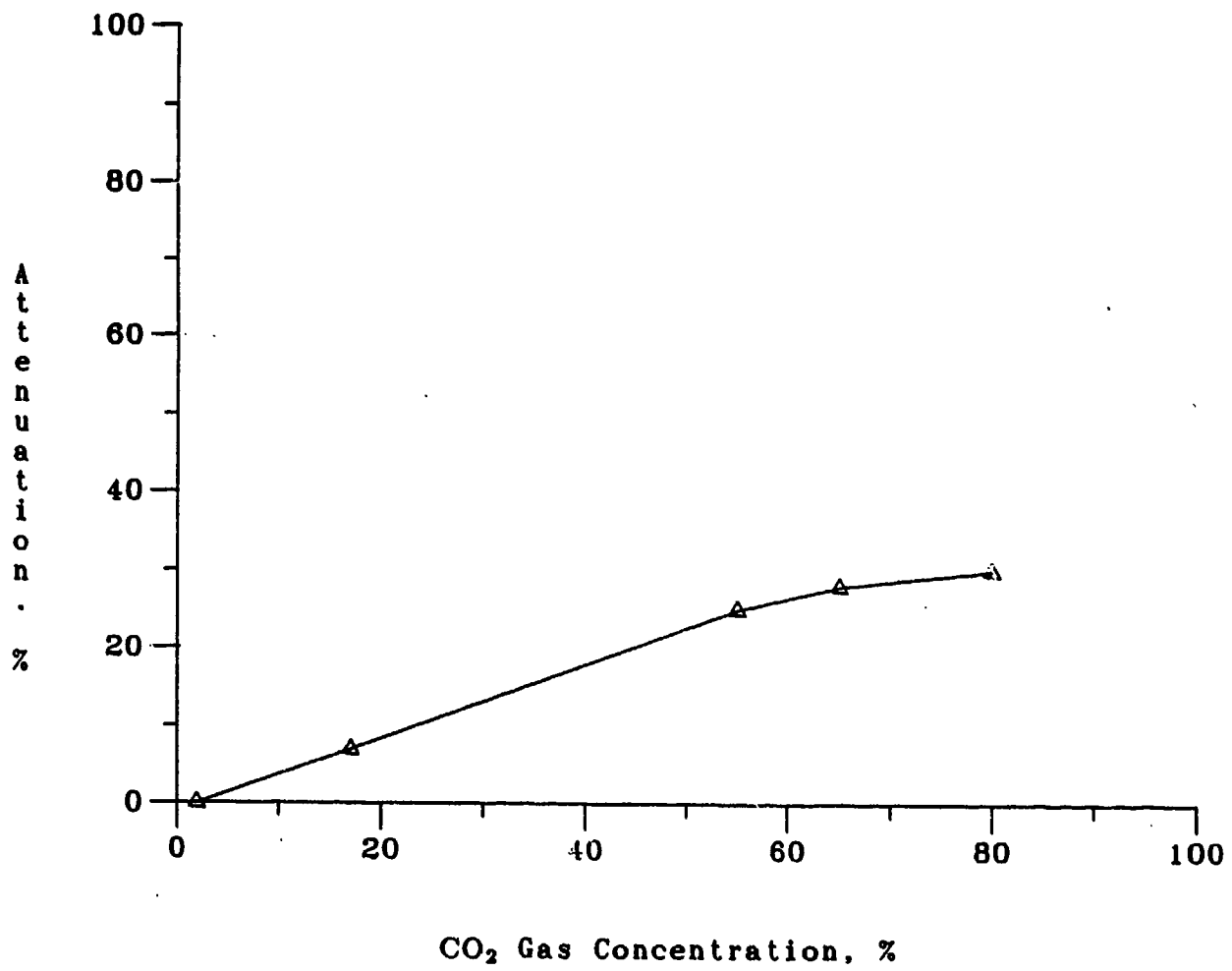


Fig. A9 Attenuation of CO₂ Laser Beam Intensity by CO₂ Gas

APPENDIX D

CO₂ LASER OPERATING PROCEDURE

1. Set the chiller temperature at 15° C and turn on the chiller power. Make sure that the water outlet valve is fully open. Check the water level of the chiller through the opening on the top of the chiller. If the water level is lower than 1 inch from the top, refill it with *distilled* water. Do not use the tap water.
2. Turn on the warning light switch located on the wall behind the CO₂ laser. Check if the red warning light above the entrance door is blinking.
3. Unlock the breaker box (if locked) on the wall behind the CO₂ laser and turn on the CO₂ laser power switch.
4. Open the CO₂ laser mix bottle, record the pressure on the log book, and set the regulator to 10 psi.
5. Turn on the exhaust fan (the switch of the fan is located on the wall beside the door of the test cell).
6. Turn on the power of the interlocking system. If the interlocking system is to be defeated, turn on the interlocking defeat switch on the box.
7. Make sure that all the sliding glass windows on the laser are properly closed.
8. Check the chiller water temperature on the dial gauge on the chiller. If the temperature is higher than 15° C, wait for a few more minutes until it reaches 15° C.
9. Turn on the power meter which is located under the laser control panel.
10. Set the right knob on the mode control of the laser control panel to *CW*.

11. Set the left knob on the mode control to *OFF*.
12. Set the knob on the current control to halfway between 0 and 50 mA.
13. Set the left keyswitch to *ON* position.
14. Turn on the laser by pushing the black pushbutton switch. Note that the orange laser lamp on the front of the laser is lit.
15. Adjust the purge rate using the purge rate control knob to maintain the tube pressure at 19-20 torr.
16. Set the left knob on the mode control to *ON*.
17. Set the current control knob to 50 mA and check the anode voltage at 15 KV by depressing the tube drive switch to voltage.
18. The reading on the power meter should be about 800 Watts. If the power is lower than 790 Watts, adjust the mirrors inside the laser following the alignment procedure described elsewhere (See Alignment Procedure).
19. Recycling mode can be used to save the laser mixture gas. Follow the recycling procedure to use the recycling mode (See Recycling Procedure).
20. Select the laser power level by adjusting the current using the current control knob. Do not try to use a power level lower than 100 Watts, since at a lower level the laser becomes unstable.
21. If a long operation is required, use the cooling system for the external optics (See Water Cooling Procedure).

Gate Control Mode

22. The gate mode is used to control the laser generating time period. To use the gate mode control, set the left knob on the mode control to *GATE* position.
23. Select the desired laser generating time by setting the gate control time in the combination of the gate control knobs. (For example, set the left knob to 100 and the right knob to 4, then the gate control time is $100 \times 4 = 400$ ms.)

Continuous Wave Operation

24. In order to use the laser beam in continuous wave in either the manual control mode or the gate control mode, set the right knob on the mode control to *CW*. For the manual control, set the left knob on the mode control panel to *ON* position. Now the laser is on. To send the laser beam out of the laser, follow the procedure from item 26.

Pulsed Mode

25. To use the pulsed mode, set the right knob on the mode control to either *SP* for single pulse or *REP* for repeated pulse.
26. Select the desired frequency and pulse length by setting the frequency and pulse length knobs on the pulse control panel in the same way as for the gate control. For the single pulse, it is not necessary to set the knobs.

Shutter Control

27. To send out the laser beam, set the keyswitch to the shutter power *ON* position.
28. Turn on the shutter power by depressing the red button.

29. Set the shutter control toggle switch to the *OPEN* position. Now, the laser beam is delivered out of the laser.
30. For the gate control, turn on the switch on the power supply box, and turn it off.

Shut-Down Procedure

31. After the use of the laser beam, set the shutter control toggle switch to the closed position. Then, turn off the keyswitch for the shutter power.
32. Set the left knob on the mode control panel to the *OFF* position. Set the right knob on the mode control panel to the *CW* position.
33. Turn off the laser by depressing the red pushbutton switch on the laser power panel. Set the power keyswitch the *OFF* position.
34. Turn off the cooling water to the external optics (if it was being used).
35. Turn off the chiller.
36. Record time and the bottle pressure in the log book.
37. Close the main valve to the gas bottle of the laser mix. Release the regulator valve.
38. Shut off the CO₂ laser power switch. Turn off the warning light switch.
39. Turn off the exhaust fan and the interlocking switch.

I, _____, have read and understood the above operating procedure as well as the safety precautions in the CO₂ laser manual.

Signature

Date

The above person is authorized to operate the CO₂ laser.

Prof. K. K. Kuo

Date

cc: Mr. John Raiser, Mech. Engr.

Mr. Robert Houtz, College of Engr.

Mr. H. O. Triebold, Jr., Mgr., Safety Division.

APPENDIX E

SPECIFICATIONS OF EQUIPMENT USED IN LASER IGNITION STUDY

• Laser

- Model Super48 CO₂ Laser, 800 Watt in continuous wave, 3500 Watt in pulsed mode.
 - . Coherent, 3210 Porter Drive, Palo Alto, CA 94304, (415) 493-2111.

• Thermal Image Plate

- Thermal Image Plate and Ultraviolet Lamp.
 - . Optical Engineering, Inc., P.O.Box 696, Coffey Lane, Santa Rosa, CA 95402, (707) 528-1060.

• Laser Power Probe

- Model P-20Y and P-1000Y Laser Power Probe.
 - . Optical Engineering, Inc., P.O.Box 696, Coffey Lane, Santa Rosa, CA 95402, (707) 528-1060.

• Mirrors and Lenses

- 3" Silicon Mirrors with Enhanced Silver Coating.
- 1.1" dia. Plano-Convex Lenses with AR Coating.
 - . Two-Six Incorporated, Saxonburg Boulevard, Saxonburg, PA 16056, (412) 352-1504.
 - . Laser Optics, Inc., P.O.Box 127, Danbury, Connecticut 06810, (203) 744-4160.

• Windows

- 3" Zinc Selenide(ZnSe) Window with AR Coating.
 - . Two-Six Incorporated, Saxonburg Boulevard, Saxonburg, PA 16056, (412) 352-1504.
- 1/2" KCl Window for Low Pressure Chamber.
 - . Harshaw Chemical Co., 6801 Cochran Road, Solon, Ohio, 44139, (216) 248-7400.

• Optic Mounts

- Model LP-1 Five Axis Gimbal Optic Mounts
 - . Newport Corporation, 18235 Mt. Baldy Circle, Fountain Valley, CA 92708, (714) 963-9811.
- Dovetail Optical Track and Slides.
 - . Thomas Tool and Die, Inc., 8805 Bradley Avenue, Sun Valley, CA 91352, (818) 767-6511.

- Stereoscopic Microscope
- Unitron ZST with Fiber Optic Ring Illuminator.
 - . Unitron Inc., 175 Express Street, Plainview, N.Y., 11803, (516) 822-4601.

- Photodiode
- Model SGD-040L Fast Response Silicon Photodiode.
 - . EG&G Photon Devices, 35 Congress Street, P.O.Box 5006, Salem, MA 01970-6526, (617) 745-3200.

- Pyroelectric Detector
- Lead Zirconate Titanate (PZT) Laser Pulse Detector.
 - . Barnes Engineering Co., 30 Commerce Road, Stamford, Connecticut 06904, (203) 348-5381.

- Thermocouples
- 25 μ m Pt-Pt13%Rh Fine Wire Thermocouple.
 - . Omega Engineering, Inc., P.O.Box 2669, Stamford, CT 06906, (203) 359-1660.
- 5 μ m Pt-Pt10%Rh Wollaston Process Wires.
 - . Sigmund Cohn Corp., 121 S. Columbus Avenue, Mount Vernon, NY 10553, (214) 664-5300.
- Model TCF302-Rh-Pt-M Thin Film Thermocouple.
 - . Medtherm Corporation, P.O.Box 412, Huntsville, Alabamb, 35804, (205) 837-2000.

- Digital Oscilloscope
- Nicolet Series 2090 Oscilloscope.
 - . Nicolet Instrument Corporation, 5225-2 Verona Road, Madison, Wisconsin 53711, (608) 271-3883.

- High Speed Movie Camera
- HYCAM 16mm High Speed Movie Camera, Model 41-0006.
 - . Redlake Corp., 15005 Concord Circle, Morgan Hill, CA 95037, (408) 779-6464.

- High Speed Video Camera
- Spin Physics High-Speed Motion Analyzer.
 - . Spin Physics Division, Eastman Kodak Co., 3099 Science Park Rd., San Diego, CA 92121, (619) 481-8182.

- Videograph Printer
- AIDI Videograph Printer CT1500.
 - . Advanced Imaging Devices, Inc., 875 Mande Avenue, Mountain View, CA 94943.

- Video System

- Panasonic PK-956 Video Camera
- Panasonic PV-5500 Video Cassette Recorder
 - . Panasonic Co., One Panasonic Way, Secaucus, New Jersey 07094, (201) 348-7000.

- Microcomputer

- IBM-PC.
 - . International Business Machines Corporation, P.O.Box 1328-S, Boca Raton, FL 33432.

- Schlieren System

- Light Source(100W Tungsten-Halogen Lamp 28-8472)
- Condensor Lens(D=18mm, f=40mm Achromat)
- Source Spatial Filter(Rectangular Aperture 23-1928)
- Focussing Lens(D=40mm, f=90mm Achromat)
 - . Ealing Electro-Optics Inc., 22 Pleasant St., South Natick, MA 01760, (617)651-8100.
- Zeiss-Type Optical V-Bench(F83-008)
- Transverse and Vertical Slides(22-4899) and Base(22-4170)
- 60mm Pin Carriers (F60-796)
- Mounting Pins(F41-229)
- Screen Holder(22-8700)
- Rectangular Ground Glass(F42-785)
 - . Edmund Scientific Co., 101 E. Gloucester Pike, Barrington, N.J. 08007, (609) 547-3488.

- Gas Control System

- High Pressure Tubings, Valves, and Connectors.
 - . High Pressure Equipment Company, Inc., 1222 Linden Avenue, Erie, PA 16505, (814) 838-2028.

- Compressor

- Single-End Compressor.
 - . Newport Scientific, Inc., 8246-E Sandy Court, Jessup, MD 20794-0189, (301) 498-6700.

- Vacuum Pump

- Model KC-3 Kinney Vacuum Pump.
 - . Kinney Vacuum Company, 495 Turnpike Street, Canton, MA 02021, (617) 828-9500.

- Pressure Regulator

- Matheson Model 3060 Series High Pressure Regulators.
 - . Matheson Gas Products, P.O.Box 1587, Secaucus, N.J. 07094.

- Gas Chromatograph

- Varian 3700 Gas Chromatograph.
 - . Varian Instrument Group, 25 Hanover Road, Florham Park, N.J. 07932, (201)822-3701.
- Columns and Syringes.
 - . Supelco Park, PA 16323-0048, (814) 359-3441.
- Standard Gases.
 - . Scott Specialty Gases, Route 611, Plumsteadville, PA 18949, (215) 766-8861.
 - . Union Carbide Corporation, Linde Division, National Specialty Gases Office, 100 Davidson Avenue, Somerset, NJ 08873, (201) 271-2600.

- Strobe Light

- Strobotac Model 1531.
 - . General Radio Co., 300 Baker Avenue, Concord, MA 01742, (617) 646-0550.

APPENDIX F

TEST PROCEDURES AND CHECKLIST FOR CRACK PROPAGATION TESTS

A. Igniter Assembly:

- ___ 1. Cut igniter charge and record mass and propellant type.
- ___ 2. Select a primer with a resistance 20 - 50 ohms and record.
- ___ 3. Assemble primer, primer holder and lexane insulator.
- ___ 4. Check primer resistance. If it has changed significantly, check leads and reassemble.
- ___ 5. Place desired amount of propellant shavings in and around the primer.
- ___ 6. Assemble remaining igniter pieces with the yellow marks aligned.
- ___ 7. Check igniter circuit continuity.
- ___ 8. Short igniter leads.

B. Sample preparation:

- ___ 1. Measure and record the mass and dimensions of the sample.
- ___ 2. Paint a dot on the front surface of the propellant for focusing purposes.
- ___ 3. If Spin Physics camera will be used, mark the crack tip location with paint and measure distance between crack tip and focusing dot.

C. Chamber Assembly:

- ___ 1. Install the desired N₂ inlet lines (except on igniter) and check for unobstructed flow.
- ___ 2. Assure sacrificial and main windows properly fit into test chamber and clean window surfaces.

- ___ 3. Spread flame retardant grease over all sample surfaces (except crack surface) and install in test chamber.
- ___ 4. Insure propellant sample will not extend beyond sample holders when compressed.
- ___ 5. Install main O-ring with joined ends at the rear of the chamber. Apply permatex to O-ring and groove .
- ___ 6. Install sacrificial window against the propellant sample.
- ___ 7. Install the main window into the chamber window cover.
- ___ 8. Bolt the chamber window assembly to the main chamber, being careful to evenly compress the sample.
- ___ 9. Measure and record top bursting diaphragm thickness and install diaphragm and hood assembly to top of chamber. Check for proper alignment of diaphragm holder to allow maximum flow area.
- ___ 10. Check side rupture disk and replace if necessary.
- ___ 11. Install igniter assembly to bottom of chamber being sure to align the yellow marks. Check igniter resistance and short the igniter circuit.
- ___ 12. Connect N₂ line to igniter. If not used, ensure that igniter ports are plugged.

D. Instrumentation:

- ___ 1. Verify that all ignition circuits are in the off position.
- ___ 2. Install pressure transducers and record their respective locations, sensitivities, and data lines.
- ___ 3. Connect water lines and check for leaks. Turn off water supply.
- ___ 4. Set up Hycam and install dummy film. Insure the film speed is reduced for ignition circuit test.

- ___ 5. Connect volt-meter to ignition box and run ignition test.
- ___ 6. Check focus of the Hycam.
- ___ 7. Load new film, depress microswitch, and insure triggering arm operates properly as the camera door is secured. Reset PPS dial.
- ___ 8. Check and record all camera settings.
- ___ 9. Record test cell temperature.
- ___ 10. Setup and focus Spin Physics camera (if used).
- ___ 11. Remove lights used for focusing.
- ___ 12. Install exhaust fan and connect to Lights No. 1 receptacle.
- ___ 13. Check data line connections to charge amplifiers.
- ___ 14. Set input voltages and calibrate charge amplifiers.
- ___ 15. Connect charge amplifier output to Physical Data recorder and record settings. Turn on Physical Data unit and hit reset button.

E. Test firing procedure:

- 1. Perform final check of all connections.

- | | |
|-------------------|--------------------------|
| ___ Hycam | ___ Spin Physics |
| ___ Transducers | ___ Water connections |
| ___ Exhaust fan | ___ N ₂ lines |
| ___ Physical Data | ___ Charge Amps |

- ___ 2. Open outside door.
- ___ 3. Secure safety key.
- ___ 4. Connect igniter leads to igniter box.
- ___ 5. Check igniter resistance.
- ___ 6. Close and secure test cell door.
- ___ 7. Turn on warning light and sound test alarm.

- ___ 8. Verify charge amps are in CHARGE position.
- ___ 9. Turn on igniter power and charge capacitor.
- ___ 10. Turn on ignition panel switches 3 thru 6 and event switch.
- ___ 11. Turn off safety switch.
- ___ 12. Unground charge amplifiers, reset Physical Data recorder.
- ___ 13. Turn on Spin Physics Camera and wait for ready light.
- ___ 14. Turn on ignition switch.
- ___ 15. After rupture disk bursts, inject N_2 .
- ___ 16. When propellant has stopped burning, stop Spin Physics camera.

F. Post Firing Procedures:

- ___ 2. Ground charge amplifiers.
- ___ 3. Turn off all ignition switches and turn on exhaust fan switch.
- ___ 4. Make a hard copy of pressure traces on X-Y plotter.
- ___ 5. Transfer pressure data to Nicolet and store on floppy disk.
- ___ 6. Generate calibration signals for transducers and record on X-Y plotter.

DATA SHEET FOR CRACK PROPAGATION EXPERIMENTS

CRACK PROPAGATION TEST NO. _____

DATE _____

Participants: _____

TEMPERATURE: T(room) _____ C T(cell) _____ C

CRACK GEOMETRY AND SAMPLE SPEC.:

IGNITER:

Propellant type _____

Primer _____

Configuration _____

Propellant type _____

Length _____

Dimensions _____

Max gap width _____

Mass _____

Inner taper angle _____

Resistance _____

Taper height _____

Thickness _____

FLYING PIN IGNITER:

Weight _____

Primer resistance _____

Fuse Wire Location _____

Propellant weight _____

Propellant type _____

CAMERA:

Diaphragm thickness _____

Type of Lens _____

Diaphragm diameter _____

Framing Rate _____ Frames/s

Diaphragm material _____

Optical Head: 1/4 , 1/2 , frame

PPS Dial _____

RUPTURE DISK ACTUATOR:

Multiplier _____

Primer resistance _____

Time Marker _____ Pulses/s

Propellant weight _____

Remote firing at _____ ft

Propellant type _____

Distance of focus _____ ft

Brake Dial _____

FILM:

Servo _____

ASA No. _____

H/L speed reducer _____

Length _____

F. Stop: _____

Color _____, B & W _____

APPENDIX G
ERROR ANALYSIS

In the multiple regression of the data in Table VI, the exponential relationships assumed for the dimensionless parameters [equations (3-36) through (3-39)] were rearranged into a linear relationship based on the natural logarithm of each value. Using the basic properties of logarithmic representations, the uncertainty in each dimensionless quantity can be expressed as

$$\ln(x_i) = \ln(x) + e_x/x \quad (G-41)$$

where x_i is the actual value, x is the measured value and e_x is the error interval associated with that measurement.⁸¹ The method of least square analysis used on the measured data will give more accurate results when

$$\ln(x) \gg e_x/x \quad (G-42)$$

An expression for the relative error in each dimensionless parameter is

$$r_x = e_x/(x \ln(x)) \quad (G-43)$$

Table VII contains estimations of the various errors involved in measuring each of the variables in the experimental setup. Equation (G-43) can then be evaluated for each of the dimensionless parameters. This equation indicates that for values of x which approach unity, the relative error could be significant. Since the error of c (n) is assumed to be zero, its correlation is not affected. However, a_T does have a finite error associated with it. For the worst case of

$a_T = 1.1$, $r_x = 0.095$ or 9.5% relative error. This could be improved by referencing a_T to a temperature outside the normal operating range.

Using equation (G-43) and the values listed in Table 4, the relative error was calculated for each dimensionless parameter based on its average value.

$$A = L_D/a_o \quad (G-44)$$

Assume $e_{L_D} \ll e_{L_D}$ therefore $e_A / A = e(L_D) / L_D$. Based on the average value, $A = 0.326$, $r_A = 9.9\%$.

Using this method, the following values of r_x are obtained:

$r = 9.9\%$
 A
 $r = 3.9\%$
 B
 $r = 0.0\%$
 C
 $r = 0.3\%$
 D
 $r = 1.7\%$
 E
 $r = 3.4\%$
 F
 $r_{\sin i} = 5.9\%$
 $r_{\cos o} = 8.2\%$
 $r_{a_T} = 2.1\%$

Table VII. Estimation of Measurement Errors

Physical Variable	Source and Type of Error	Error Interval (+/-)
i o	Random error in the measurement and calculation of the inner taper angle.	0.2°
	The systematic error of symmetry	0.5°
a _T	Random error in the measurement of the room temperature	0.5 K
	Systematic error in the difference between room temp. and initial propellant temp.	3.0 K
	Random and systematic error in converting temperature to a _T (note: in the temperature range of interest da _T /dT is near zero)	0.01
	Accuracy of the a _T data (note: a _T is defined near operating temperatures)	NA
n	Since n is a discrete quantity, it is assumed to have no random error	0.0
a _o	Random error of the measuring instrument	0.25 mm
L _D	Random error in determining the bright flame front tip location	2.0 mm
	Systematic error of correlation between the flame front and actual tip location (note: assumed to be small)	unknown
V _D	Random error of measuring the change of flame front location with respect to time (due to the averaging effect)	0.0
P	Systematic error of the installation, wear, calibration and recording of pressure data	5%
dp/dt	Since dp/dt is calculated using a very large dp and t is very accurate the error should not be greater than in P	5%

(DYN)

DISTRIBUTION LIST

Dr. R.S. Miller
Office of Naval Research
Code 432P
Arlington, VA 22217
(10 copies)

Dr. J. Pastine
Naval Sea Systems Command
Code 06R
Washington, DC 20362

Dr. Kenneth D. Hartman
Hercules Aerospace Division
Hercules Incorporated
Alleghany Ballistic Lab
P.O. Box 210
Washington, DC 21502

Mr. Otto K. Heiney
AFATL-DLJG
Elgin AFB, FL 32542

Dr. Merrill K. King
Atlantic Research Corp.
5390 Cherokee Avenue
Alexandria, VA 22312

Dr. R.L. Lou
Aerojet Strategic Propulsion Co.
Bldg. 05025 - Dept 5400 - MS 167
P.O. Box 15699C
Sacramento, CA 95813

Dr. R. Olsen
Aerojet Strategic Propulsion Co.
Bldg. 05025 - Dept 5400 - MS 167
P.O. Box 15699C
Sacramento, CA 95813

Dr. Randy Peters
Aerojet Strategic Propulsion Co.
Bldg. 05025 - Dept 5400 - MS 167
P.O. Box 15699C
Sacramento, CA 95813

Dr. D. Mann
U.S. Army Research Office
Engineering Division
Box 12211
Research Triangle Park, NC 27709-2211

Dr. L.V. Schmidt
Office of Naval Technology
Code 07CT
Arlington, VA 22217

JHU Applied Physics Laboratory
ATTN: CPIA (Mr. T.W. Christian)
Johns Hopkins Rd.
Laurel, MD 20707

Dr. R. McGuire
Lawrence Livermore Laboratory
University of California
Code L-324
Livermore, CA 94550

P.A. Miller
736 Leavenworth Street, #6
San Francisco, CA 94109

Dr. W. Moniz
Naval Research Lab.
Code 6120
Washington, DC 20375

Dr. K.F. Mueller
Naval Surface Weapons Center
Code R11
White Oak
Silver Spring, MD 20910

Prof. M. Nicol
Dept. of Chemistry & Biochemistry
University of California
Los Angeles, CA 90024

Mr. L. Roslund
Naval Surface Weapons Center
Code R10C
White Oak, Silver Spring, MD 20910

Dr. David C. Sayles
Ballistic Missile Defense
Advanced Technology Center
P.O. Box 1500
Huntsville, AL 35807

(DYN)

DISTRIBUTION LIST

Mr. R. Geisler
ATTN: DY/MS-24
AFRPL
Edwards AFB, CA 93523

Naval Air Systems Command
ATTN: Mr. Bertram P. Sobers
NAVAIR-320G
Jefferson Plaza 1, RM 472
Washington, DC 20361

R.B. Steele
Aerojet Strategic Propulsion Co.
P.O. Box 15699C
Sacramento, CA 95813

Mr. M. Stoss
Naval Surface Weapons Center
Code R10B
White Oak
Silver Spring, MD 20910

Mr. E.S. Sutton
Thiokol Corporation
Elkton Division
P.O. Box 241
Elkton, MD 21921

Dr. Grant Thompson
Morton Thiokol, Inc.
Wasatch Division
MS 240 P.O. Box 524
Brigham City, UT 84302

Dr. R.S. Valentini
United Technologies Chemical Systems
P.O. Box 50015
San Jose, CA 95150-0015

Dr. R.F. Walker
Chief, Energetic Materials Division
DRSMC-LCE (D), B-3022
USA ARDC
Dover, NJ 07801

Dr. Janet Wall
Code 012
Director, Research Administration
Naval Postgraduate School
Monterey, CA 93943

Director
US Army Ballistic Research Lab.
ATTN: DRXBR-IBD
Aberdeen Proving Ground, MD 21005

Commander
US Army Missile Command
ATTN: DRSMI-RKL
Walter W. Wharton
Redstone Arsenal, AL 35898

Dr. Ingo W. May
Army Ballistic Research Lab.
ARRADCOM
Code DRXBR - 1BD
Aberdeen Proving Ground, MD 21005

Dr. E. Zimet
Office of Naval Technology
Code 071
Arlington, VA 22217

Dr. Ronald L. Derr
Naval Weapons Center
Code 389
China Lake, CA 93555

T. Boggs
Naval Weapons Center
Code 389
China Lake, CA 93555

Lee C. Estabrook, P.E.
Morton Thiokol, Inc.
P.O. Box 30058
Shreveport, Louisiana 71130

Dr. J.R. West
Morton Thiokol, Inc.
P.O. Box 30058
Shreveport, Louisiana 71130

Dr. D.D. Dillehay
Morton Thiokol, Inc.
Loughorn Division
Marshall, TX 75670

G.T. Bowman
Atlantic Research Corp.
7511 Wellington Road
Gainesville, VA 22065

(DYN)

DISTRIBUTION LIST

R.E. Shenton
Atlantic Research Corp.
7511 Wellington Road
Gainesville, VA 22065

Mike Barnes
Atlantic Research Corp.
7511 Wellington Road
Gainesville, VA 22065

Dr. Lionel Dickinson
Naval Explosive Ordnance
Disposal Tech. Center
Code D
Indian Head, MD 20340

Prof. J.T. Dickinson
Washington State University
Dept. of Physics 4
Pullman, WA 99164-2814

M.R. Miles
Dept. of Physics
Washington State University
Pullman, WA 99164-2814

Mr. T. F. Davidson
Vice President, Technical
Morton Thiokol, Inc.
Aerospace Group
3340 Airport Road
Ogden, Utah 84405

Mr. J. Consaga
Naval Surface Weapons Center
Code R-16
Indian Head, MD 20640

Naval Sea Systems Command
ATTN: Mr. Charles M. Christensen
NAVSEA-62R2
Crystal Plaza, Bldg. 6, Rm 806
Washington, DC 20362

Mr. R. Beauregard
Naval Sea Systems Command
SEA 64E
Washington, DC 20362

Brian Wheatley
Atlantic Research Corp.
7511 Wellington Road
Gainesville, VA 22065

Mr. G. Edwards
Naval Sea Systems Command
Code 62R32
Washington, DC 20362

C. Dickinson
Naval Surface Weapons Center
White Oak, Code R-13
Silver Spring, MD 20910

Prof. John Deutch
MIT
Department of Chemistry
Cambridge, MA 02139

Dr. E.H. deButts
Hercules Aerospace Co.
P.O. Box 27408
Salt Lake City, UT 84127

Dr. David A. Flanigan
Director, Advanced Technology
Morton, Thiokol, Inc.
Aerospace Group
3340 Airport Road
Ogden, Utah 84405

Dr. L.H. Caveny
Air Force Office of Scientific
Research
Directorate of Aerospace Sciences
Bolling Air Force Base
Washington, DC 20332

W.G. Roger
Code 5253
Naval Ordnance Station
Indian Head, MD 20640

Dr. Donald L. Ball
Air Force Office of Scientific
Research
Directorate of Chemical &
Atmospheric Sciences
Bolling Air Force Base
Washington, DC 20332

(DYN)

DISTRIBUTION LIST

Dr. Anthony J. Matuszko
Air Force Office of Scientific Research
Directorate of Chemical & Atmospheric
Sciences
Bolling Air Force Base
Washington, DC 20332

Dr. Michael Chaykovsky
Naval Surface Weapons Center
Code R11
White Oak
Silver Spring, MD 20910

J.J. Rocchio
USA Ballistic Research Lab.
Aberdeen Proving Ground, MD 21005-5066

G.A. Zimmerman
Aerojet Tactical Systems
P.O. Box 13400
Sacramento, CA 95813

B. Swanson
INC-4 MS C-346
Los Alamos National Laboratory
Los Alamos, New Mexico 87545

Dr. James T. Bryant
Naval Weapons Center
Code 3205B
China Lake, CA 93555

Dr. L. Rothstein
Assistant Director
Naval Explosives Dev. Engineering Dept.
Naval Weapons Station
Yorktown, VA 23691

Dr. M.J. Kamlet
Naval Surface Weapons Center
Code R11
White Oak, Silver Spring, MD 20910

Dr. Henry Webster, III
Manager, Chemical Sciences Branch
ATTN: Code 5063
Crane, IN 47522

Dr. A.L. Slafkosky
Scientific Advisor
Commandant of the Marine Corps
Code RD-1
Washington, DC 20380

Dr. H.G. Adolph
Naval Surface Weapons Center
Code R11
White Oak
Silver Spring, MD 20910

U.S. Army Research Office
Chemical & Biological Sciences
Division
P.O. Box 12211
Research Triangle Park, NC 27709

G. Butcher
Hercules, Inc.
MS X2H
P.O. Box 98
Magna, Utah 84044

W. Waesche
Atlantic Research Corp.
7511 Wellington Road
Gainesville, VA 22065

Dr. John S. Wilkes, Jr.
FJSRL/NC
USAF Academy, CO 80840

Dr. H. Rosenwasser
AIR-320R
Naval Air Systems Command
Washington, DC 20361

Dr. Joyce J. Kaufman
The Johns Hopkins University
Department of Chemistry
Baltimore, MD 21218

Dr. A. Nielsen
Naval Weapons Center
Code 385
China Lake, CA 93555

(DYN)

DISTRIBUTION LIST

K.D. Pae
High Pressure Materials Research Lab.
Rutgers University
P.O. Box 909
Piscataway, NJ 08854

Dr. John K. Dienes
T-3, B216
Los Alamos National Lab.
P.O. Box 1663
Los Alamos, NM 87544

A.N. Gent
Institute Polymer Science
University of Akron
Akron, OH 44325

Dr. D.A. Shockey
SRI International
333 Ravenswood Ave.
Menlo Park, CA 94025

Dr. R.B. Kruse
Morton Thiokol, Inc.
Huntsville Division
Huntsville, AL 35807-7501

G. Butcher
Hercules, Inc.
P.O. Box 98
Magna, UT 84044

W. Waesche
Atlantic Research Corp.
7511 Wellington Road
Gainesville, VA 22065

Dr. R. Bernecker
Naval Surface Weapons Center
Code K13
White Oak
Silver Spring, MD 20910

Prof. Edward Price
Georgia Institute of Tech.
School of Aerospace Engineering
Atlanta, GA 30332

J.A. Birkett
Naval Ordnance Station
Code 5253K
Indian Head, MD 20640

Prof. R.W. Armstrong
University of Maryland
Dept. of Mechanical Engineering
College Park, MD 20742

Herb Richter
Code 385
Naval Weapons Center
China Lake, CA 93555

J.T. Rosenberg
SRI International
333 Ravenswood Ave.
Menlo Park, CA 94025

G.A. Zimmerman
Aeroject Tactical Systems
P.O. Box 13400
Sacramento, CA 95813

Prof. Kenneth Kuo
Pennsylvania State University
Dept. of Mechanical Engineering
University Park, PA 16802

T.L. Boggs
Naval Weapons Center
Code 3891
China Lake, CA 93555

(DTN)

DISTRIBUTION LIST

Dr. C.S. Coffey
Naval Surface Weapons Center
Code R13
White Oak
Silver Spring, MD 20910

J.M. Culver
Strategic Systems Projects Office
SSPO/SP-2731
Crystal Mall #3, RM 1048
Washington, DC 20376

D. Curran
SRI International
333 Ravenswood Avenue
Menlo Park, CA 94025

Prof. G.D. Duvall
Washington State University
Department of Physics
Pullman, WA 99163

E.L. Throckmorton
Code SP-2731
Strategic Systems Program Office
Crystal Mall #3, RM 1048
Washington, DC 23076

Dr. E. Martin
Naval Weapons Center
Code 3858
China Lake, CA 93555

Dr. R. Martinson
Lockheed Missiles and Space Co.
Research and Development
3251 Hanover Street
Palo Alto, CA 94304

Dr. M. Farber
135 W. Maple Avenue
Monrovia, CA 91016

W.L. Elban
Naval Surface Weapons Center
White Oak, Bldg. 343
Silver Spring, MD 20910

C. Cotzmer
Naval Surface Weapons Center
Code R-11
White Oak
Silver Spring, MD 20910

G.E. Manser
Morton Thiokol
Wasatch Division
P.O. Box 524
Brigham City, UT 84302

G.A. Lo
3251 Hanover Street
B204 Lockheed Palo Alto Research Lab
Palo Alto, CA 94304

R.G. Rosemeier
Brimrose Corporation
7720 Belair Road
Baltimore, MD 20742

R.A. Schapery
Civil Engineering Department
Texas A&M University
College Station, TX 77843

Administrative Contracting
Officer (see contract for
address)
(1 copy)

Director
Naval Research Laboratory
Attn: Code 2627
Washington, DC 20375
(6 copies)

Defense Technical Information Center
Bldg. 5, Cameron Station
Alexandria, VA 22314
(12 copies)

Dr. Robert Polvani
National Bureau of Standards
Metallurgy Division
Washington, D.C. 20234

Dr. Y. Gupta
Washington State University
Department of Physics
Pullman, WA 99163